Title	Studies on Electrochemical Syntheses of Semiconductor Thin Films for Photovoltaic Applications
Author(s)	Septina, Wilman
Citation	大阪大学, 2013, 博士論文
Version Type	VoR
URL	https://doi.org/10.18910/26213
rights	
Note	

Studies on Electrochemical Syntheses of Semiconductor Thin Films for Photovoltaic Applications

Wilman Septina

September 2013

Studies on Electrochemical Syntheses of Semiconductor Thin Films for Photovoltaic Applications

A dissertation submitted to

The Graduate School of Engineering Science

Osaka University

In partial fulfillment of the requirements for the degree of
Doctor of Philosophy in Engineering

By

Wilman Septina

September 2013

Contents

Abstract

Direct conversion of solar energy into electric energy using photovoltaics is considered as an ideal solution to meet the growing demand for energy supply because solar energy is unlimited and environmentally friendly. In this study, we investigated fabrication of new photoabsorbers for photovoltaics, such as $Cu_2ZnSnSe_4$, Cu_2ZnSnS_4, $CuSbS_2$ and Cu_2O, by electrochemical deposition (electrodeposition) methods. These materials may replace conventional solar cell materials because they are composed of earth-abundant and safe elements and can be produced by low-cost processes.

Single-step electrodeposition from an acidic electrolyte containing Cu(II), Zn(II), Sn(IV), and Se(IV) species was investigated to synthesis $Cu_2ZnSnSe_4$ (CZTSe). The desired CZTSe film as the main phase was obtained at some selected applied potential ranges. Sulfurization of the as-deposited film at several temperatures under H_2S gas flow resulted in the formation of corresponding mixed compounds of CZTSe and Cu_2ZnSnS_4 (CZTS), *i.e.*, $Cu_2ZnSn(S,Se)_4$ (CZTSSe) with kesterite structure. However, photoelectrochemical measurements of the sulfurized films indicated insufficient quality of the films for photovoltaic application, most notably due to deviation from the ideal kesterite`s composition for solar cell application. To solve this problem, we employed sequential electrodeposition of Cu-Zn-Sn-Se and Cu-Sn-Se layers for fabrication of the CZTSe thin film. Annealing of the bilayer film under Se vapor formed a CZTSe thin film with an ideal composition for solar cell application. The solar cell with a device with the structure of glass/Mo/CZTSe/CdS/ZnO/Al:ZnO derived from thus-obtained CZTSe film exhibited a preliminary conversion efficiency of 1.1%.

We investigated the fabrication of CZTS and $CuSbS_2$ by electrochemical deposition from their metallic stacks. In both the cases, we investigated the effect of preheating to the electrochemically stacked layers of Cu/Sn/Zn and Cu/Sb before sulfurization process. When

the CZTS film was fabricated without the 350-°C preheating, the film contained a secondary Cu_2SnS_3 phase and other impurities. The CZTS film also showed poor adhesion to the bottom molybdenum (Mo) substrate with many crevices and voids in the film. These structural failures of the CZTS film were significantly reduced when the metallic precursor was preheated at 350 °C before sulfurization for 20 min. As expected from these properties, the solar cell with an glass/Mo/CZTS/CdS/Al:ZnO structure derived from the 350 °C preheated metallic precursor for 20 min showed the best conversion efficiency of 5.6%. Similarly, a $CuSbS_2$ film containing appreciable impurity components was obtained when the precursor metallic stack was heated monotonously from room temperature to 450 °C in Ar then sulfurized at this temperature. The film showed poor adherence having many crevices; there were many appreciable pinholes at entire surface of the film. However, a $CuSbS_2$ film without including any impurity phases was obtained when the metallic precursor film was pretreated at 510 °C in Ar for 60 min just before the sulfurization at 450 °C. It was also clarified that the thus-obtained $CuSbS_2$ film showed good adhesion to the Mo/glass substrate and almost no notable pinholes. As expected from these structural analyses, the 510 °C pretreated film worked as a relatively efficient absorber for the thin film solar cell with a glass/Mo/$CuSbS_2$/CdS/Al:ZnO structure: it gave a preliminary conversion efficiency of 3.1%.

Electrodeposition of Cu_2O was performed under potentiostatic control from an alkaline electrolyte solution (pH 12.5) containing copper (II) sulfate and lactic acid. The solar cells with a glass/FTO/Cu_2O/Al:ZnO structure were fabricated by sputtering an Al:ZnO film onto the Cu_2O film. We found that the morphologies and phase purities of the Cu_2O films are highly dependent on the electrodeposition potential; thus it strongly affects the photovoltaic properties. The highest efficiency of 0.603% was obtained with a Cu_2O film deposited at -0.6 V (vs. Ag/AgCl). In addition, we also investigated the feasibility of fabrication of a hybrid solar cell consisting of electrodeposited Cu_2O and spin-coated PCBM. The optimized solar cell showed overall power conversion efficiency of 0.095%.

Chapter 1

General Introduction

1.1.Solar Energy and Photovoltaic (PV)

In 2011, the world consumed energy as much as 142,000 TWh. It is projected that in 2030, the worldwide energy consumption will be increased by about 36%, due to the global increase in population and economy [1]. Currently, the energy sources rely heavily on the fossil fuels (Fig. 1) with about 87 % come from the mixture of oil, coal, and natural-gas [2]. This high-dependence will have a negative side effect in the future, as the sources will be depleted, and it will contribute to the high CO_2 emission. Therefore, alternative energy sources which are renewable, sustainable, and environmental friendly are highly required. At present, the share of alternative energy is only 1.59 % of the global consumption [2].

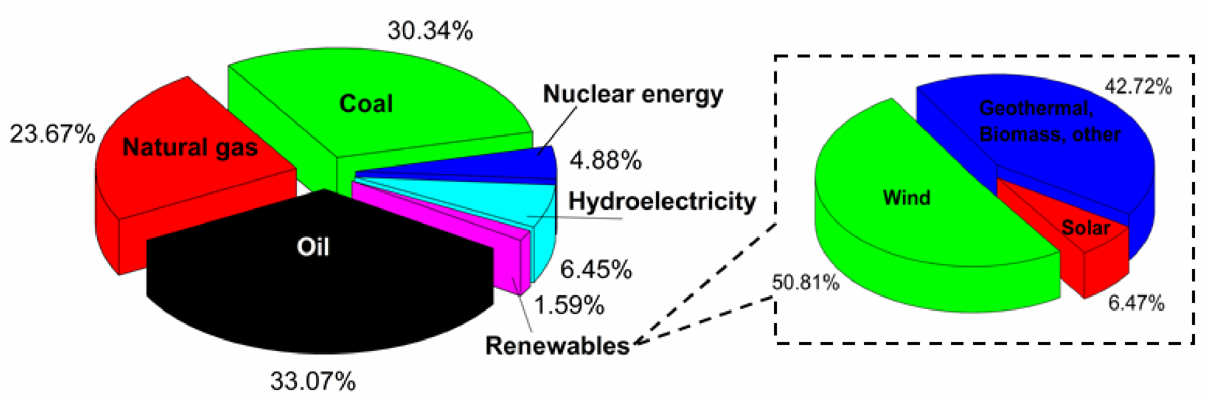

Figure 1. Fraction of world energy consumption by type of energy sources in 2011 and inset shows share of energy consumption among renewable energies in 2011 [2].

Solar energy is one of the alternative energy, which promises an unlimited clean energy for the future. The earth receives about 10^{17} W of energy from the sun, and to put it in another context, the sun provides, in about an hour, the present energy requirements of the entire human population for a whole year [3]. This number indicates huge potential of solar energy as an alternative energy source.

Photovoltaic or solar cell is one of the technologies which enable us to harness the enormous amount of solar energy. It generates direct current (DC) electric power from semiconductors under solar radiation. It can be considered as a two-terminal device which acts like a diode under dark, and generates photovoltage under illumination. Recently, the installation of worldwide photovoltaic has been increasing significantly with the growth rate of about 65% to 75% per year, although the produced energy accounts for a tiny fraction in the total energy used (see Fig. 1) .

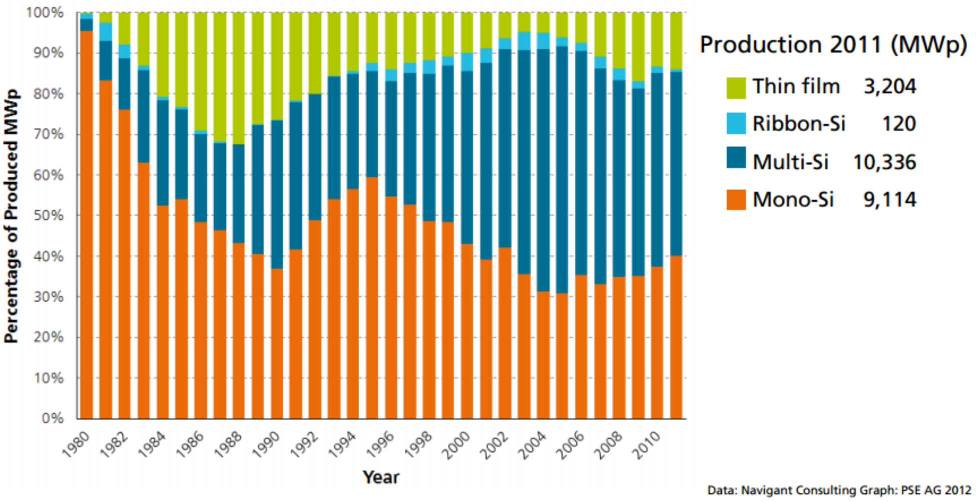

Data: Navigant Consulting Graph: PSE AG 2012

Figure 2. Market share of PV technology. [5]

Figure 2 shows market shares of various solar cells over a period 1980 to 2011. So far, silicon-based solar cells have dominated the majority of the solar-energy market due to their well-developed fabrication techniques and relatively good cells energy conversion efficiencies of 20 to 25% [4]. At present, it accounts for about 80-90% of total installed solar cells in the world. In majority, the silicon is fabricated in its monocrystalline or multicrystalline forms. The monocrystalline silicon is produced by slicing wafers from a high-purity single crystal ingot. The multicrystalline silicon is made by sawing a cast block of silicon first into bars and then into wafers.

The cost of Si solar cell is largely dependent on the cost of Si wafer used in the fabrication. Their high fabrication cost and limited feedstock of silicon spark the photovoltaic community to search for new materials and technologies. Cheaper solar cells can only be produced by using cheaper materials and low-cost fabrication methods. This is where thin film technology offers promising potential as an alternative to silicon photovoltaic technology. Thin film solar cells are based on materials that strongly absorb sunlight so that the cells can be very thin (1-3 μm), which reduces the demand for the amount of the raw material. In addition, thin film solar cells are less susceptible to purity and crystallinity of the materials. Details of the thin-film technology will be explained in the next chapter.

1.2.Thin Film PV

As mentioned in the previous chapter, thin film solar cell technology emerged from the constraint of the high-cost production of monocrystalline silicon solar cell, which requires Si in the pure crystalline form. The thin film solar cells are based on materials that strongly absorb sunlight so that the cells can be made very thin (1-3 μm). Besides that, the thin film solar cell also has several features that make it an attractive alternative to the conventional Si solar cell. The features of the thin film solar cell are as follows: [6]

1. A variety of methods can be used to fabricate thin films ranging from vacuum methods, such as sputtering, evaporation, and plasma deposition, to non-vacuum methods such as electrodeposition, spray pyrolysis, and chemical bath deposition.
2. The films can be amorphous, highly oriented, or epitaxial depending upon the deposition techniques and parameters.
3. A wide choice of substrates is available from rigid to flexible.

4. Easy doping or alloying during depositions.
5. Different types of electronic junctions such as single or tandem junctions are possible.
6. Graded band gap or graded composition of the materials can be easily obtained.

1.2.1. Thin film PV materials

Various materials can be made into thin films. The ideal materials should have high optical absorptivity to absorb the sunlight irradiation (>10^4 cm^{-1}). It should also have an appropriate band gap, ideally around 1.5 eV, to absorb a significant portion of solar spectrum. The materials also should be able to form a good electronic p-n junction with compatible materials.

A large number of materials have been found to be promising for thin film photoabsorbers. Figure 3 showed the maximum theoretical efficiency for some of the potential materials in an ideal p-n junction structure, which was calculated according to the Schokley-Quisser detailed balance limit [7]. As seen from the figure, various materials are predicted to have an efficiency higher than 10%, which possess an optimal band gap in a range 1.0 eV to 1.5 eV. This estimation assumes a loss only due to the radiative recombination. However, in reality, imperfection of the crystal, such as the defect, the intrinsic electrical and optical properties of the materials, and lattice mismatch of the p and n-type materials, contributes to some losses, and leading to a lower efficiency.

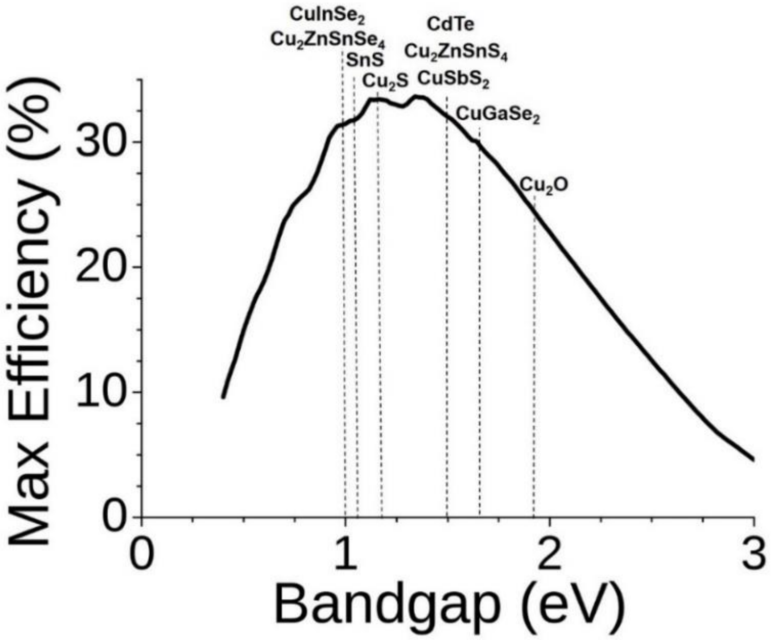

Figure 3. Schokley-Quissier theoretical efficiency of some of the semiconductors for thin film solar cells.

To date, three of the most commonly studied thin film materials are amorphous silicon, CdTe, and Cu(In,Ga)Se_2 (CIGS), which are already used in commercialized solar cells with module efficiencies of around 10%, 13%, and 16%, respectively [4]. With the recent trend of increase in market share of thin-film PV, with the total commulative installation of about 11.5 GW in 2011 [8], there is a huge demand for bigger expansion of the installation. However, recent studies suggest that there will be a constraint for further continuous growth, especially if we want to reach terra-watt (TW) scale. Due to the limited availability of Te and In (see Fig. 4), it is predicted that maximum total installation capacity of CdTe and CIGS solar cells are about 120 GWp and 11,000 GWp, respectively [9][10].The high price of In and Ga coupled with the toxicity issue of Cd also limits the use of these compounds on a large scale.

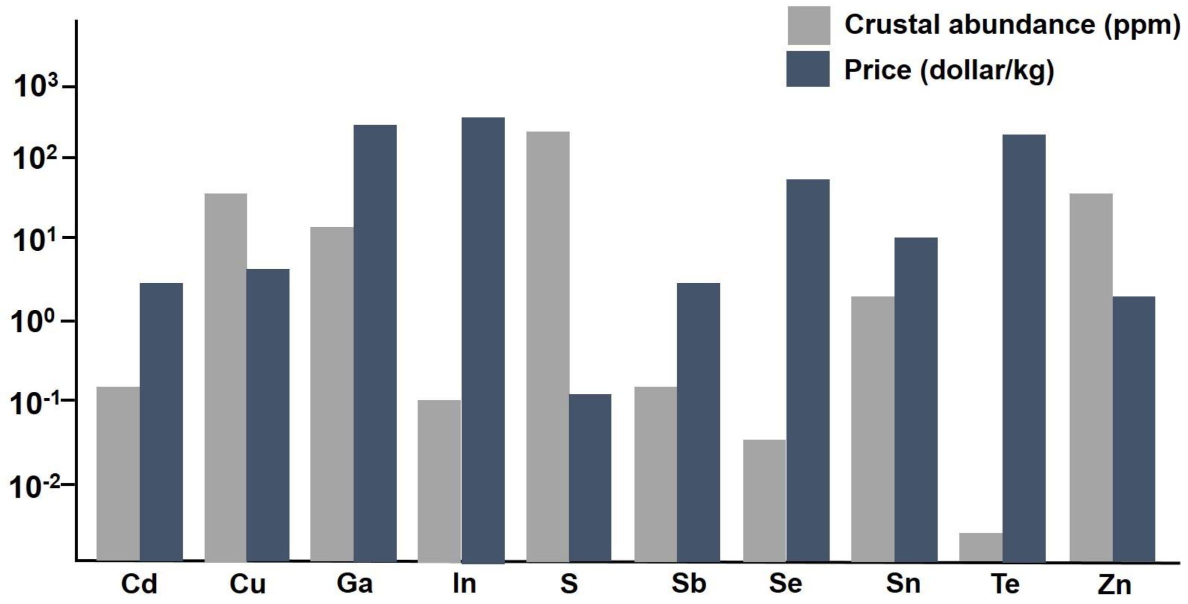

Figure 4. Crustal abundance (ppm) and price (dollar/kg) of the related elements used in thin film solar cells. Adapted from ref [11] and [12].

The above limitations prompted intensive investigations of the compounds that contained earth-abundant and low-cost elements. As listed in Fig. 4, $Cu_2ZnSnS(e)_4$, SnS, Cu_2S, $CuSbS_2$, and Cu_2O are among the potential alternative materials for thin film solar cells. These materials consist of elements that are more abundant and lower in price than those of CdTe and CIGS. However, maximum reported efficiencies of the solar cells based on those materials are lower than those of CdTe and CIGS: 11.1% for $Cu_2ZnSnS(e)_4$ [13], 2.46% for SnS [14], 9.1% for Cu_2S [15], 3.1% for $CuSbS_2$ [16] and 4.12% for Cu_2O [17]. In addition, the solar cells made of the binary compounds is still a major issue. Hence, it is important to develop low cost processes for fabrication of these new-type solar cells with high efficiency and good durability.

1.3. Working Principles of Solar Cells

Photovoltaic action involves several processes that lead to conversion of sunlight energy into electricity. These processes include charge (electron and hole) generation, charge separation, and charge transport. Charges generated by light absorption by semiconductor have to be separated by some driving force in order to generate as photocurrent and photovoltage. This driving force can be established in many ways through various solar cell structures. In this section, we will briefly review the structures and working principles of some of the type of solar cells that are relevant to this thesis.

1.3.1. Schottky-barrier Solar Cell

The simplests structure of solar cells possesses the semiconductor-metal junction which is usually called a Schottky-barrier junction. This is achieved by joining a p-type or n-type semiconductor with a metal with a certain value of work function (Φ_m) so that the work function of a p-type semiconductor (Φ_p) is higher than the work function of metal ($\Phi_p > \Phi_m$) or the opposite for an n-type semiconductor ($\Phi_n < \Phi_m$). The work function of materials is defined as the potential required to remove the least tightly bound electron, and in a metal Φ_m is equal to the electron affinity. In semiconductors, Φ_p or Φ_n can be controlled by doping.

Figure 5a shows a typical structure of a Schottky-barrier solar cell with a p-type semiconductor/metal junction. When they are brought into contact, their fermi levels (E_f) will line up via charge transfer and caused the semiconductor bands to bend down toward the interface (Fig. 5b), presenting a barrier toward majority carriers (holes). This alignment will create a region in the interface which is depleted in carriers, which is usually called a depleted region or a space charge region (W). Under illumination with photon energy greater than E_g, the space charge layer will cause electron-hole pairs photogenerated in the semiconductor to be separated so that electrons accumulate in the metal and holes in the semiconductor, and develops photovoltage; the semiconductor becomes more positive than the metal. This photovoltage is related to the difference in work functions between the semiconductor and the metal.

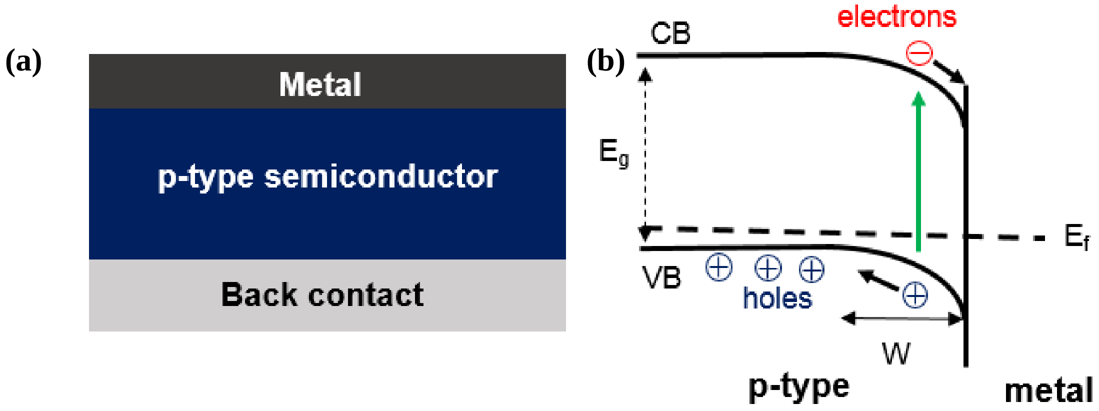

Figure 5. (a) Basic structure of schottky-barrier solar cell, and (b) illustration of working principle of the cell

1.3.2. P-N Homojunction Solar Cell

P-n junction is the most widely used structure for solar cells. The conventional silicon-based solar cell and most of the thin film solar cells basically works based on p-n junction. P-n homojunction is created by doping the same semiconductor asymmetrically, so that we have an interface between p-type and n-type layers of the same material. Figure 6 shows a typical structure of a p-n homojunction solar cell.

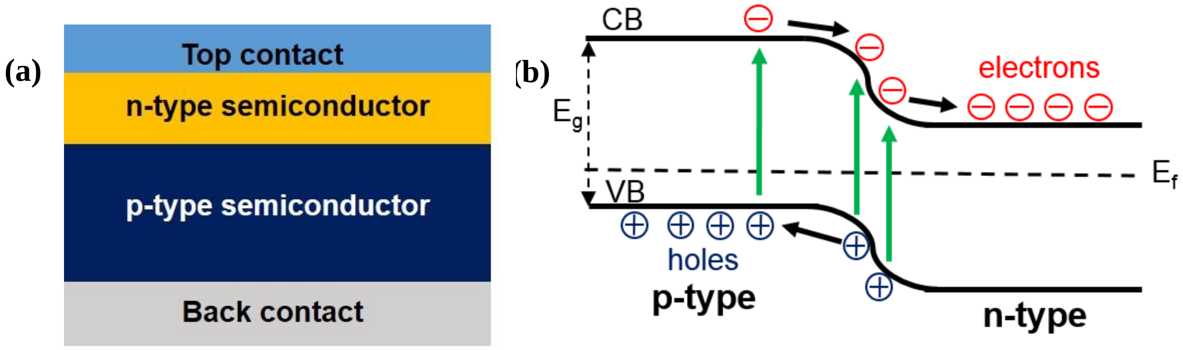

Figure 6. (a) Basic structure of p-n homojunction solar cell, and (b) illustration of working

principle of p-n junction.

Since the work function of a p type material is larger than that of a n-type, the electrostatic potential of the n side must be must be more positive than that of the p side, and an electric field is established across the junction (see Fig. 6b) which drives photogenerated electrons towards the n side and holes towards the p side. The junction region is depleted of both electrons and holes, and always presents a barrier to majority carriers (holes in p-type and electrons in n-type), and a low-resistance path to minority carriers. Minority carriers photogenerated in the p and n layers reach the junction by diffusion, then are transferred to the corresponding sides: electrons to the n-type side and holes to the p-type side.

1.3.3. P-N Heterojunction Solar Cell

The p-n junction also can be made using two different semiconductor materials with different band gaps, which is usually called a heterojunction. This junction is usually employed to semiconductors that are difficult to make both p-type and n-type. In this design, we can select a combination of materials, which will give high photovoltage based upon the differences in band gaps. Photocurrent loss can be minimized by choosing the semiconductors materials with wide band gaps, such as ZnO, CdS, ZnS, etc. for the front side.

The heterojunction concept is the basis for the solar cells based on p-type semiconductors such as CdTe, CIGS, and emerging thin film materials such as $Cu_2ZnSnS(e)_4$ and $CuSbS_2$. Figure 7a shows the typical structure of a heterojunction solar cell. The window layer usually consists of bilayer of intrinsic and doped ZnO, which acts as a front contact through which the sunlight comes. The buffer layer is usually made of n-type material, which has a wide band gap to form p-n junction as well as to admit maximum amount of light to the junction and the absorber.

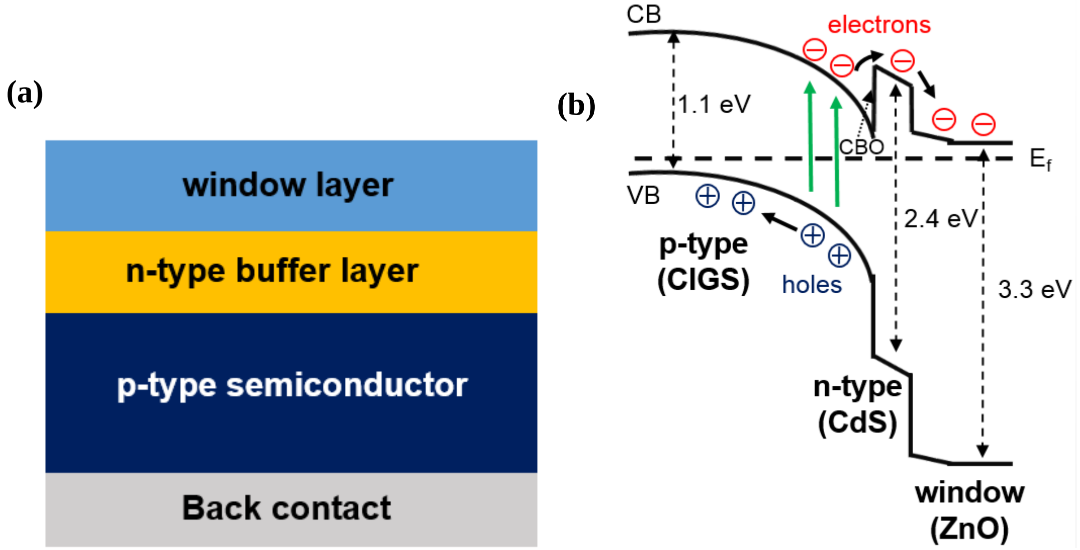

Figure 7. (a) Basic structure of p-n heterojunction solar cell, and (b) illustration of working principle of CIGS/CdS/ZnO heterojunction solar cell.

The working principle and band diagram of the heterojunction solar cell is shown in Fig. 7b. Here, CIGS/CdS/ZnO heterojunction is chosen on which a lot of study has been reported and various aspects have been reviewed [18-21]. Due to differences in conduction band (CB) levels of CIGS and CdS, upon contacting they form a conduction band offset (CBO = CB_{CdS} - CB_{CIGS}) which will create a barrier to the photogenerated electrons, as shown in the illustration. It has been reported that increasing recombination at the interface is observed for negative CBO and whereas too-large positive CBO impedes electron transfer across the interface. Hence, a positive CBO, whereas in the range of 0 to 0.4 eV, which usually called “spike alignment”, is important to obtain high photovoltaic performance [19].

1.3.4. Current-Voltage (*J*-*V*) Characteristics

A solar cell is basically a semiconductor diode. The semiconductor materials absorb the incoming photons and convert them into electron-hole pairs. The important parameter is band gap energy (E_g) of the semiconductor. All photons with photon energy ($h\nu$)>E_g will each contribute to the photogenerated electron-hole pairs with the excess energy lost because of thermalization.

(a)

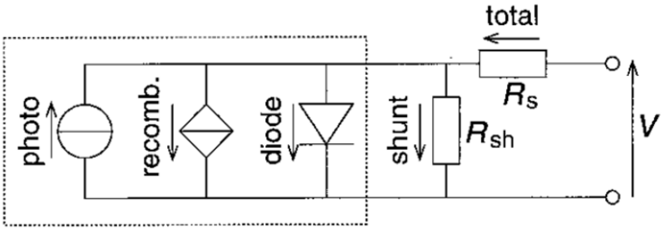

(b)

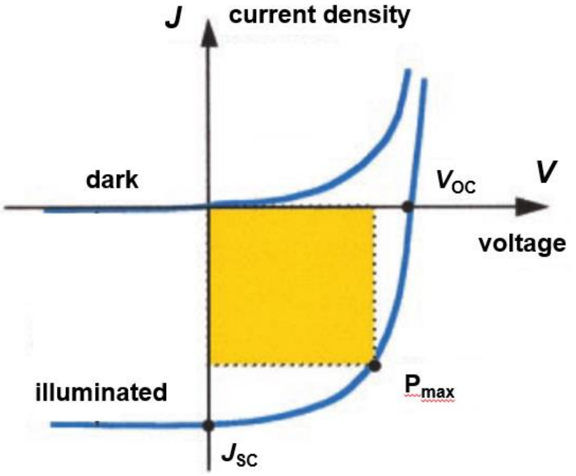

Figure 8. (a) Electrical equivalent circuit of a solar cell. (b) Typical *J*-*V* characteristics of a solar cell. Adapted from ref [22]

In the second step of the energy conversion process, the photogenerated electron-hole pairs are separated, with electron drifting to one of the electrodes and hole drifting to the other electrode because of the internal electric field caused by the junction structure. The equivalent circuit of a solar cell is shown in Figure 8a. Series resistance (R_s) and shunt resistance (R_{sh}) are resistors that represent electrical losses. R_s is particularly due to contact resistance and R_{sh} is commonly due to pinholes through the solar cell.

The current density - voltage (J-V) relation of the solar cell is shown in Figure 8b. Short circuit current J_{SC}, open circuit voltage V_{OC}, and fill factor FF are the three key parameters characterizing the solar cell performance. The maximum limit current is given by the photogenerated current density J_{SC}. The cell power density (P) reaches maximum at the cell`s operating point or maximum power point (P_{max}). This occurs at some voltage V_m with a corresponding current density J_m. The fill factor is defined by the following ratio

$$FF = \frac{J_m V_m}{J_{SC} V_{OC}} \tag{1.1}$$

The efficiency η of the cell is given by the ratio of the power density delivered at an operating point to the incident light power density, P_s,

$$\eta = \frac{J_m V_m}{P_s} \tag{1.2}$$

Efficiency is related to J_{sc} and V_{oc} using FF,

$$\eta = \frac{J_{sc} V_{oc} FF}{P_s} \tag{1.3}$$

1.4. Electrochemical Deposition of Thin-film Compound

Electrodeposition is a well-known technology to deposit metals and alloys in the industry with wide applications from copper deposition in electronic industry for integrated circuit to zinc or chromium coating for surface protection. In recent years, electrodeposited thin film semiconductors have been used in solar cell applications, and several companies have already commercialized the solar cells based upon this method, such as CIGS-based solar cell by Solo Power. Besides that, electrodeposition techniques are also successfully employed to prepare numerous binary, ternary, and quaternary semiconductors such as CdSe [23], Cu_2O [24][25], $CuSbS_2$ [16][26], Cu_3BiS_3[27], Cu_2ZnSnS_4 [28][29], $Cu_2ZnSnSe_4$ [30][31], etc.

Fabrication of thin film semiconductors for solar cells by the electrodeposition offers several advantages over other deposition techniques:

1. It is simple and economical technique because of its low operating temperature, low cost apparatus, and negligible waste materials.
2. It is not required to have very pure starting materials, as in the case of other methods such as sputtering or coevaporation.
3. The deposition is mainly controlled by electrical paramters such as electrode voltage and current density, which are easily adjusted to control the film thickness, composition, morphology, etc.
4. An electrochemical synthesis is an oxidation or a reduction reaction. By fine-tuning the applied cell potential, the oxidizing or reducing power can be continuously varied and suitably selected.

1.4.1. Basic Principles

An example of the electrodeposition system is shown in Fig. 9a. In general, the electrodeposition of thin film requires an electrolyte containing appropriate metal ions (for example, $CuSO_4$ solution for the deposition of copper and $ZnSO_4$ solution for deposition of zinc), an electrode or a substrate where the deposition is desired (working electrode), a counter electrode (usually inert metals such as Pt), a reference electrode (Ag/AgCl or a standard calomel electrode (SCE)), and a potentiostat or a galvanostat as a power source. When current flows through the electrolyte, the cations and anions move toward the working and counter electrodes, respectively, and deposition occurs on the working electrode after undergoing some charge transfer. During the electrodeposition, reaction at the electrode includes several steps (Fig. 9b) [32],

(1) Ionic transfer

(2) Discharge

(3) Breaking up of ion-ligand bond

(4) Incorporation of adatoms onto the electrode followed by nucleation and growth

The thermodynamical potential for electrodeposition is given by the Nernst equation [33],

$$E_m = E_m^0 + \frac{RT}{nF}\ln\left(\frac{a_m^{m+}}{a_m}\right) \qquad (1.4)$$

where E_m is the reduction potential of a metal M in a given electrolyte, E_m^0 is the standard reduction potential to form M, R is the gas constant, T is the absolute temperature, n is the number of electrons required for the reduction, F is the Faraday constant, and a_m^{m+} and a_m are the activities of M^{m+} ions in the electrolyte and of metallic M in the deposit, respectively.

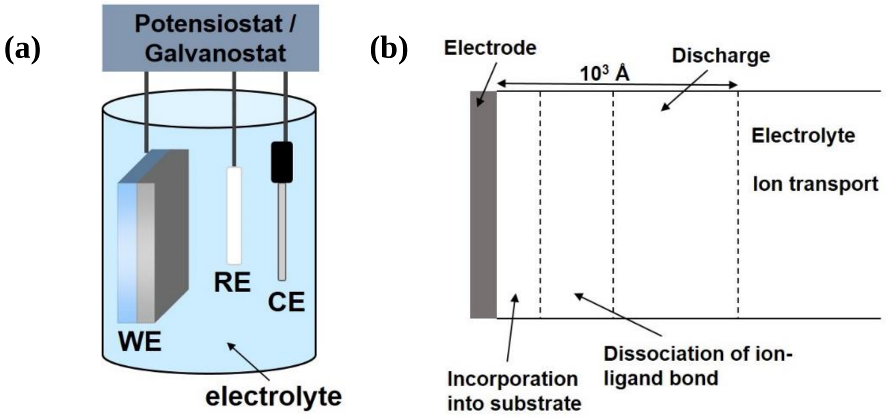

Figure 9. (a) Electrochemical deposition setup. RE : reference electrode, WE : working electrode, CE: counter electrode. (b) Reactions in the electrodeposition process.

In ideal conditions, electrodeposition of M can occur at potentials more negative than the thermodynamical reduction potential (E_m) of the metal M. The difference between the working potential and E_m is known as overpotential. In a potentiostatic deposition, the potential to be employed is not always known beforehand. Therefore, a linear voltammetry is usually first carried out by scanning the potential from an initial value, E_i, to a final value E_f. E_i and E_f correspond to potentials at which the solvent undergoes electrolysis, for instance, the hydrogen evolution and oxygen evolution potentials for an aqueous electrolyte solution. A potentiostatic synthesis can be carried out if the reaction takes place at any potential between these two values. If the reaction potential falls outside the window region provided by E_i and E_f, then another suitable electrode and solvent have to be chosen with the appropriate potential window which includes the reaction potential. Beside that, the Pourbaix diagram (potential-pH) is commonly used as a guide to determine the preliminary electrodeposition conditions, especially the pH value of the electrolyte [34].

1.4.2. Examples of Electrodeposition Approaches

The electrodeposition approach to prepare thin film semiconductors for solar cells is useful because that complex materials such as quaternary or pentarnary semiconductor of $Cu_2ZnSn(S,Se)_4$ can be prepared. There are 3 strategies for the synthesis: deposition of metallic stack (Cu, Sn, and Zn), binary stack (Cu_2Se, $SnSe_2$, and ZnSe), and all the elements, as shown in Fig. 10. We can use the suitable methods to get the desired quality of the material. After deposition, usually heat treatment at high temperature under Ar or sulfur (S) or selenium (Se) is required to obtain the desired materials with high crystallinity.

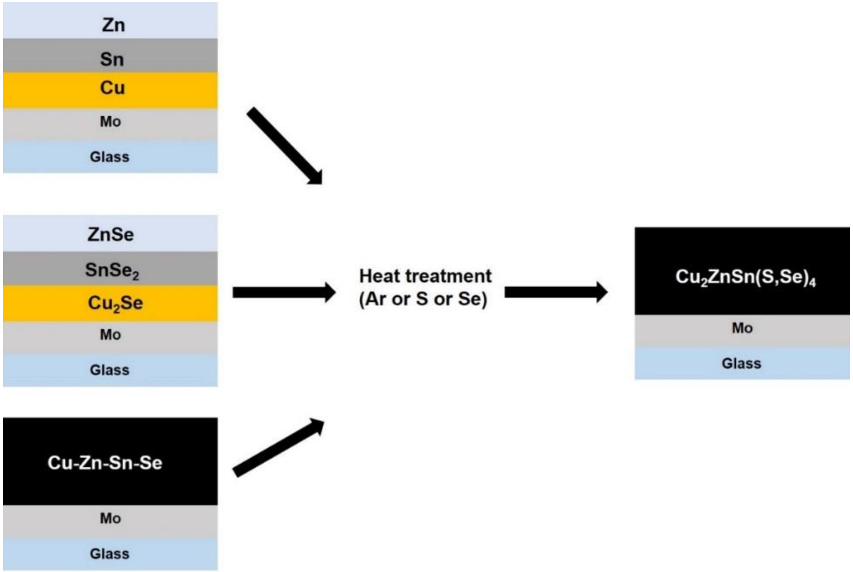

Figure 10. Various electrodeposition approaches to prepare $Cu_2ZnSn(S,Se)_4$.

Possible reactions that occur during the electrodeposition of materials for $Cu_2ZnSn(S,Se)_4$ solar cells can be simplified as follows:

$$Cu^{2+} + 2e^{-} \rightarrow Cu \quad (1.5)$$

$$Sn^{2+} + 2e^{-} \rightarrow Sn \quad (1.6)$$

$$Zn^{2+} + 2e^{-} \rightarrow Zn \quad (1.7)$$

$$2Cu^{2+} + Se^{2-} + 2e^{-} \rightarrow Cu_2Se \quad (1.8)$$

$$Sn^{4+} + Se^{2-} + 2e^{-} \rightarrow SnSe_2 \quad (1.9)$$

$$Zn^{2+} + Se^{2-} \rightarrow ZnSe \quad (1.10)$$

$$2Cu^{2+} + Sn^{4+} + Zn^{2+} + 4Se^{2-} \rightarrow Cu_2ZnSnSe_4 \quad (1.11)$$

It should be noted that in actual deposition, the electrolyte solution usually involves complexing agents or additives. Therefore, the true reactions should be more complicated.

1.5. Photoelectrochemical Characterization of Thin-film Compound

Photoelectrochemical measurements of thin film semiconductors in contact with an electrolyte have been widely used to evaluate the photoactivity of the materials prior to the fabrication of solar cells [35-39]. In our laboratory, this method is frequently used to test the new materials for solar cell, as will be shown in several chapters in this thesis. The advantage of using electrolyte to characterize thin film semiconductors is that it is transparent and it easily forms contact with the semiconductors without damaging them. The contact is also rather ideal due to the absence of the lattice mismatch at the interface, which is commonly observed at the metal contact. Moreover, it is also tolerable to pinholes in the film which may cause a shunting leakage in the solar cell device.

In general, the electrolyte used contains a redox couple that is able to scavenge minority carriers (electrons for p-type and holes for n-type). Upon contacting the semiconductor with the electrolyte, the Fermi level (E_F) of the semiconductor will align with the Fermi level of the redox couple, so that E_F (semiconductor) = E_F (redox), leading to the formation of a Schottky barrier. In the case of p-type semiconductor (Fig. 11), when the semiconductor is in contact with a redox system which has a higher Fermi level, the energy bands bend downward toward the interface as the majority carriers (holes) are extracted into the redox system until the Fermi levels are equalized (equilibrium). This will create a depletion layer known as a space charge region (W). When this junction is illuminated, electron can be excited from the valence band (VB) to the conduction band (CB) provided that the photon energy is higher than the band gap energy of the semiconductor. Under the depletion condition, minority carriers (electrons in p-type) created by the light absorption in the space charge region are transported to the interface by drift/diffusion. Minority carriers generated deeper in the bulk may still be collected by diffusing to the space charge region provided that the diffusion length is sufficient. Otherwise, they will recombine with the majority carriers. The minority carriers transported to the surface may undergo charge transfer to the redox system or recombine with the majority carriers via surface trap. The width of the space charge region can be conveniently varied by varying the band bending via controlling the applied potential with respect to the reference electrode potential.

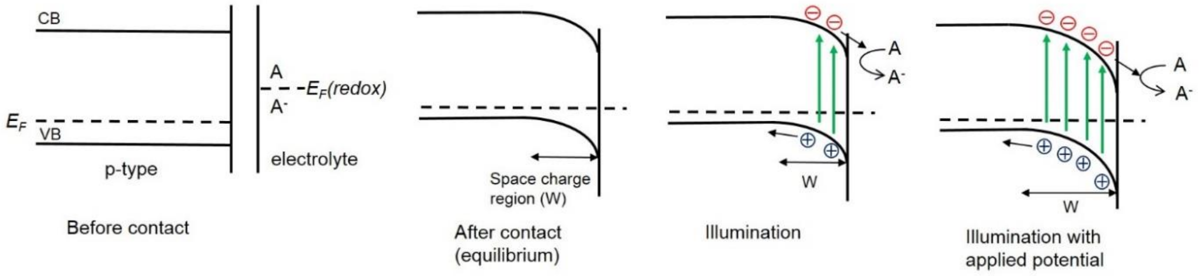

Figure 11. Illustration of condition of semiconductor and electrolyte contact: before contact, after contact, under illumination, and under illumination with applied potential, respectively.

1.5.1. Photovoltammetry

Photovoltammetry technique offers a powerful method for evaluating the photoactivity of the new materials for solar cells, which does not need to fabricate an entire device [39]. The measuremens can be carried out by sweeping the electrode potential under chopped light. White light or LED light with the wavelengths where the semiconductor absorb strongly are commonly used as the light sources. Figure 12a showed an example of photovoltammogram of $CuInS_2$ synthesized in our laboratory using Eu^{3+}/Eu^{2+} as the redox couple and Xenon lamp as the light source [40]. The sign of the photocurrent can be used to identify the majority carrier type; cathodic current indicates p-type and anodic current indicates n-type. The magnitude of the photocurrent indicates the fraction of photogenerated minority carriers contributing the photocurrent. Therefore, it shows the existence of surface or bulk traps, and also gives indication of the external quantum efficiency (EQE). Scanning in the dark (light off) gives information about the pinholes in the film or any impurities in the film, which can be deduced from high dark currents and the appearance of transient current spikes associated with oxidation and reduction of redox couple in contact with the metal substrate or impurities.

1.5.2. External Quantum Efficiency

Measurement of EQE of photocurrent as a function of photonenergy provides information such as photoabsorption profile of the material, doping densities, and minority carrier diffusion length. EQE is defined as ratio of electron flux in the external circuit to the incident photon flux. Therefore, it is also called IPCE (incident photon to current conversion efficiency) [41]. Figure 12b showed an example of the EQE/IPCE spectrum of a $CuInS_2$ film electrode [40].

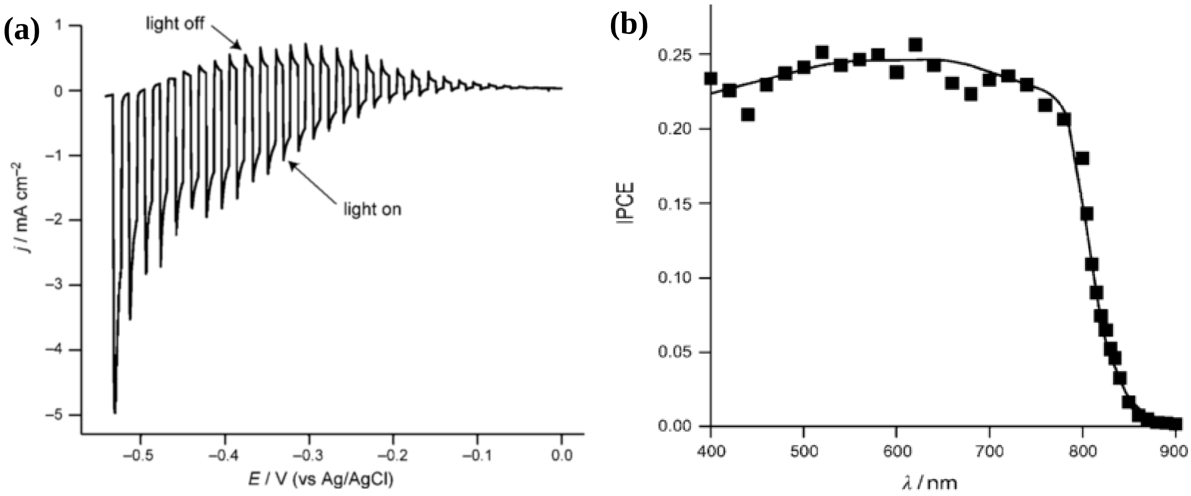

Figure 12. Examples of (a) photovoltammetry graph and (b) EQE/IPCE spectrum.

The EQE of an ideal semiconductor/electrolyte junction under applied bias is given by the Gartner equation [42],

$$\mathrm{EQE} = 1 - \frac{\exp(-\alpha W)}{1+\alpha L_n}, \tag{1.12}$$

where α is the absorption coefficient of the material, W is the width of the space charge region, and L_n is the minority carrier diffusion length. W also can be defined as,

$$W = \{2(E_{\mathrm{FB}} - E)\varepsilon_0\varepsilon_{\mathrm{r}}/qN_{\mathrm{d}}\}^{1/2}, \tag{1.13}$$

where, E_{FB}, E, ε_0, ε_{r}, q, and N_{d} are a flatband potential, an applied potential, the dielectric constant of vacuum, a specific dielectric constant of the material, the electric charge, and a dopant density, respectively.

1.6. Research Objectives

The objectives of this thesis study are:

(1) To investigate the feasibility of fabrication of various alternative thin-film photoabsorbers by electrodeposition, particularly $Cu_2ZnSnSe_4$, Cu_2ZnSnS_4, $CuSbS_2$ and Cu_2O.

(2) To study the direct electrochemical synthesis and characterization of $Cu_2ZnSnSe_4$ films, and their application in thin film solar cells.

(3) To investigate electrochemical deposition methods and successive processes to fabricate Cu_2ZnSnS_4 and $CuSbS_2$, and their application in thin film solar cells.

(4) To investigate the electrochemical synthesis and characterization of Cu_2O film, and its application in thin film and hybrid solar cells

1.7. Scope and Outline of Thesis

This thesis mainly deals with electrochemical deposition and characterization of various alternative photoabsorbers for thin film solar cells, particularly $Cu_2ZnSnSe_4$, Cu_2ZnSnS_4, $CuSbS_2$ and Cu_2O. The outline of each chapter is as follows:

Chapter 1

This chapter concerns about the background of development of photovoltaics and the emerging history of thin film photovoltaics including the recent research challenges, particularly the challenges to developing materials containing more earth abundant elements. The relevant theoretical backgrounds of the thin film photovoltaics, electrodeposition, including photoelectrochemical characterization are also briefly explained. Based on the explained backgrounds, the research objectives and the outline of the thesis are presented.

Chapter 2

The possibility of single–step electrodeposition synthesis of a $Cu_2ZnSnSe_4$ (CZTSe) film on a Mo–coated glass substrate from an acidic electrolyte containing Cu(II), Zn(II), Sn(IV), and Se(IV) species was examined. Effects of applied potentials on film compositions and film morphologies were studied in detail. Mechanistic aspects of the formation and growth of a CZTSe film were also assessed. To improve stoichiometry of the CZTSe film, we also employed a bilayer film made of Cu-Zn-Sn-Se and Cu-Sn-Se layers, which were electrodeposited sequentially, as the precursor for fabrication of the CZTSe film. The precursor film was converted to CZTSe by annealing under Ar or Se vapor. The solar cell properties of devices fabricated from these annealed films are also reported.

Chapter 3

We investigated fabrication of Cu_2ZnSnS_4 and $CuSbS_2$ thin films by sulfurization of electrochemically deposited metallic stacks composed of Cu/Sn/Zn and Cu/Sb, respectively. Effect of preheating of the electrodeposited metallic stacks before the sulfurization on morphologies of the final films were examined. Based on the results, the effects of preheating on photovoltaic properties of the thus-obtained Cu_2ZnSnS_4 and $CuSbS_2$-based cell are also discussed.

Chapter 4

In this chapter, potentiostatic deposition of Cu_2O thin films on glass substrates coated with transparent conductive oxide (TCO) is described. For the purpose of achieving optimum solar cell properties, we investigated fabrication of solar cells based on a Cu_2O/Al:ZnO heterojunction. Effects of applied potentials for the Cu_2O deposition on structural properties of the Cu_2O films and properties of the solar cells made of these films are discussed in detail. In addition, we fabricated inorganic/organic hybrid solar cells consisting of the Cu_2O layer and a fullerene derivative (PCBM) layer. The solar cell properties were studied by changing the conditions of electrochemical deposition of the Cu_2O layer and post-annealing.

Finally, the results obtained through this work and perspectives for the future were described in General conclusion.

References

[1] B. Petroleum, BP Statistical Review, (2011).

[2] B. Dudley, BP statistical review of world energy, in, 2012.

[3] P.A. Lynn, Electricity from sunlight: an introduction to photovoltaics, Wiley, 2011.

[4] M.A. Green, K. Emery, Y. Hishikawa, W. Warta, E.D. Dunlop, Progress in Photovoltaics: Research and Applications, 20 (2012) 12-20.

[5] Fraunhofer Institute for Solar Energy Systems, Photovoltaic Reports, December 2012.

[6] K.L. Chopra, P.D. Paulson, V. Dutta, Progress in Photovoltaics: Research and Applications, 12 (2004) 69-92.

[7] W. Shockley, H.J. Queisser, Journal of Applied Physics, 32 (1961) 510-519.

[8] A. Jäger-Waldau, Int J Photoenergy, 2012 (2012) 1-6.

[9] C. Candelise, M. Winskel, R. Gross, Prog Photovoltaics, 20 (2012) 816-831.

[10] C. Candelise, J.F. Speirs, R.J. Gross, Renewable and Sustainable Energy Reviews, 15 (2011) 4972-4981.

[11] WebElements: the periodic table on the web. http://www.webelements.com/ (accessed May 1, 2013)

[12] http://www.metalprices.com/ (accessed May 1, 2013)

[13] T.K. Todorov, J. Tang, S. Bag, O. Gunawan, T. Gokmen, Y. Zhu, D.B. Mitzi, Advanced Energy Materials, 3 (2013) 34-38.

[14] P. Sinsermsuksakul, K. Hartman, S. Bok Kim, J. Heo, L. Sun, H. Hejin Park, R. Chakraborty, T. Buonassisi, R.G. Gordon, Applied Physics Letters, 102 (2013) 053901.

[15] J.A. Bragagnolo, A.M. Barnett, J.E. Phillips, R.B. Hall, A. Rothwarf, J.D. Meakin, Electron Devices, IEEE Transactions on, 27 (1980) 645-651.

[16] W. Septina, S. Ikeda, Y. Iga, T. Nakamura, T. Harada, M. Matsumura, Thin Solid Films, submitted.

[17] Y. Nishi, T. Miyata, T. Minami, Thin Solid Films, 528 (2013) 72-76.

[18] S. Niki, M. Contreras, I. Repins, M. Powalla, K. Kushiya, S. Ishizuka, K. Matsubara, Progress in Photovoltaics: Research and Applications, 18 (2010) 453-466.

[19] M. Gloeckler, J.R. Sites, Thin Solid Films, 480 (2005) 241-245.

[20] S. Siebentritt, M. Igalson, C. Persson, S. Lany, Progress in Photovoltaics: Research and Applications, 18 (2010) 390-410.

[21] A. Rockett, Progress in Photovoltaics: Research and Applications, 20 (2012) 575-581.

[22] A. Shah, Science, 285 (1999) 692-698.

[23] O. Savadogo, Solar Energy Materials and Solar Cells, 52 (1998) 361-388.

[24] W. Septina, S. Ikeda, M.A. Khan, T. Hirai, T. Harada, M. Matsumura, L.M. Peter, Electrochimica Acta, 56 (2011) 4882-4888.

[25] M. Izaki, T. Shinagawa, K.T. Mizuno, Y. Ida, M. Inaba, A. Tasaka, J Phys D Appl Phys, 40 (2007) 3326-3329.

[26] D. Colombara, L.M. Peter, K.D. Rogers, J.D. Painter, S. Roncallo, Thin Solid Films, 519 (2011) 7438-7443.

[27] D. Colombara, L.M. Peter, K.D. Rogers, K. Hutchings, J Solid State Chem, 186 (2012) 36-46.

[28] Y. Lin, S. Ikeda, W. Septina, T. Harada, M. Matsumura, Solar Energy Materials and Solar Cells, in review.

[29] S. Ahmed, K.B. Reuter, O. Gunawan, L. Guo, L.T. Romankiw, H. Deligianni, Advanced Energy Materials, 2 (2012) 253-259.

[30] W. Septina, S. Ikeda, A. Kyoraiseki, T. Harada, M. Matsumura, Electrochimica Acta, 88 (2013) 436-442.

[31] L. Guo, Y. Zhu, O. Gunawan, T. Gokmen, V.R. Deline, S. Ahmed, L.T. Romankiw, H. Deligianni, Progress in Photovoltaics: Research and Applications, (2013) n/a-n/a.

[32] R.K. Pandey, S. Sahu, S. Chandra, Hdbk of Semiconductor Electrodeposition, CRC PressI Llc, 1996.

[33] C.D. Lokhande, S.H. Pawar, physica status solidi (a), 111 (1989) 17-40.

[34] Pourbaix, M. (1974). Atlas of electrochemical equilibria in aqueous solutions. M. Pourbaix, published 1974 by NACE, 644.

[35] J.J. Scragg, P.J. Dale, L.M. Peter, Electrochemistry Communications, 10 (2008) 639-642.

[36] D. Lincot, H.G. Meier, J. Kessler, J. Vedel, B. Dimmler, H.W. Schock, Sol Energ Mater, 20 (1990) 67-79.

[37] H.C. Ye, H.S. Park, V.A. Akhavan, B.W. Goodfellow, M.G. Panthani, B.A. Korgel, A.J. Bard, J Phys Chem C, 115 (2011) 234-240.

[38] A. Paracchino, J.C. Brauer, J.E. Moser, E. Thimsen, M. Graetzel, J Phys Chem C, 116 (2012) 7341-7350.

[39] R.C. Alkire, D.M. Kolb, J. Lipkowski, P. Ross, Photoelectrochemical Materials and Energy Conversion Processes, Wiley-VCH, 2010.

[40] S. Ikeda, T. Nakamura, S.M. Lee, T. Yagi, T. Harada, T. Minegishi, M. Matsumura, Chemsuschem, 4 (2011) 262-268.

[41] M.D. Archer, A.J. Nozik, Nanostructured and photoelectrochemical systems for solar photon conversion, Imperial College Press London, 2008.

[42] W. W. Gartner, Physical Review, 116 (1959) 84.

Chapter 2

Electrochemical Deposition of $Cu_2ZnSnSe_4$ Thin Films

2.1. Single–step Electrodeposition of a Microcrystalline $Cu_2ZnSnSe_4$ Thin Film

2.1.1. Introduction

Kesterites, Cu_2ZnSnS_4 (CZTS), $Cu_2ZnSnSe_4$ (CZTSe) and their alloys ($Cu_2ZnSn(S,Se)_4$) (CZTSSe)), are regarded as promising absorber materials for future photovoltaic systems on a terra–watt scale[1-3]. These materials have band gap energies ranging from 1.0 eV to 1.5 eV[4-6], which match well with the optimal spectral range of solar radiation. The high absorption coefficients of these materials ($> 10^4$ cm^{-1})[4,7] assure absorption of the entire incident photon flux in an absorber layer as thin as a few microns. Moreover, they consist of earth–abundant and inexpensive elements and would thus not have problems on material shortages and high–cost limitations[1,8]. The latest conversion efficiency of 11.1%[9] has encouraged numerous investigations to search for more feasible and low–cost production methods for large–scale employment of kesterite solar cells.

Electrodeposition is one of the promising technologies for fabrication of low–cost photovoltaic absorber films because of the low–cost equipment, scalability of large scale, and good control over film composition and morphology. As has been reported for fabrication of *p*–type photovoltaic absorber materials, *e.g.*, $Cu(In,Ga)Se_2$ (CIGS)[10-12], CdTe[13] and Cu_2O[14,15], the simplest process is single–step electrodeposition to form a semiconductor film directly. In the case of electrodeposited kesterite devices, however, a sequential route, consisting of electrodeposition of a Cu–Zn–Sn stacked layer[16] or a Cu–Zn–Sn alloy[17] followed by sulfurization, is often employed; there have been a few report on fabrication of kesterite compounds from single–step electrodeposition[18,19]. Pawar *et al.* reported an electrodeposition of CZTS from the solution containing $CuSO_4$, $ZnSO_4$, $SnSO_4$, and $Na_2S_2O_3$ with tri–sodium citrate and tartaric acid as complexing agents, and further annealing at 550 °C under Ar atmospheres to improve the film crystallinity [18]. Similarly, Cui *et al.* reported an approach to fabricate CZTS by annealing under H_2S atmosphere of an electrodeposited film containing alloy of Cu–Zn–Sn-S [19]. Both of these single–step electrodepositions were performed in solutions containing sulfur as a chalcogen source; there has been no detailed report on an attempt to fabricate a kesterite film from a solution containing selenium, despite many studies on fabrication of the above–mentioned CIGS film.

In this study, therefore, we examined the possibility of fabrication of a CZTSe film by single–step electrodeposition from a Cu–Zn–Sn–Se–containing electrolyte. Effects of applied potentials on film compositions and morphologies were studied in detail. Mechanistic aspects of the formation and growth of a CZTSe film were also assessed. In addition, we attempted to fabricate quinary CZTSSe films by sulfurization of the electrodeposited film; electronic and optical properties of the thus-obtained films were also examined by using photoelectrochemical measurement.

2.1.2. Experimental

2.1.2.1 Material synthesis

Electrodeposition was carried out potentiostatically in a vertical three–electrode setup consisting of an Ag/AgCl reference electrode, a Pt–sheet counter electrode, and a Mo–coated glass substrate (Mo/glass) as a working electrode. Before the deposition, the Mo/glass substrate was pre–cleaned by sonication in acetone. The working electrode area was 0.7 cm^2. The distance between the working and counter electrodes was kept constant at about 2 cm. The electrolyte used consisted of 4 mM $CuSO_4$, 80 mM $ZnSO_4$, 20 mM $SnCl_4$, 5 mM Na_2SeO_3 and 500 mM lactic acid. The initial pH of the electrolyte was *ca.* 1.3 and then carefully adjusted to 2.5–2.6 by addition of aqueous NH_3 solution (28%). Electrodeposition was performed to obtain thin films with thicknesses of *ca.* 1.6–1.9 μm at a potential of –0.1 V to –0.6 V (*vs.*

Ag/AgCl) for 60 min at room temperature without stirring using a Hokuto Denko HSV–110 potentiostat-galvanostat. Temperature of all deposition solutions was kept at 24±1 °C by immersion in a thermostatted water bath. No precipitate appeared from the electrolyte after keeping for one week at room temperature. The film deposited at –0.6 V (*vs.* Ag/AgCl) was finally subjected to sulfurization at various temperatures (450 °C–550 °C) under H_2S (5% in Ar) flow for 10 min.

2.1.2.2 Characterizations

Elemental compositions of thus–obtained films were determined using a Hitachi TM3000 scanning electron microscope (SEM) equipped with a SwiftED3000 energy dispersive X–ray spectrometer (EDX). Crystal structures were measured by X–ray diffraction (XRD) analysis using a Rigaku MiniFlex X–ray diffractometer (Cu Kα, Ni filter). Crystalline phase compositions were determined by Raman spectroscopy using a JASCO NRS–3100 Laser Raman Spectrophotometer with a laser wavelength of 532 nm. Surface and cross–sectional morphologies of the films after sulfurization were examined using a Hitachi S–5000 FEG field emission scanning electron microscope (FE–SEM).

Photoelectrochemical measurements were carried out using a three–electrode cell in 0.2 M $Eu(NO_3)_3$ (pH 4) electrolyte[20,21]. A Pt wire and an Ag/AgCl electrode in saturated KCl served as the counter electrode and reference electrode, respectively, and a Hokuto Denko HB–151 potentio–galvanostat was employed to obtain voltammograms. Photocurrents were measured using the lock–in technique to obtain an external quantum efficiency (*EQE*) spectrum. Sample electrodes were illuminated with a monochromatic light of variable wavelength chopped at a frequency of 10 Hz. The number of incident photons was determined with an OPHIR Orion Laser power meter equipped with a photodiode. Before the photoelectrochemical measurements, the sulfurized films were treated with a 10% KCN solution to clean the surface[22-24].

2.1.3. Results and discussion

2.1.3.1. Dependence of film compositions and structures on deposition potentials

Fig. 1a shows a cyclic voltammogram (*CV*) in the electrolyte containing Cu(II), Zn(II), Sn(IV) and Se(IV) species (see experimental) at potentials ranging from +0.15 V to –0.80 V (*vs.* Ag/AgCl) and a scan rate of 10 mV s^{-1}. A steep rise of cathodic current was observed from the beginning of the sweep (+0.15 V (*vs.* Ag/AgCl)) followed by a plateau region between 0 V and –0.20 V (*vs.* Ag/AgCl). The second reduction process started at –0.2 V (*vs.* Ag/AgCl) and peaked at –0.35 V (*vs.* Ag/AgCl). Then the cathodic current again reach a plateau region until a steep rise at applied potentials more negative than –0.60 V (*vs.* Ag/AgCl). In addition, an appreciable anodic peak was observed at –0.40 V (*vs.* Ag/AgCl) in the anodic scan. From these observations, therefore, there are three main regions inducing several deposition reactions, while the last highly negative potential region should also include significant contribution of H_2 evolution. Due to the complexity of the present electrolyte, *i.e.*, containing four different species to be reduced, these reduction processes were not easily assignable. Hence, compositional and structural characteristics of the films deposited with chronoamperometry mode with potentials ranging from –0.10 V to –0.60 V (vs. Ag/AgCl) for 60 min were examined. As can be seen in the chronoamperograms (Fig. 1b), the typical current density–time responses of the depositions exhibited current plateau regardless of the applied potentials, which is commonly observed for the electrodeposition controlled by convective mass–transfer[25,26].

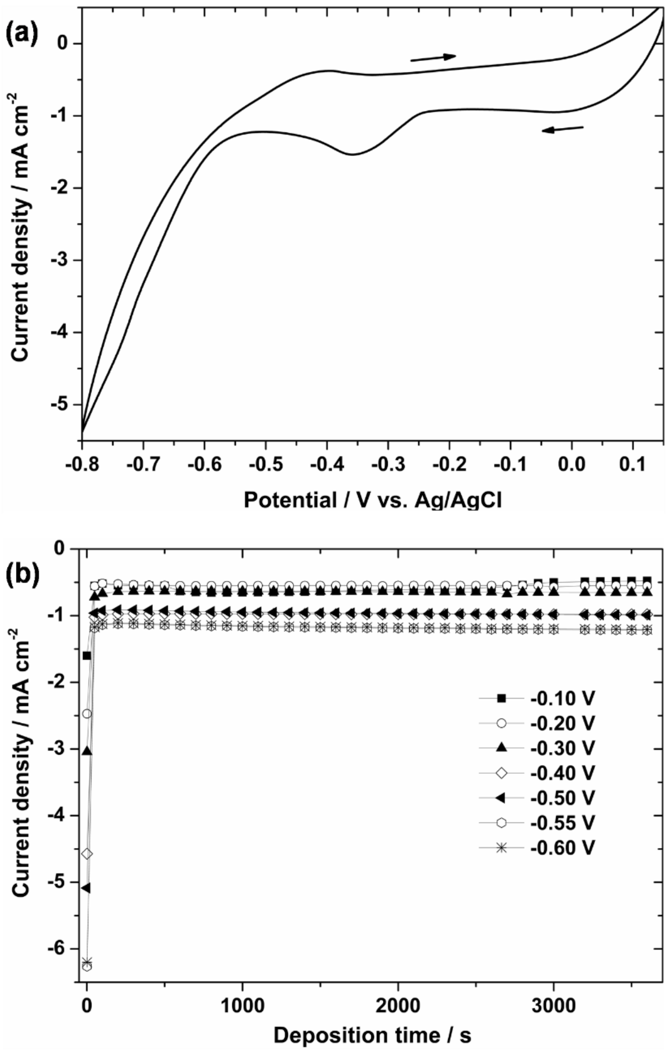

Figure 1. (a) Cyclic voltammogram of a Mo/glass substrate immersed in an electrolyte containing Cu(II), Zn(II), Sn(IV) and Se(IV) species. Scan rate: 10 mV s^{-1}. Arrows indicate scan directions. (b) chronoamperograms during the electrodeposition with potentials ranging from –0.10 V to –0.60 V (vs. Ag/AgCl) for 60 min.

Fig. 2 shows Cu, Zn, Sn and Se compositions in as–deposited films as a function of applied potentials measured by EDX. XRD patterns and Raman spectra of these films are also shown in Figs. 3 and 4, respectively. The films deposited at potentials more positive than –0.20 V (*vs.* Ag/AgCl) consisted of Cu and Se elements without incorporation of Zn and Sn, as expected from differences in their standard electrode potentials, as shown in Table 1[27]. XRD analyses revealed that these films were mainly composed of CuSe (JCPDS 34–0171), $Cu_{1.8}Se$ (JCPDS 88–2046), and elemental Se (JCPDS 47–1515), as shown in Figs. 3a and 3b. Raman spectra of these films (Figs. 4a and 4b) also indicated an intense peak assignable to a Cu–Se binary compound at 263 cm^{-1} and its corresponding weak peak at 187 cm^{-1}[28], along with a moderate peak due to trigonal selenium at 240 cm^{-1}[29]. As is analogized from the Pourbaix diagram of the copper–selenium system proposed by Thouin *et al.*[30], probable main reactions in the present system at the potential range are as follows:

$$\mathrm{Cu(II)} + \mathrm{Se(IV)} + 6\mathrm{H}^+ + 6e^- \rightarrow \mathrm{CuSe} + 3\mathrm{H_2O}, \quad (2.1.1)$$

$$\mathrm{Se(IV)} + 6\mathrm{H}^+ + 4e^- \rightarrow \mathrm{Se} + 3\mathrm{H_2O}, \quad (2.1.2)$$

$$(1+x)\mathrm{CuSe} + xe^- \rightarrow \mathrm{Cu}_{1+x}\mathrm{Se} + x\mathrm{Se(–II)}\ (x = 0.8). \quad (2.1.3)$$

Hence, reduction processes shown in the *CV* at potentials ranging from 0.15 V to –0.20 V (*vs.* Ag/AgCl) (see Fig. 1a) were mainly attributed to reactions (2.1.1)–(2.1.3).

Table 1. Standard reduction potentials of the related ions[27].

Reduction reactions	E° / V vs. Ag/AgCl
$Cu^{2+} + 2e^- \rightarrow Cu$	0.14
$Zn^{2+} + 2e^- \rightarrow Zn$	-0.96
$Sn^{4+} + 2e^- \rightarrow Sn^{2+}$	-0.04
$Sn^{2+} + 2e^- \rightarrow Sn$	-0.33
$H_2SeO_3 + 4H^+ + 4e^- \rightarrow Se + 3H_2O$	0.54

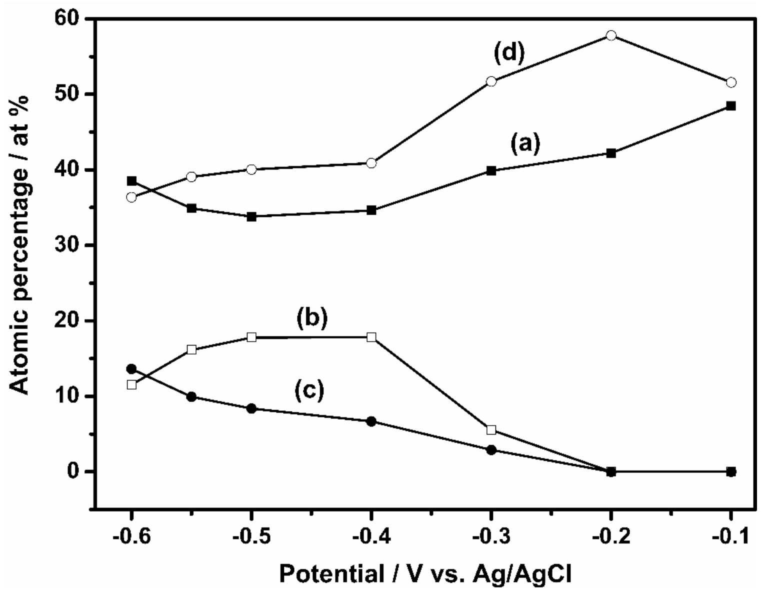

Figure 2. Atomic composition of the as–deposited films as a function of applied potentials: (a) Cu, (b) Zn, (c) Sn, and (d) Se.

When the film was prepared at –0.30 V (*vs.* Ag/AgCl), only two weak reflections of elemental Se were observed; reflections of Cu–Se binary compounds disappeared in its XRD pattern (Fig. 3c). The corresponding Raman spectrum shown in Fig. 4c exhibits decreases in peak intensities of both these binary compounds and elemental Se, along with appearance of a new broad peak at around 190 cm^{-1}. As has been reported in the literature[28], further increase in the Cu/Se chemical ratio from 1–1.8 (CuSe and $Cu_{1.8}Se$) to 2 (Cu_2Se) resulted in disappearance of their Raman signal due to low Raman scattering efficiency of the Cu_2Se compound. Hence, reduction of the 263 cm^{-1} peak is attributed to reduction of Cu–Se binary compounds to form Cu_2Se. Moreover, the newly appearing 190 cm^{-1} peak is assignable to the A1–mode peak commonly observed for CZTSe[31,32], indicating formation of the quaternary CZTSe. Indeed, incorporation of both Zn and Sn components in the films started at this potential, as confirmed by results of EDX analysis shown in Fig. 2. In addition, decrease in the peak intensity of trigonal Se is likely to be compensation of as–formed Se by the CZTSe formation through several reduction processes (see below).

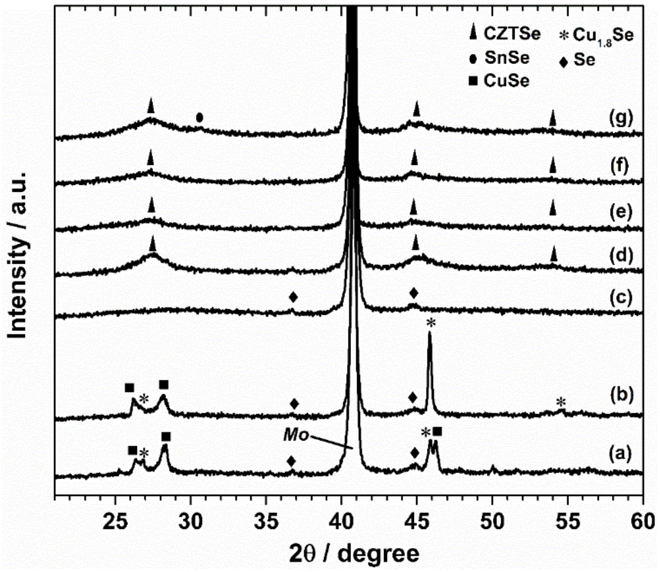

Figure 3. XRD of the as–deposited films obtained at (a) –0.10 V, (b) –0.20 V, (c) –0.30 V, (d) –0.40 V, (e) –0.50 V, (f) –0.55 V, and (g) –0.60 V (*vs.* Ag/AgCl).

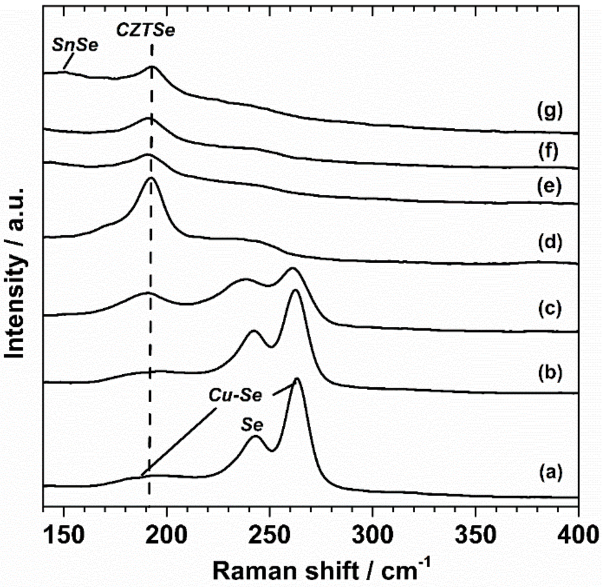

Figure 4. Raman spectra of the as-deposited films obtained at (a) –0.10 V, (b) –0.20 V, (c) –0.30 V, (d) –0.40 V, (e) –0.50 V, (f) –0.55 V, and (g) –0.60 V (*vs.* Ag/AgCl).

When the applied potentials went into a more negative region (–0.40 V to –0.55 V (*vs.* Ag/AgCl)), contents of Zn and Sn elements in thus–obtained films significantly increased (Fig. 2). As shown in Figs. 3d–3f, XRD patterns of these films showed appearances of three broad reflections at 2θ of 27°, 45° and 53°, all of which corresponded well to those of CZTSe (JCPDS 52–0868) with crystal orientations of (112), (220) and (312), respectively. Although other compounds such as ZnSe and Cu_2SnSe_3 should give the same diffraction patterns because of similar crystal structures similar to that of CZTSe, observations of the dominant peak of A1–mode CZTSe in their Raman spectra (Figs. 4d–4f) strongly support depositions of CZTSe films as the main component in this applied potential region. As for the film deposited at –0.60 V (*vs.* Ag/AgCl), a weak reflection at 2θ of 30.5° in the XRD pattern and a broad peak at around 150 cm^{-1} in the Raman spectrum assignable to the binary SnSe compound[33] were also detected. An appreciable increase in the Sn content in the film (see Fig. 2) is attributable to the formation of this secondary phase.

We have not yet obtained a film with a stoichiometric composition of CZTSe (*i.e.*, Cu/Zn/Sn/Se=25/12.5/12.5/50): all of the films containing Cu, Zn, Sn and Se elements have a relatively Cu–rich composition (see Fig. 2), despite appearances of a single–phase XRD pattern and Raman spectrum of CZTSe in the films obtained at applied potentials ranging from –0.40 V and –0.55 V (*vs.* Ag/AgCl). This discrepancy implies the existence of another Cu–containing secondary phase undetected by these structural analyses. The residual component is probably in the form of the monovalent selenide analogue, Cu_2Se. As mentioned above, Cu_2Se was formed by reduction of Cu–Se binary compounds, *i.e.*, CuSe and $Cu_{1+x}Se$ ($x = 0.8$):

$$2CuSe + 2e^- \rightarrow Cu_2Se + Se(-II) \tag{2.1.4}$$

$$(2/(1+x))Cu_{1+x}Se + ((1-x)/(1+x))e^- \rightarrow Cu_2Se + ((1-x)/(1+x))Se(-II)\ (x = 0.8). \tag{2.1.5}$$

In addition to these processes, Cu_2Se can also be produced by reaction between Cu(II) and reactive Se components, such as trigonal Se[30,34] and Se(–II) derived from the trigonal Se, as given by:

$$2Cu(II) + Se + 4e^- \rightarrow Cu_2Se \tag{2.1.6}$$

$$2Cu(II) + Se(-II) + 2e^- \rightarrow Cu_2Se. \tag{2.1.7}$$

The absence of any reflections of the Cu_2Se compound in the above XRD patterns implies low crystalline nature of this compound. As mentioned above, low Raman scattering efficiency of the compound[28] also resulted in no detection of the above Raman spectra.

Incorporation of Zn and Sn elements into the films was observed even at more positive applied potentials than standard electrode potentials of these elements, especially for the Zn component (Table 1). Thus, underpotential depositions of these elements should be facilitated by the reaction with Se species, in a fashion similar to incorporation of In and Ga components in the Cu–In–Ga–Se system[10,11,35]. In the Cu–In–Ga–Se system, the advantage of the addition of tetravalent Se(IV) lies in the ease of formation of binary selenide compounds due to their large formation energies (Cu_2Se (–104 kJ mol^{-1}), In_2Se_3 (–386 kJ mol^{-1}), Ga_2Se_3 (–418 kJ mol^{-1})); this leads to simultaneous deposition of the Cu–In–Ga–Se elements at wider potential ranges to form $Cu(In,Ga)Se_2$, despite significantly negative standard electrode potentials of In and Ga redox systems (–0.53 V (*vs.* Ag/AgCl) for In and –0.75 V (*vs.* Ag/AgCl) for Ga)[27]. This type of co–deposition mechanism, known as the Kroger mechanism[36], also explained successful syntheses of other selenide and telluride compounds such as ZnSe[37] and CdTe[38,39]. Due to the easiness of formation of the Zn and Sn selenide compounds (–

154.938 kJ mol^{-1} for ZnSe and –109.997 kJ mol^{-1} for $SnSe_2$)[40, 41], therefore, inclusion of Zn and Sn in the present Cu–Zn–Sn–Se system is expected to follow a mechanism similar to that for the Cu–In–Ga–Se system.

Based on the above compositional analyses, cathodic currents observed in the above *CV* (Fig. 1a) at potentials ranging from –0.20 V to –0.60 V (*vs.* Ag/AgCl) are assigned to be derived from formation of mixed compounds of Cu_2Se, ZnSe, and $SnSe_2$, while the exact potentials of these deposition processes cannot be determined due to the overlap of these processes in this potential region. Hence, production of the CZTSe phase is given by the following equation:

$$Cu_2Se + ZnSe + SnSe_2 \rightarrow Cu_2ZnSnSe_4. \qquad (2.1.8)$$

In order to induce stationary CZTSe deposition, continuous production of these binary selenides is required. However, a separate electrodeposition experiment from the electrolyte containing Cu(II) and Se(IV) at –0.60 V (*vs.* Ag/AgCl) did not produce Cu_2Se: it produced a higher oxidation state of binary Cu–Se compounds such as CuSe and $Cu_{1.8}Se$. Moreover, when the same potential was applied, there was no appreciable production of ZnSe and $SnSe_2$ from electrolytes containing Zn(II)/Se(IV) and Sn(IV)/Se(IV), respectively; the major deposition product from these electrolytes was passive red selenium, an unreactive insulating compound different from the trigonal Se. These results suggest that the presence of Cu(II), Zn(II), and Sn(IV) species components in the solution was necessary to induce efficient deposition of Cu_2Se, ZnSe, and $SnSe_2$ and thus the codeposition of CZTSe. Similar to the production of Cu_2Se as mentioned above, ZnSe and $SnSe_2$ would be formed by reaction with reactive Se species (*i.e.*, trigonal Se and Se(–II)) as follows:

$$\mathrm{Zn(II)} + \mathrm{Se} + 2e^{-} \rightarrow \mathrm{ZnSe} \quad (2.1.9)$$

$$\mathrm{Zn(II)} + \mathrm{Se(-II)} \rightarrow \mathrm{ZnSe} \quad (2.1.10)$$

$$\mathrm{Sn(IV)} + 2\mathrm{Se} + 4e^{-} \rightarrow \mathrm{SnSe_2} \quad (2.1.11)$$

$$\mathrm{Sn(IV)} + 2\mathrm{Se(-II)} \rightarrow \mathrm{SnSe_2}. \quad (2.1.12)$$

In regard to the Sn incorporation, moreover, it is also probable that reactions between Sn metal and Se proceed due to the sufficient potential to deposit Sn metal[42]: this process would induce $SnSe_2$ as well as SnSe. Moreover, other possible pathways for the latter SnSe compound can be considered, *e.g.*, reduction of $SnSe_2$ and reaction between Sn(II) formed from Sn(IV) and Se(–II). Appreciable production of SnSe at a highly negative applied potential (–0.60 V (*vs.* Ag/AgCl)) is likely to be attributed to frequent occurrence of these reactions.

For the further examination of characteristics of the as–deposited film, we measured the atomic composition of the film deposited at –0.60 V at various deposition times ranging from 5 min to 60 min; these results are shown in Fig. 5. As deposition time goes on, gradual increases of Cu and Sn atomic percentages on the film and the opposite for Zn and Se, reaching the composition of Cu (38.5%), Zn (11.5%), Sn (13.6%) and Se (36.4%) at 60–min deposition, were observed. Although the cause of the composition gradient is not clear at present, this indicates presence of a perpendicular compositional gradient in the as–deposited film. A similar composition gradient along the thickness of the as–deposited film was also observed for the single–step electrodeposition of $CuInSe_2$ film[25,43].

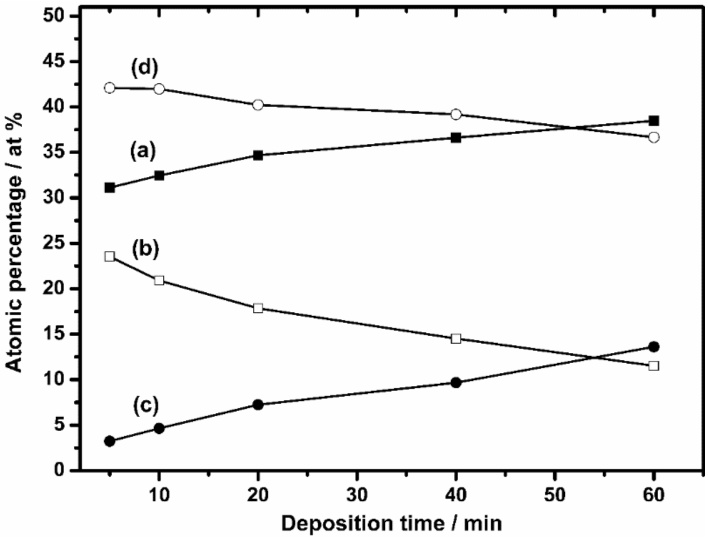

Figure 5. Atomic composition of the film deposited at –0.60 V (*vs.* Ag/AgCl) as a function of deposition time: (a) Cu, (b) Zn, (c) Sn, and (d) Se.

2.1.3.2. Sulfurization of the films

The as–deposited film was then sulfurized to induce grain growth, as well as to investigate effects of the sulfur addition to the film to obtain a quinary CZTSSe film. As has been reported in the literature[31], appropriate Zn/Sn ratios of the series of kesterites for their solar cell applications are *ca.* 1.1 to 1.3. Since appreciable loss of Sn is commonly observed during high–temperature heat treatment for synthesis of kesterite due to the volatily of Sn, a precursor film with a sufficient Zn/Sn ratio to compensate the loss of Sn is required. Therefore, we chose the film deposited at applied potential of –0.60 V (*vs.* Ag/AgCl) for 60 min with a Zn/Sn ratio of *ca.* 0.85 with a thickness of *ca.* 1.7 μm for sulfurization, although the film contained appreciable SnSe secondary phases. Fig. 6 shows surface and cross–sectional SEM images of the precursor film and that sulfurized under H_2S flow at different temperatures. An SEM image of the surface of the as–deposited film without sulfurization shows micron-sized granular particles that are homogeneously deposited without any appreciable cracks and voids (Fig. 6a);

corresponding cross–section exhibits a rough structure (Fig. 6e). As shown in Figs. 6b and 6c, sulfurization at 450 °C and 500 °C induced reduction of the granular shape, leading to gradual changes into smooth surface morphologies. Their cross–sectional images indicate occurrence of crystalline growth accompanied by formation of voids between the film and Mo/glass substrate (Figs. 6f and 6g). Although sulfurization at a higher temperature (550 °C) resulted in further grain growth, formation of voids and cracks became significant, as shown in Figs. 6d and 6h. Indeed, some of the 550–°C sulfurized film was peeled off from the Mo/glass substrate.

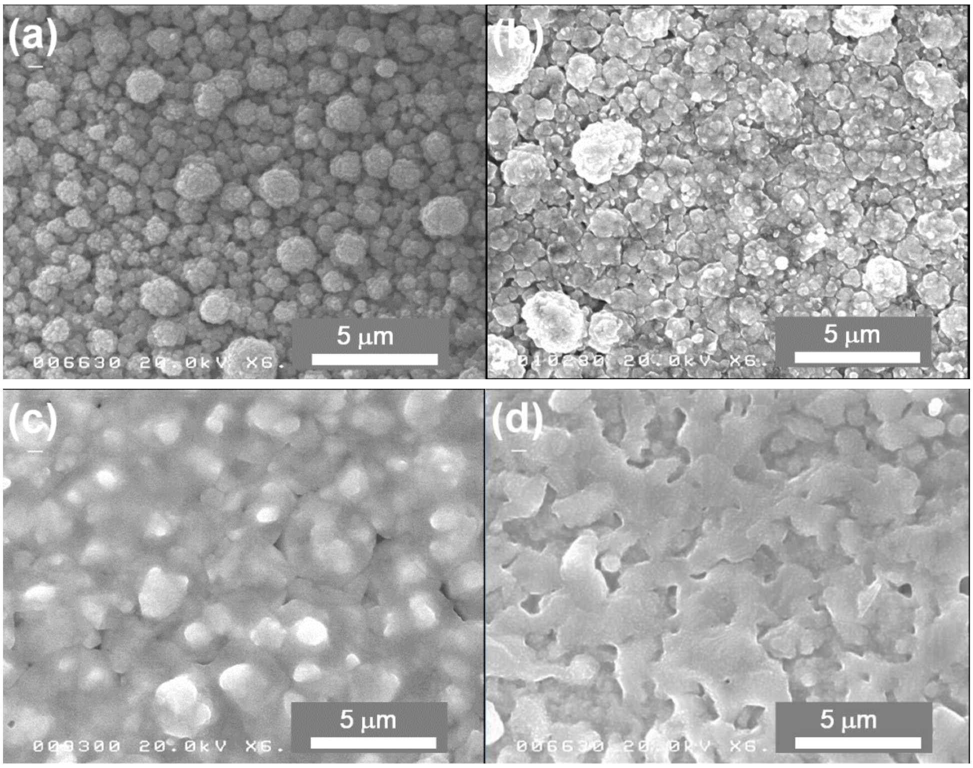

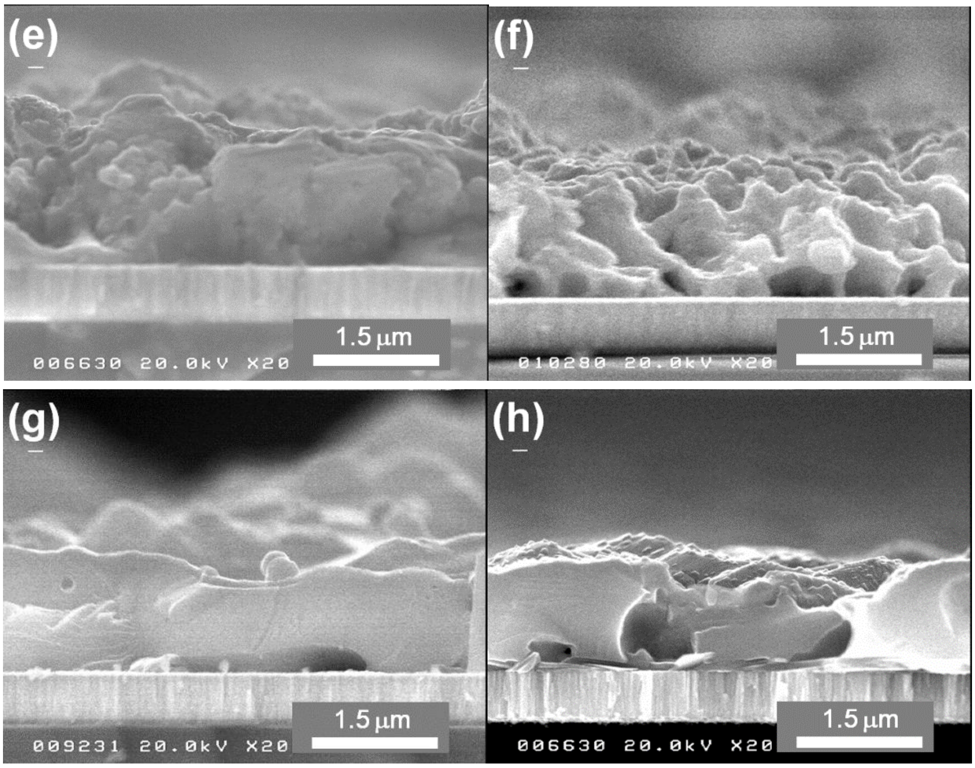

Figure. 6. Surface and cross–sectional SEM images of the films (a,e) before sulfurization and after sulfurization under H_2S flow at (b,f) 450 °C, (c,g) 500 °C, and (d,h) 550 °C.

Fig. 7 shows XRD patterns of the annealed films. The 450–°C sulfurized film shown in Fig. 6a indicates several reflections assignable to the kesterite crystal with (112), (200), (211), (105), (220), (312), and (008) planes together with reflections of the SnSe phase (JCPDS 32–1382). When the sulfurization temperature was increased, the SnSe component disappeared; XRD patterns of films sulfurized at 500 °C and 550 °C corresponded well to that of the pure sulfide analogue, CZTS (JCPDS 26–0575), indicating replacement of the Se component with S during high temperature sulfurization. As determined by EDX analyses, high S/(S+Se) ratios of 500–°C and 550–°C sulfurized films (*i.e.*, 0.82 and 0.86, respectively) support the results. Meanwhile, Cu/(Zn+Sn) and Zn/Sn ratios of these films (Cu/(Zn+Sn) = 1.16 and Zn/Sn = 1.19 for the 500–°C annealed film, Cu/(Zn+Sn) = 1.15 and Zn/Sn = 1.16 for the 550–°C annealed film) were slightly Cu–rich and Zn–rich compositions compared to the stoichiometric composition. Corresponding Raman spectra of these films indicate appreciable peaks similar to the pure sulfide CZTS (338 cm^{-1}, 288 cm^{-1}, and 367 cm^{-1})[31,44], along with a weak peak at 240 cm^{-1}, as shown in Fig. 8. Observations of the former peaks should be due to the high sulfur content of the present CZTSSe. The latter weak peak is likely to be derived from a "CZTSe–like" component in the mixed compound of sulfide and selenide (*i.e.*, CZTSSe) in accordance with the literature[31,45,46]. The fact that the peak position of the CZTSe–like component shifted significantly from that of pure selenide (194 cm^{-1})[32] is also consistent with the high S content in the present CZTSSe. In addition, Raman peaks of the present films are rather broad, suggesting insufficient crystallinity and presence of large amounts of bulk defects[47].

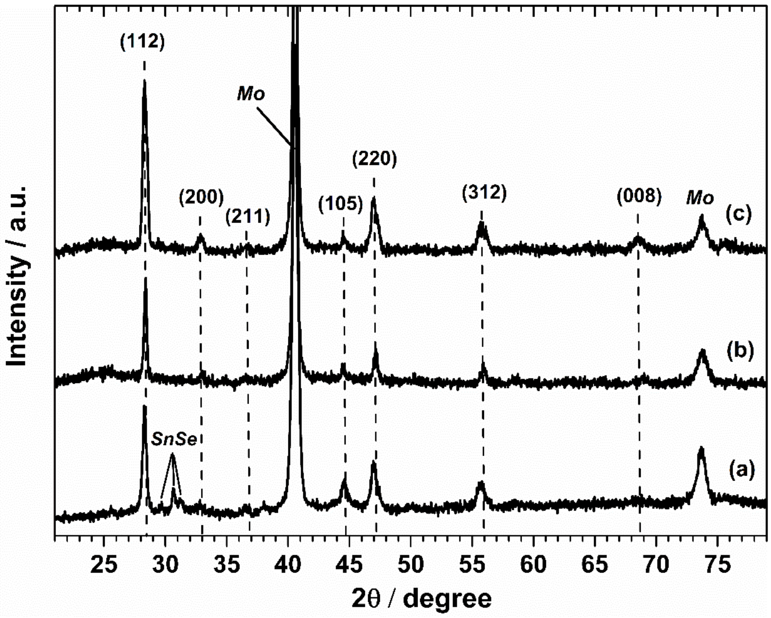

Figure 7. XRD patterns of films sulfurized at (a) 450 °C, (b) 500 °C, and (c) 550 °C.

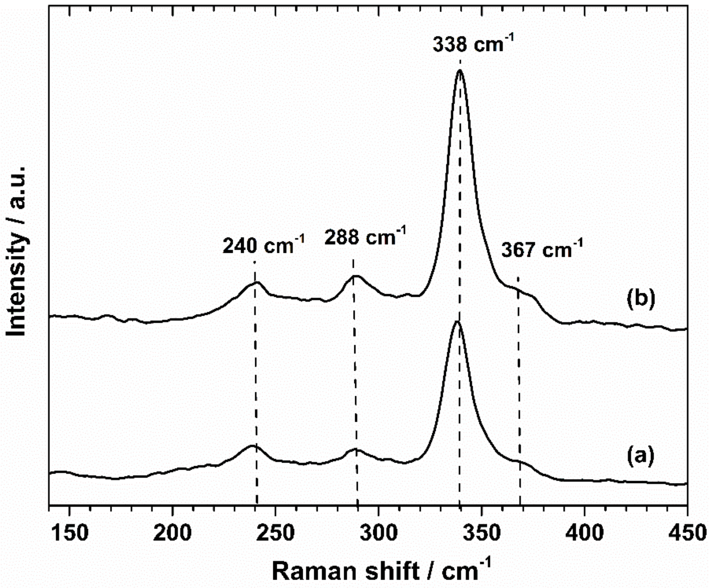

Figure 8. Raman spectra of films sulfurized at (a) 500 °C and (b) 550 °C.

2.1.3.3. Photoelectrochemical measurement

The photocurrent–voltage characteristics of CZTSSe films obtained by different sulfurization temperatures were examined by linear sweep voltammetry (*LSV*) in an aqueous Eu^{3+} solution under chopped illumination at potentials from 0 V to –0.45 V (*vs.* Ag/AgCl). Fig. 9 shows the results. Since cathodic photocurrents appeared on all CZTSSe films, they behaved as *p*–type semiconductor electrodes. It is evident that the magnitude of the photocurrents from the films sulfurized at 500 °C and 550 °C was significantly higher than that of the film sulfurized at a lower temperature (450 °C), as can be expected from the absence of significant secondary phases from these films as well as their well–grown grains. The relatively small photoresponse of the 550–°C sulfurized film compared to that of the 500–°C sulfurized film was probably due to the presence of significant voids in the film. It should be noted that we also observed transient spike photoresponses on the 500–°C and 550–°C sulfurized films. As has been discussed in CIGS and other *p*–type compound semiconductor electrodes, this transient spike can be related to several reasons such as sluggish charge transfer in the solution[20] or recombination on the surface (surface states) and/or bulk[20,48,49].

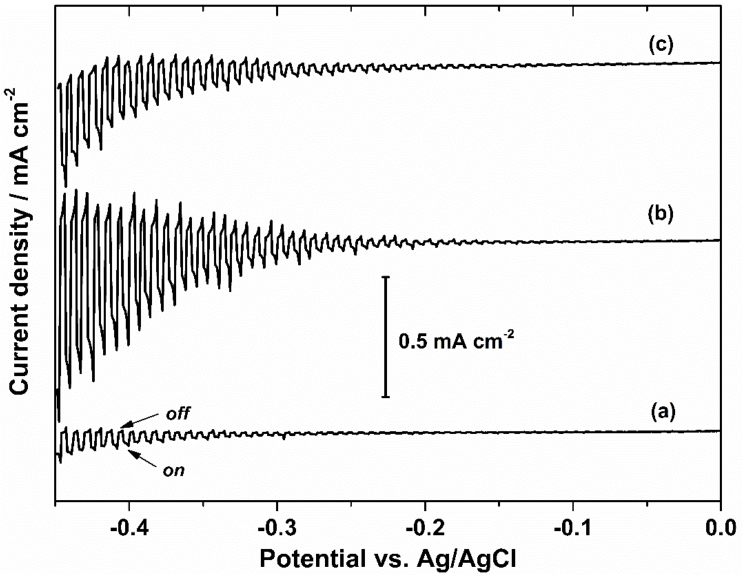

Figure 9. Photovoltammetry graphs of films sulfurized at (a) 450 °C, (b) 500 °C, and (c) 550 °C under chopped light illumination in a 0.2 M $Eu(NO_3)_3$ electrolyte. The scans were performed at cathodic directions.

Fig. 10 shows an *EQE* spectrum of the 500–°C sulfurized film measured at –0.40 V (*vs.* Ag/AgCl). Due to the very small photocurrent signals of the other annealed films, *EQE* spectra of those films were difficult to obtain: these were not measured. The *EQE* spectrum of the 500–°C sulfurized film has an onset at 1.34 eV (*ca.* 930 nm) and gradually rises to higher photon energy up to 2.07 eV (*ca.* 600 nm), suggesting excess carrier concentration of the film. As mentioned above, the present CZTSSe film should contain appreciable defects in the bulk as well as on the surface. Hence, such a high carrier concentration would be due to these structural failures, leading to reduction of the minority carrier diffusion length. Moreover, the fact that the *EQE* onset photon energy is much longer than the band gap energy of CZTSSe reported in the literature (*i.e.*, 1.41–1.48 eV for CZTSSe with S/(S+Se) ratios of *ca.* 0.80–0.9)[6,47] implies the presence of appreciable amounts of sub–gap states near the band edge in the present film. In order to achieve an efficient photovoltaic property, therefore, qualities of the present CZTSSe films would be insufficient: thus, further investigations to improve film properties are required.

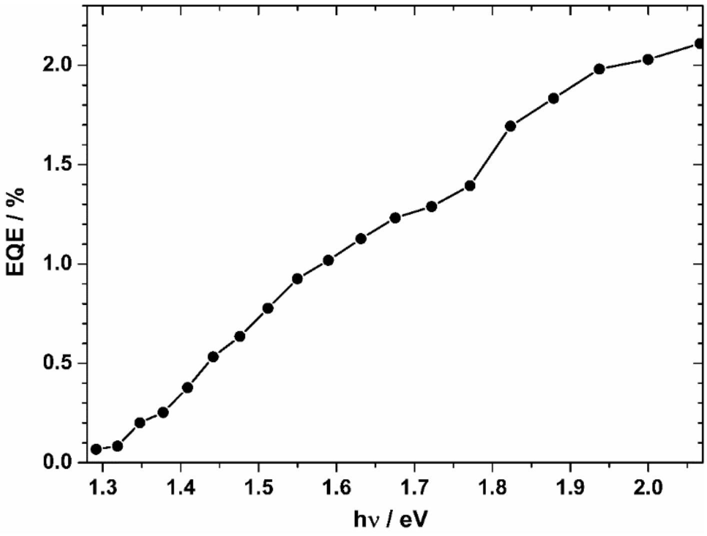

Figure 10. External quantum efficiency spectrum of the film sulfurized at 500 °C.

2.1.4. Conclusion

In the present study, single–step electrodeposition of a CZTSe film from an acidic electrolyte containing Cu(II), Zn(II), Sn(IV), and Se(IV) species was examined. Deposition of the desired CZTSe film as the main compound was achieved by fixing appropriate applied potentials. Mechanistic studies suggested that CZTSe was formed by reactions among the corresponding binary selenides, Cu_2Se, ZnSe, and $SnSe_2$. Upon sulfurization of the as–deposited film, we successfully fabricated *p*–type CZTSSe as a single phase when the sulfurization temperatures were higher than 500 °C. This initial finding should open a new possible pathway to prepare kesterite thin films from simple single–step electrodeposition of a quaternary precursor. Although structural, electronic and photoelectrochemical characteristics of the present film suggest insufficient quality for photovoltaic application, optimizations of the electrolyte and electrodeposition conditions as well as the sulfurization parameters would lead to improvements of these properties.

References

[1] L.M. Peter, Philosophical transactions. Series A, Mathematical, physical, and engineering sciences, 369 (2011) 1840-1856.

[2] T. Todorov, O. Gunawan, S.J. Chey, T.G. de Monsabert, A. Prabhakar, D.B. Mitzi, Thin Solid Films, 519 (2011) 7378-7381.

[3] B.K. Meyer, P.J. Klar, Phys Status Solidi-R, 5 (2011) 318-323.

[4] H. Katagiri, K. Saitoh, T. Washio, H. Shinohara, T. Kurumadani, S. Miyajima, Solar Energy Materials and Solar Cells, 65 (2001) 141-148.

[5] T.M. Friedlmeier, H. Dittrich, H.W. Schock, Inst Phys Conf Ser, 152 (1998) 345-348.

[6] S. Chen, A. Walsh, J.-H. Yang, X. Gong, L. Sun, P.-X. Yang, J.-H. Chu, S.-H. Wei, Physical Review B, 83 (2011) 125201.

[7] K. Ito, T. Nakazawa, Jpn J Appl Phys 1, 27 (1988) 2094-2097.

[8] C. Wadia, A.P. Alivisatos, D.M. Kammen, Environ Sci Technol, 43 (2009) 2072-2077.

[9] T.K. Todorov, J. Tang, S. Bag, O. Gunawan, T. Gokmen, Y. Zhu, D.B. Mitzi, Advanced Energy Materials, DOI: 10.1002/aenm.201200348.

[10] D. Lincot, J.F. Guillemoles, S. Taunier, D. Guimard, J. Sicx-Kurdi, A. Chaumont, O. Roussel, O. Ramdani, C. Hubert, J.P. Fauvarque, N. Bodereau, L. Parissi, P. Panheleux, P. Fanouillere, N. Naghavi, P.P. Grand, M. Benfarah, P. Mogensen, O. Kerrec, Solar Energy, 77

(2004) 725-737.

[11] R.N. Bhattacharya, H. Wiesner, T.A. Berens, J. Matson, J. Keane, K. Ramanathan, A. Swartzlander, A. Mason, R.N. Noufi, J Electrochem Soc, 144 (1997) 1376-1379.

[12] C.J. Hibberd, E. Chassaing, W. Liu, D.B. Mitzi, D. Lincot, A.N. Tiwari, Prog Photovoltaics, 18 (2010) 434-452.

[13] N.W. Duffy, L.M. Peter, R.L. Wang, D.W. Lane, K.D. Rogers, Electrochimica Acta, 45 (2000) 3355-3365.

[14] M. Izaki, T. Shinagawa, K.-T. Mizuno, Y. Ida, M. Inaba, A. Tasaka, Journal of Physics D: Applied Physics, 40 (2007) 3326-3329.

[15] W. Septina, S. Ikeda, M.A. Khan, T. Hirai, T. Harada, M. Matsumura, L.M. Peter, Electrochimica Acta, 56 (2011) 4882-4888.

[16] S. Ahmed, K.B. Reuter, O. Gunawan, L. Guo, L.T. Romankiw, H. Deligianni, Advanced Energy Materials, 2 (2012) 253-259.

[17] A. Ennaoui, M. Lux-Steiner, A. Weber, D. Abou-Ras, I. Kotschau, H.W. Schock, R. Schurr, A. Holzing, S. Jost, R. Hock, T. Voss, J. Schulze, A. Kirbs, Thin Solid Films, 517 (2009) 2511-2514.

[18] S.M. Pawar, B.S. Pawar, A.V. Moholkar, D.S. Choi, J.H. Yun, J.H. Moon, S.S. Kolekar, J.H. Kim, Electrochimica Acta, 55 (2010) 4057-4061.

[19] Y.F. Cui, S.H. Zuo, J.C. Jiang, S.Z. Yuan, J.H. Chu, Solar Energy Materials and Solar Cells, 95 (2011) 2136-2140.

[20] D. Lincot, H.G. Meier, J. Kessler, J. Vedel, B. Dimmler, H.W. Schock, Solar Energy Materials, 20 (1990) 67-79.

[21] J.J. Scragg, P.J. Dale, L.M. Peter, Electrochemistry Communications, 10 (2008) 639-642.

[22] Y. Ogawa, A. JagerWaldau, T.H. Hua, Y. Hashimoto, K. Ito, Applied Surface Science, 92

(1996) 232-236.

[23] M. Bar, B.A. Schubert, B. Marsen, S. Krause, S. Pookpanratana, T. Unold, L. Weinhardt, C. Heske, H.W. Schock, Applied Physics Letters, 99 (2011) 152111.

[24] T. Tanaka, T. Sueishi, K. Saito, Q.X. Guo, M. Nishio, K.M. Yu, W. Walukiewicz, Journal of Applied Physics, 111 (2012) 053522.

[25] O. Roussel, O. Ramdani, E. Chassaing, P.P. Grand, M. Lamirand, A. Etcheberry, O. Kerrec, J.F. Guillemoles, D. Lincot, J Electrochem Soc, 155 (2008) D141-D147.

[26] E. Chassaing, O. Ramdani, P.-P. Grand, J.-F. Guillemoles, D. Lincot, physica status solidi (c), 5 (2008) 3445-3448.

[27] A.J. Bard, R. Parsons, J. Jordan, Standard potentials in aqueous solution, CRC, 1985.

[28] V. Izquierdo-Roca, E. Saucedo, C.M. Ruiz, X. Fontane, L. Calvo-Barrio, J. Alvarez-Garcia, P.P. Grand, J.S. Jaime-Ferrer, A. Perez-Rodriguez, J.R. Morante, V. Bermudez, Phys Status Solidi A, 206 (2009) 1001-1004.

[29] V. Izquierdo-Roca, J. Alvarez-Garcia, L. Calvo-Barrio, A. Perez-Rodriguez, J.R. Morante, V. Bermudez, O. Ramdani, P.P. Grand, O. Kerrec, Surface and Interface Analysis, 40 (2008) 798-801.

[30] L. Thouin, J. Vedel, J Electrochem Soc, 142 (1995) 2996-3001.

[31] D.B. Mitzi, O. Gunawan, T.K. Todorov, K. Wang, S. Guha, Solar Energy Materials and Solar Cells, 95 (2011) 1421-1436.

[32] A. Redinger, K. Hones, X. Fontane, V. Izquierdo-Roca, E. Saucedo, N. Valle, A. Perez-Rodriguez, S. Siebentritt, Applied Physics Letters, 98 (2011) 101907.

[33] N.D. Boscher, C.J. Carmalt, R.G. Palgrave, I.P. Parkin, Thin Solid Films, 516 (2008) 4750-4757.

[34] L. Thouin, S. Rouquettesanchez, J. Vedel, Electrochimica Acta, 38 (1993) 2387-2394.

[35] M.E. Calixto, K.D. Dobson, B.E. McCandless, R.W. Birkmire, J Electrochem Soc, 153 (2006) G521-G528.

[36] F.A. Kroger, J Electrochem Soc, 125 (1978) 2028-2034.

[37] R. Kowalik, P. Zabinski, K. Fitzner, Electrochimica Acta, 53 (2008) 6184-6190.

[38] M.P.R. Panicker, M. Knaster, F.A. Kroger, J Electrochem Soc, 125 (1978) 566-572.

[39] D. Lincot, A. Kampmann, B. Mokili, J. Vedel, R. Cortes, M. Froment, Applied Physics Letters, 67 (1995) 2355-2357.

[40] I. Barin, Si-$SrWO_4$, in: Thermochemical Data of Pure Substances, Wiley-VCH Verlag GmbH, 2008, pp. 1480-1586.

[41] I. Barin, WS_{2-e}, in: Thermochemical Data of Pure Substances, Wiley-VCH Verlag GmbH, 2008, pp. 1815-1885.

[42] N.R. Mathews, Solar Energy, 86 (2012) 1010-1016.

[43] J.F. Guillemoles, P. Cowache, A. Lusson, K. Fezzaa, F. Boisivon, J. Vedel, D. Lincot, Journal of Applied Physics, 79 (1996) 7293-7302.

[44] P.A. Fernandes, P.M.P. Salome, A.F. da Cunha, Thin Solid Films, 517 (2009) 2519-2523.

[45] M. Grossberg, J. Krustok, J. Raudoja, K. Timmo, M. Altosaar, T. Raadik, Thin Solid Films, 519 (2011) 7403-7406.

[46] J. He, L. Sun, S.Y. Chen, Y. Chen, P.X. Yang, J.H. Chu, Journal of Alloys and Compounds, 511 (2012) 129-132.

[47] V. Izquierdo-Roca, X. Fontané, E. Saucedo, J.S. Jaime-Ferrer, J. Álvarez-García, A. Pérez-Rodríguez, V. Bermudez, J.R. Morante, New Journal of Chemistry, 35 (2011) 453.

[48] L.M. Peter, Chem Rev, 90 (1990) 753-769.

[49] H.C. Ye, H.S. Park, V.A. Akhavan, B.W. Goodfellow, M.G. Panthani, B.A. Korgel, A.J. Bard, J Phys Chem C, 115 (2011) 234-240.

2.2. Fabrication of $Cu_2ZnSnSe_4$ Thin Films from an Electrodeposited Cu-Zn-Sn-Se/Cu-Sn-Se Bilayer

2.2.1. Introduction

Previously, we have developed an alternative electrochemical approach to fabricate CZTSSe thin film, *i.e.*, single-step electrodeposition of a Cu-Zn-Sn-Se precursor film from an electrolyte containing Cu(II), Zn(II), Sn(IV), and Se(IV) species followed by sulfurization[1]. Although we found appropriate electrodeposition conditions to obtain CZTSSe thin films, significant compositional deviations from the CZTSSe stoichiometry could not be avoided, resulted in difficulty to obtain photovoltaic properties of these thin films. In order to achieve efficient tuning of compositions to obtain the CZTSe film with the favorable Cu-poor/Zn-rich composition for photovoltaic application[2], herein we propose a sequential electrodeposition of Cu-Zn-Sn-Se and Cu-Sn-Se layers followed by annealing under argon (Ar) or Se atmosphere. Structural and compositional characterizations of as-deposited and annealed films are discussed. The solar cell properties of devices fabricated from these annealed films were also reported.

2.2.2. Experimental

Electrodeposition was carried out potentiostatically using in a Hokuto Denko HSV-110 potentiostat-galvanostat. A standard vertical three-electrode setup consisting of an Ag/AgCl reference electrode, a Pt-sheet counter electrode, and a Mo-coated glass substrate (Mo/glass) as a working electrode was employed for electrodeposition. The electrolyte used for the first Cu-Zn-Sn-Se layer consisted of 2.5 mM $CuSO_4$, 80 mM $ZnSO_4$, 20 mM $SnCl_4$, 5 mM Na_2SeO_3 and 500 mM lactic acid with the pH carefully adjusted to 2.5-2.6 by addition of aqueous NH_3 solution (28%). The electrolyte for the second Cu-Sn-Se layer was consisted of 1 mM $CuSO_4$, 20 mM $SnCl_4$, 7 mM Na_2SeO_3 and 500 mM lactic acid with the pH adjusted to 2.5-2.6 by the addition of aqueous NH_3 solution (28%). Electrodepositions for the first and the second layers were performed at potential of -0.6 V (*vs.* Ag/AgCl) for 30 min and 20 min, respectively. During these depositions, temperature of electrolytes was kept at 24 °C using a thermostatted water bath.

The as-deposited film was then annealed at 475 °C or 525 °C under Ar flow (200 ml min^{-1}) for 5 min. The annealing was also performed in the presence Se vapor. For this experiment, a two-zone furnace was employed: 1 g of Se powder was heated to 350 °C in the first zone to form a Se vapor and the as-deposited film was heated at 575 °C in the second zone for 5 min. Nitrogen (N_2) gas with flow rate of 200 ml min^{-1} was used to carry the Se vapor from the first zone to the second zone.

For evaluation of solar cell properties of these annealed films, they were processed to form an glass/Mo/CZTSe/CdS/ZnO/Al:ZnO structure. After cleaning the surfaces of the annealed films by immersion in an aqueous KCN solution (10%) for 2 min, a CdS buffer layer was deposited by chemical bath deposition [3]. Then an ZnO and an Al:ZnO layers were sequentially deposited on the top of the CdS layer by radio frequency (RF) magnetron sputtering.

Elemental compositions of thus-obtained films were determined using a Hitachi TM3000 scanning electron microscope (SEM) equipped with a SwiftED3000 energy dispersive X-ray spectrometer (EDX). Crystal structures were measured by X-ray diffraction (XRD) analysis using a Rigaku MiniFlex X-ray diffractometer (Cu Kα, Ni filter). Crystalline phase compositions were determined by Raman spectroscopy using a JASCO NRS-3100 Laser Raman Spectrophotometer with a laser wavelength of 532 nm. Surface and cross-sectional morphologies of the films after sulfurization were examined using a Hitachi S-5000 FEG field emission scanning electron microscope (FE-SEM). Current density-voltage (*J*-*V*) characteristics under simulated AM1.5 irradiation (100 mW cm^{-2}) through the Al:ZnO window layer and those under dark of thus-obtained solar cells were measured with a Bunkoh-Keiki CEP-015 photovoltaic measurement system.

2.2.3 Result and discussion

2.2.3.1. Structural characterizations

Fig. 1a shows Raman spectrum of the first Cu-Zn-Sn-Se layer electrodeposited from the solution containing Cu(II), Zn(II), Sn(IV), and Se(IV) species. The appearance of a dominant peak at 190 cm^{-1} is close to the A1 mode peak of CZTSe[2,4]. However, presences of other secondary phases were also expected by observation of a broad peak at *ca.* 230-270 cm^{-1}: this is likely to be an overlapping of peaks due to a trigonal selenium (240 cm^{-1})[5], ZnSe (250 cm^{-1})[14], and Cu_xSe (263 cm^{-1})[6]. The EDX analysis of the Cu-Zn-Sn-Se layer revealed that the atomic ratio of the layer was Cu-poor (Cu/(Zn+Sn) = 0.76), Zn-rich (Zn/Sn = 6.04), and Se-poor (Se/metals = 0.78) compositions when compared to the ideal CZTSe stoichiometry. In order to compensate insufficient Cu, Sn, and Se components, the second layer was electrodeposited on the top of the underlying layer from the electrolyte containing Cu(II), Sn(IV), and Se(IV) species. The Raman spectrum of the film after the deposition of the second layer indicated a shift of the main peak to 180 cm^{-1}, as shown in Fig. 1b. Since the A1 mode peaks of Cu_2SnSe_3 and $SnSe_2$ are close to this value[7][8], we cannot exclude the possibility of the second layer was mixture of these compounds.

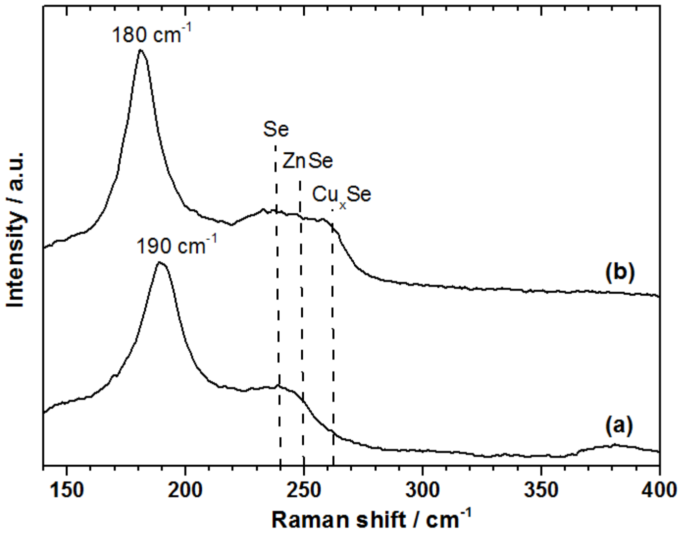

Figure 1. Raman spectrum of (a) the Cu-Zn-Sn-Se bottom layer and (b) the Cu-Zn-Sn-Se/Cu-Sn-Se bilayer.

Fig. 2 shows cross-sectional and top-view SEM images of the as-deposited bilayer. The cross-sectional image clearly exhibits a boundary between the bottom Cu-Zn-Sn-Se layer and the top Cu-Sn-Se layer with thicknesses of 1.3 μm and 1.4 μm, respectively (Fig. 2a). Corresponding surface image indicated homogeneous deposition of the top Cu-Sn-Se layer, though it had rough surfaces consisted of granular particles (Fig. 2b).

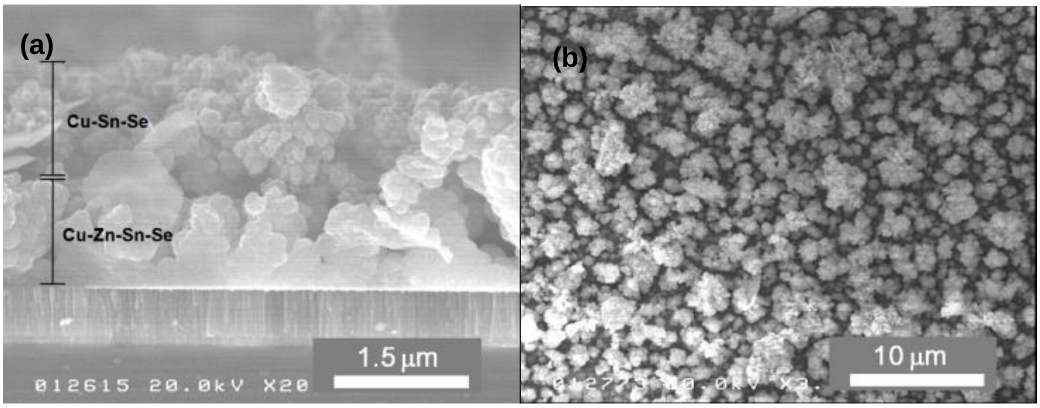

Figure 2. (a) Cross-sectional and (b) surface SEM images of the as-deposited film.

As shown in Fig. 3a, XRD pattern of the as-deposited bilayer film has broad peaks at 2θ of 27° and 45° assignable to reflections of both CZTSe (JCPDS 52-0868) and CTSe (JCPDS 72-8034), in addition to reflections of the Mo substrate. Upon annealing of this film at 475 °C under Ar flow, intensities of the peaks increased and an additional peak also appeared at 2θ of 53° (Fig. 3b). These peaks became more intense with increase in the annealing temperature at 525 °C (Fig. 3c), indicating an increase in the film crystallinity. Corresponding Raman spectra of these Ar–annealed films shown in Figs. 4a and 4b indicate appearances of three peaks at 196 cm^{-1}, 172 cm^{-1}, and 234 cm^{-1}. Since they are well consistent with peaks of CZTSe[2,4], we can expect formation of pure CZTSe phase in these Ar-annealed films: thus, observed three peaks in XRD patterns of these Ar-annealed films are assignable to (112), (220), and (312) reflections of CZTSe crystallites. As shown in Fig. 5a, the cross-sectional SEM image of the Ar-annealed film at 525 °C showed an appreciable grain growth compared to the as-deposited bilayer film, *i.e.*, micrometer-sized grains were formed on the entire surface of the Mo layer. As observed in the top-view SEM image shown in Fig. 5b, however, their distribution was quite loose.

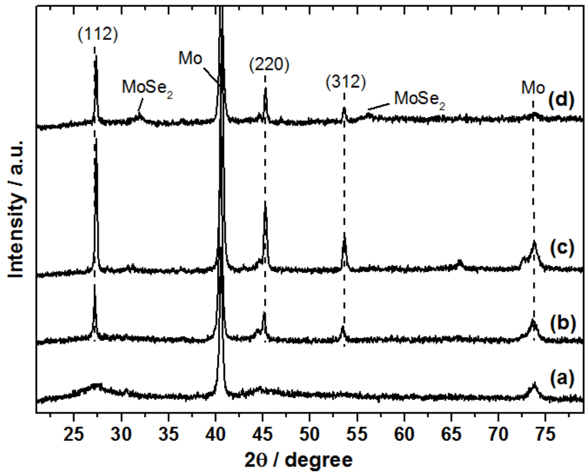

Figure 3. XRD patterns of (a) the as-deposited film, and those that annealed under Ar at (b) 475 °C and (b) 525 °C, and (d) selenized at 575 °C.

Atomic compositions and ratios of the Ar-annealed films obtained by EDX analyses are summarized in Table 1 (entries 1 and 2). Both of the Ar-annealed films had rather Cu-poor compositions from the ideal stoichiometry of CZTSe. Although this is desirable for photovoltaic application, atomic percentages of Sn and Se of the films were very small, leading to highly Zn-rich and slightly Se-poor compositions: such compositional deviation became significant upon increase in annealing temperature. Indeed, when we performed further increase in temperatures of Ar-annealing, losses of Sn and Se became more severe (data not shown). As reported in the literature [9], these losses were likely to be due to the evaporation of SnSe during the annealing because of a high-vapor pressure of this material.

Table 1. Atomic compositions and ratios of the film annealed at various temperatures under Ar and under Se flows for 5 min.

Temp. (Atmosphere)	Cu (%at.)	Zn (%at.)	Sn (%at.)	Se (%at.)	Cu/(Zn+Sn)	Zn/Sn	Se/metals
475 ^{o}C (Ar)	24.40	16.22	11.66	47.72	0.88	1.40	0.91
525 ^{o}C (Ar)	23.65	19.64	10.01	46.7	0.80	1.97	0.88
575 ^{o}C (Se)	23.44	15.67	12.82	48.07	0.82	1.23	0.93

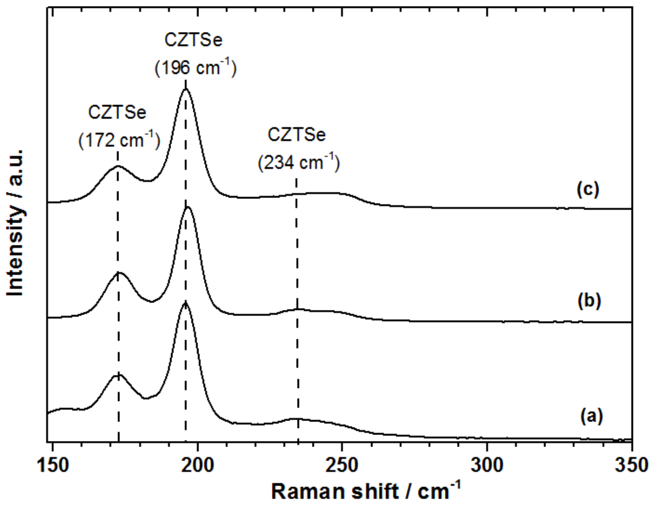

Figure 4. Raman spectra of annealed films under Ar at (a) 475 °C and (b) 525 °C, and (c) under Se flow at 575 °C.

In order to avoid Sn and Se losses as much as possible, we performed annealing under Se flow. As shown in Table 1 (entry 3), the atomic composition of thus-obtained film indicates suppression of Sn and Se evaporations even when we applied a high temperature annealing (575 °C). Corresponding Raman spectrum shown in Fig. 4c indicates formation of the CZTSe phase as a single phase, while appreciable formation of the $MoSe_2$ was also observed in its XRD pattern (Fig. 3d). In addition, the Se-annealing induced morphological differences of the film when compared to that obtained by the Ar-annealing. As shown in SEM images of the Se-annealed film (Figs. 5c and 5d), the film had relatively dense morphology, though it composed of rather small grains despite of applying the high temperature annealing. It is also noted that the thickness of the bottom Mo layer of the Se-annealed film increased from *ca.* 600 nm to *ca.* 800 nm due to the formation of a thick $MoSe_2$ layer.

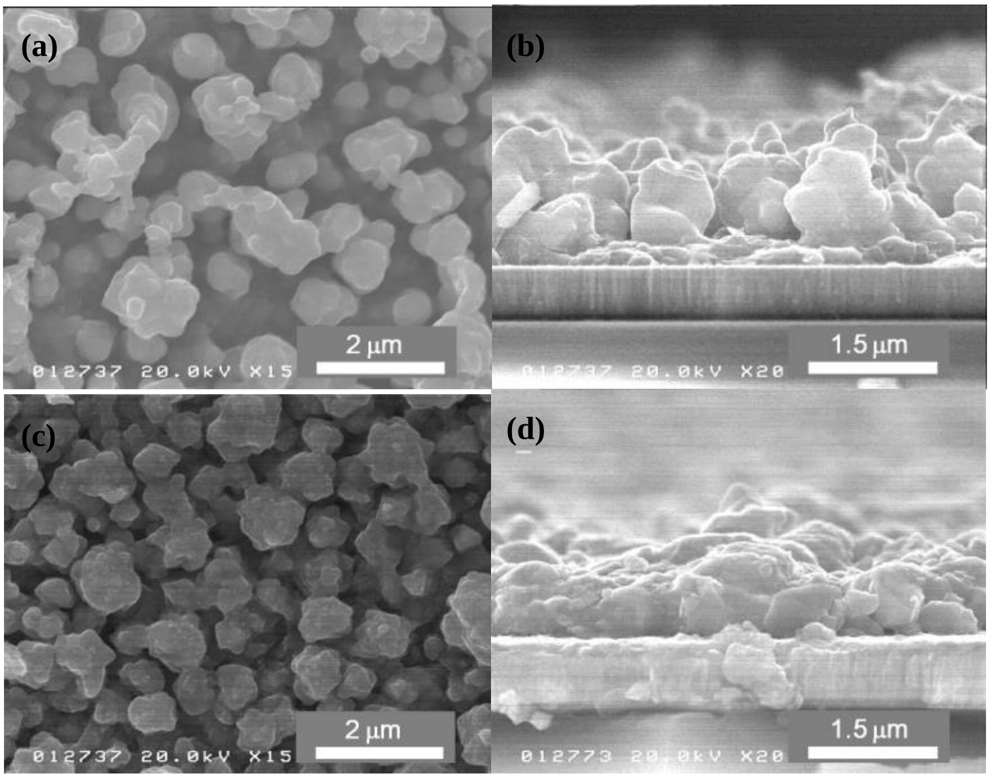

Figure 5. (a, c) Cross-sectional and (b, d) surface SEM images of the film (a, b) annealed at 525 °C under Ar, and (c, d) under Se flow at 575 °C.

2.2.3.2 Solar cell properties

To evaluate solar cell properties, these annealed films were transferred into devices with a glass/Mo/CZTSe/CdS/ZnO/Al:ZnO structure. Fig. 6 shows the *J*-*V* characteristics of them. As shown in Figs. 6a and 6b, the devices derived from Ar-annealed films gave appreciable photovoltage: specifically, the device based on the 525 °C-annealed film exhibits relatively high open circuit potential (V_{OC}). However, they showed quite low short circuit current densities (J_{SC}s), indicating that they have high series resistances (R_s), despite the formation of relatively large grains. As discussed above, these Ar-annealed films have atomic compositions significantly deviated from the CZTSe stoichiometry. This might induce a reduction of the carrier transport property of the CZTSe bulk. On the other hand, the solar cell derived from the

Se–annealed film showed appreciable J_{SC}: it showed conversion efficiency of 1.1% (Fig. 6c). Reduction of the deviation of atomic compositions of Sn and Se in the Se–annealed CZTSe film from the ideal composition for solar cell application (see above) should result in an improvement of carrier transport property. Nevertheless, the efficiency of the best device in the present study was still low compared to the reported CZTSe-based device ($\eta = 9.1\%$) [10]. It is clear from the *J*-*V* curve of the present best device that it has a significant leakage and appreciable resistances. Indeed, estimated shunt resistance (R_{sh}) was very low (0.028 kΩ cm^2) and its R_s value is somewhat large (8 Ω cm^2). The former leakage is likely to be due to presences of crevices between less-grown CZTSe grains and the latter resistance is partly attributed to the presence of thick $MoSe_2$ layer. Relatively Se-poor composition of the film, which would create a deep donor level [11], and rough surface morphology of the CZTSe film should enhance carrier recombination at the CZTSe bulk and the CZTSe-CdS interface, respectively. These structural and morphological faults led to reducing overall cell parameters of the present device significantly. Thus, in order to improve them, changes in parameters for depositions of the Cu-Zn-Sn-Se/Cu-Sn-Se bilayer and optimization of annealing conditions, *e.g.*, duration, profile, and selenium vapor pressure, are now in progress.

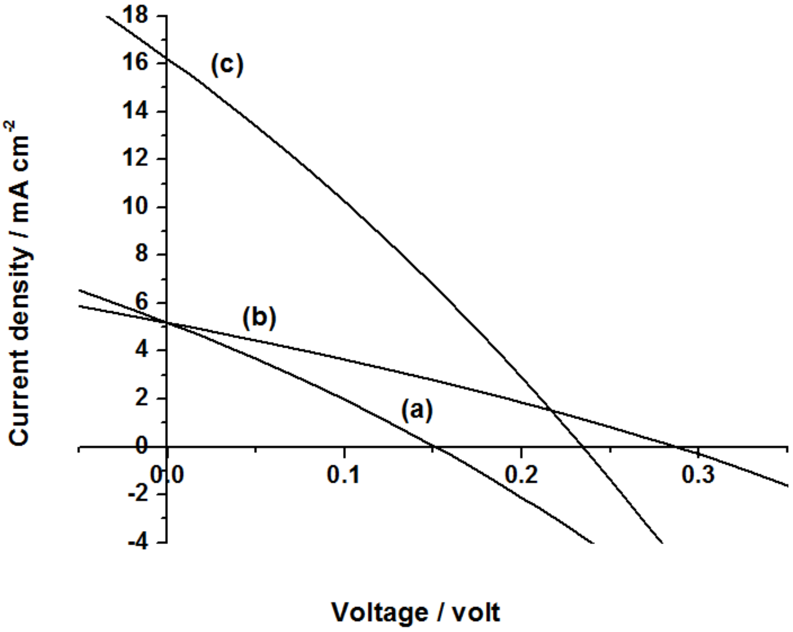

Figure 6. Illuminated *J-V* curves of glass/Mo/CZTSe/CdS/ZnO/AZO devices using the film annealed under Ar at (a) 475 °C and (b) 525 °C, and (c) under Se flow at 575 °C.

2.2.4 Conclusion

In this study, we reported a fabrication of CZTSe solar cell from the electrodeposited Cu-Zn-Sn-Se/Cu-Sn-Se bilayer. Although the annealing under Ar induced significant losses of Sn and Se components, these losses could be reduced by the introduction of Se vapor during annealing. Solar cells based on the thus-obtained CZTSe thin film showed appreciable device properties: the highest conversion efficiency of 1.1% was obtained on the cell based on the CZTSe thin film prepared by annealing under Se flow. Thus, we have proved the possibility of present new electrochemical route for fabrication of the CZTSe-based photovoltaic device. The conversion efficiency is expected to be improved by further optimizations of synthetic parameters of the CZTSe film.

References

[1] W. Septina, S. Ikeda, A. Kyoraiseki, T. Harada, M. Matsumura, Electrochim. Acta **88**, 436-442 (2013).

[2] D.B. Mitzi, O. Gunawan, T.K. Todorov, K. Wang, S. Guha, Sol. Energy Mater. Sol. Cells **95**, 1421-1436 (2011).

[3] S. M. Lee, S. Ikeda, T. Yagi, T. Harada, A. Ennaoui and M. Matsumura, Phys. Chem. Chem. Phys **13**, 6662 (2011).

[4] A. Redinger, K. Hones, X. Fontane, V. Izquierdo-Roca, E. Saucedo, N. Valle, A. Perez-Rodriguez, S. Siebentritt, Appl. Phys. Lett. 98, 101907 (2011).

[5] V. Izquierdo-Roca, J. Alvarez-Garcia, L. Calvo-Barrio, A. Perez-Rodriguez, J.R. Morante, V. Bermudez, O. Ramdani, P.P. Grand, O. Kerrec, Surf. and Interface Anal. **40**, 798-801 (2008).

[6] V. Izquierdo-Roca, E. Saucedo, C.M. Ruiz, X. Fontane, L. Calvo-Barrio, J. Alvarez-Garcia, P.P. Grand, J.S. Jaime-Ferrer, A. Perez-Rodriguez, J.R. Morante, V. Bermudez, Phys. Status Solidi A **206**, 1001-1004 (2009).

[7] P.U. Bhaskar, G.S. Babu, Y.B.K. Kumar, V.S. Raja, Appl. Surf. Sci. **257**, 8529-8534 (2011).

[8] D.G. Mead and J.C. Irwin, Solid State Commun. **20**, 885-887 (1976).

[9] J.J. Scragg, P.J. Dale, D. Colombara, L.M. Peter, ChemPhysChem **13**, 3035-3046 (2012).

[10] I. Repins, C. Beall, N. Vora, C. DeHart, D. Kuciauskas, P. Dippo, B. To, J. Mann, W.-C. Hsu, A. Goodrich, R. Noufi, Sol. Energy Mater. Sol. Cells **101**, 154-159 (2012).

[11] T. Maeda, S. Nakamura, T. Wada, Thin Solid Films **519**, 7513-7516 (2011).

Chapter 3

Electrochemical Deposition of Metallic Films for Fabrication of Cu_2ZnSnS_4 and $CuSbS_2$-based Solar Cells

3.1. Fabrication of Cu_2ZnSnS_4 Thin Films from Electrodeposited Metallic Stack and Its Photovoltaic Applications: Mechanistic Study of Preheating Effect to The Electrodeposited Metals Precursor

3.1.1. Introduction

Copper zinc tin sulfide (Cu_2ZnSnS_4, CZTS) is one of the most promising materials as an alternative low-cost absorber for thin-film photovoltaic devices. The material has a high optical absorption coefficient of 10^4 cm^{-1} and a direct band gap of 1.5 eV [1-3]: the theoretical limit of power conversion efficiency is as high as 32% based on Shockley-Queisser photon balance calculations [4]. Moreover, compared to other commercial CdTe and CIGS absorbers, it is advantageous that all of the constituent elements in CZTS are naturally abundant and non-toxic, thus facilitating large-scale production [5,6].

A literature survey indicated that CZTS-based solar cells have been primarily fabricated by vacuum technologies, *e.g.*, CZTS devices with high conversion efficiencies of 8.4% and 6.7% have been prepared by evaporation[7] and sputtering [8], respectively. However, these vacuum processes suffer from relatively low throughput, low material utilization, and difficulties associated with large-scale production [9]. To overcome these drawbacks, many researchers have adopted solution-based non-vacuum deposition approaches, such as spray pyrolysis [10], printing [11,12], spin coating [13,14], and electrodeposition [15-17] because of their suitability for use in large-scale substrates, high throughput, and efficient material usage. Recently, a selenosulfide derivative, $Cu_2ZnSn(S,Se)_4$ (CZTSSe), fabricated by spin coating of a hydrazine-based precursor solution containing required elements has reached more than 11% efficiency [14], though the CZTSSe material contains toxic selenium and the use of explosive hydrazine is necessary for its synthesis.

Among the above-mentioned non-vacuum methods, electrodeposition of a CZTS film has been shown to be desirable because of its advantages, including low equipment cost, negligible waste of chemicals with utilization efficiencies close to 100%, and possible formation of a compact film required for solar cell application. In the pioneering work by Ennaoui *et al.*, a

CZTS-based solar cell prepared from an elecrodepositied Cu-Sn-Zn alloy followed by sulfurization at 550 °C for 2 h showed appreciable photovoltaic properties with a conversion efficiency of 3.4 % [15]. Scragg *et al.* also reported 3.2% conversion efficiency using a CZTS-based solar cell prepared by electrodeposition of a Cu/Sn/Cu/Zn metallic stack followed by sulfurization at 575 °C for 2 h [16]. One of the main drawbacks of these methods reported in the literature is the requirement of long sulfurization duration, which is unsuitable for an industrial process in terms of both time and energy usage.

Recently, Ahmed *et al.* have shown a significant effect of preheating of an electrodeposited metallic stack before sulfurization on photovoltaic properties: a CZTS-based solar cell exhibiting more than 7% conversion efficiency was obtained by sulfurization of the precursor in a short period (12 min) [17]. Although the primary factor of the preheating effect has not yet been revealed in a preliminary study, these results motivated us to find optimum conditions of such preheating for achieving better photovoltaic performance as well as to examine mechanistic aspects of the preheating effects. In our work, therefore, the structural and morphological variations of an electrodeposited Cu-Sn-Zn stack induced by preheating and the growth mechanisms of CZTS films from these metallic precursors with and without preheating were examined in detail. Based on the results, their effects on photovoltaic properties of the thus-obtained CZTS-based cell are also discussed.

3.1.2. Experimental

Metallic layers of copper (Cu), tin (Sn), and zinc (Zn) were deposited successively on a molybdenum-coated soda lime glass (Mo/glass) substrate by using a conventional three-electrode cell with a Pt foil as a counter electrode and an Ag/AgCl reference electrode under potentiostatic control using a Hokuto Denko HSV-110 potentiostat. A Cu layer was firstly deposited on Mo/glass at -0.4 V (*vs.* Ag/AgCl) in an aqueous solution containing 0.05 M $CuSO_4$, 0.02 M citric acid and 0.04 M tri-sodium citrate. An Sn layer was deposited on the Cu-covered Mo/glass substrate at -0.55 V (*vs.* Ag/AgCl) in an aqueous solution with 0.05 M $Sn(SO_3CH_3)_2$

and 1 M CH_3SO_3H. Finally, a Zn layer was deposited at -1.20 V (*vs.* Ag/AgCl) in a pH 3 buffer solution containing $ZnSO_4$ (0.1 M) and K_2SO_4 (0.5 M). During depositions of these metallic layers, deposition baths were kept at 25 °C by a thermostatted water bath. Thus-obtained metallic stack, labeled CTZ(0), was placed in an evacuated Pyrex ampule (*ca.* 160 cm^3). The ampule was then put in a 350-˚C heated electric furnace; after keeping it for 20 min or 40 min, the ampule was ejected from the furnace for cooling. Samples after the 350-˚C preheating for 20 min and 40 min were labeled CTZ(20) and CTZ(40), respectively. In order to facilitate sulfurization to form CZTS films, these metallic precursors with or without the 350-˚C preheating (*i.e.*, CTZ(0), CTZ(20), and CTZ(40)) were again put in the evacuated Pyrex ampule with 5 mg elemental sulfur. The ampule was then put in a 580-˚C heated electric furnace; after keeping it for 10 min, the ampule was ejected from the furnace for cooling. The CZT(0) sample was also sulfurized at 585 °C for 12 min for comparison.

Crystal structures of the films were analyzed by X-ray diffraction (XRD) using a Rigaku MiniFlex X-ray diffractometer (Cu Kα, Ni filter). Crystalline phase compositions were determined by Raman spectroscopy using a JASCO NRS-3100 Laser Raman Spectrophotometer with a laser wavelength of 532 nm. Morphology of the films was studied using a Hitachi S-5000 FEG field emission scanning electron microscope (FE-SEM) at a voltage of 20 kV. Atomic compositions were analyzed by energy-diffuse X-ray (EDX) analysis using a Hitachi S-2250N EDX analyzer.

As-prepared CZTS films were processed to complete with an glass/Mo/CZTS/CdS/Al:ZnO structure [18,19]. The CdS buffer layer was deposited by chemical bath deposition (CBD). Then a transparent conductive oxide (TCO) layer of Al-doped ZnO (Al:ZnO) was deposited on the CdS surface by radio-frequency (RF)-magnetron sputtering. Current density-voltage (*J*-*V*) characteristics under simulated AM1.5 irradiation (100 mW cm^{-2}) were measured with a Bunkoh-Keiki CEP-015 photovoltaic measurement system.

3.1.3. Results and discussion

Fig. 1 shows XRD patterns of the electrodeposited metallic precursor film (CTZ(0)) and the films heated at 350 °C in an evacuated ampule for 20 min (CTZ(20)) and 40 min (CTZ(40)). As-expected, the XRD pattern of CTZ(0) can be indexed to be a mixture of Cu (JCPDS 04-0836), Zn (JCPDS 65-3358), and Sn (JCPDS 65-2631) (Fig. 1a). On the other hand, the CTZ(20) sample showed XRD patterns of Cu-Sn and Cu-Zn alloys with chemical compositions of Cu_6Sn_5 (JCPDS 65-2303), Cu_5Zn_8 (JCPDS 41-1435) and Cu_3Sn (JCPDS 65-4653) and reflections of pure metals disappeared, as shown in Fig. 1b. The fact that the color of the film changed from the white-grey of the Zn top layer of the precursor into a grey-gold is attributable to formation of such alloys. Due to the limited mutual solubility between Sn and Zn (*i.e.*, less than 0.5 wt %) [20], there is no observation of any Sn-Zn alloys. Indeed, no experimental evidence for any stable solid phases between Sn and Zn has been reported [21]. In addition, prolonged heat treatment for 40 min induced increase in intensities of reflections of Cu_6Sn_5 and Cu_5Zn_8, indicating crystalline growth of these alloys (Fig. 1c).

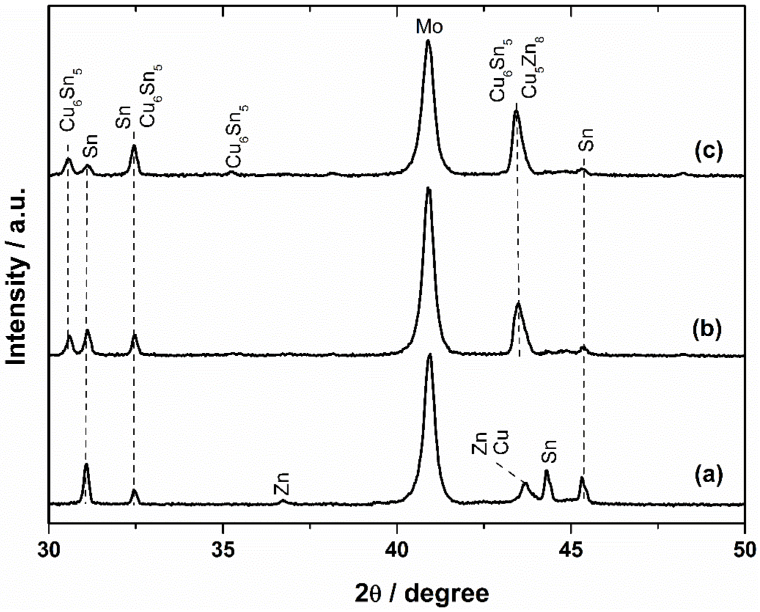

Figure. 1. X-ray diffraction patterns of (a) CTZ(0), (b) CTZ(20), and (c) CTZ(40).

Corresponding surface SEM images of metallic precursors are shown in Fig. 2. The SEM image of the CTZ(0) film shows island-shaped morphology: there are many crevices between their grains (Fig. 2a). Based on the fact that the Cu bottom layer formed a compact morphology (data), the observed island-shaped surface is derived from inhomogeneous electrodeposition of the second Sn layer. Although shapes of grains of CTZ(20) and CTZ(40) films became somewhat angular, island-shaped morphologies still remained (Figs. 2b and 2c). These results suggest requirements to find a condition for homogeneous deposition of Sn layer in order to obtain a homogeneous/flat metallic precursor layer. As can be expected from the above XRD results, moreover, sizes of angular grains in the CTZ(40) films was larger than those in the CTZ(20) films. It is also notable that there are appreciable voids formed in the CTZ(40) film: such a structural failure may affect properties of the final CZTS film (see below).

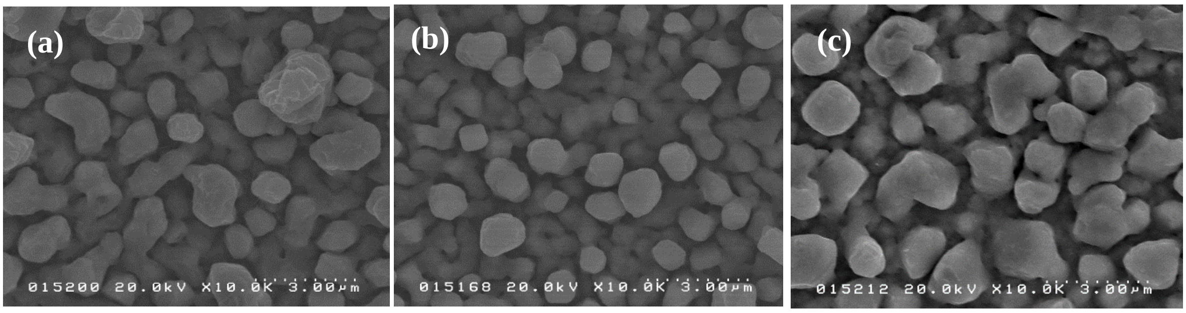

Figure 2. Top-view SEM images of (a) CTZ(0), (b) CTZ(20), and (c) CTZ(40).

Sulfurization of these metallic precursors in a sulfur atmosphere at 580 °C for 10 min led to complete alterations of diffraction patterns, as shown in Fig. 3. With or without preheating treatment, the XRD patterns of thus-obtained films matched well with the kesterite structure of CZTS (JCPDS 26-0575): reflections corresponding to (101), (110), (112), (103), (200), (202), (211), (105), (220), (312), (224) and (008) planes were detected without any significant reflections of other compounds except for those derived from the bottom Mo layer (*i.e.*, Mo and its sulfurized form). As shown in Fig. 4, corresponding Raman spectra showed an intense peak centered at 338 cm^{-1} along with two weak peaks located at 289 cm^{-1} and 369 cm^{-1}; these Raman signals are in good agreement with those derived from CZTS [8,22,23]. Other than these CZTS peaks, no appreciable peak was observed on sulfurized films prepared from the CTZ(20) and CTZ(40) metallic precursors, indicating high phase purity of these CZTS films (Figs. 4b and 4c). On the other hand, the presence of an additional peak centered at 303 cm^{-1}, which is assignable to the ternary phase of Cu_2SnS_3 [24,25], indicates insufficient phase purity of the CZTS film obtained from CTZ(0), as shown in Fig. 3a. Since the Cu_2SnS_3 compound shows almost the same diffraction patterns as those of CZTS, the presence of this secondary phase was not identified by the above XRD analysis. It should be noted that the Cu_2SnS_3 phase was disappeared when the CTZ(0) metallic precursor was sulfurized at higher temperature, *e.g.*, 585 °C for 12 min, indicating incomplete reaction of the CTZ(0) precursor when it sulfurized at 580 °C for 10 min (see below).

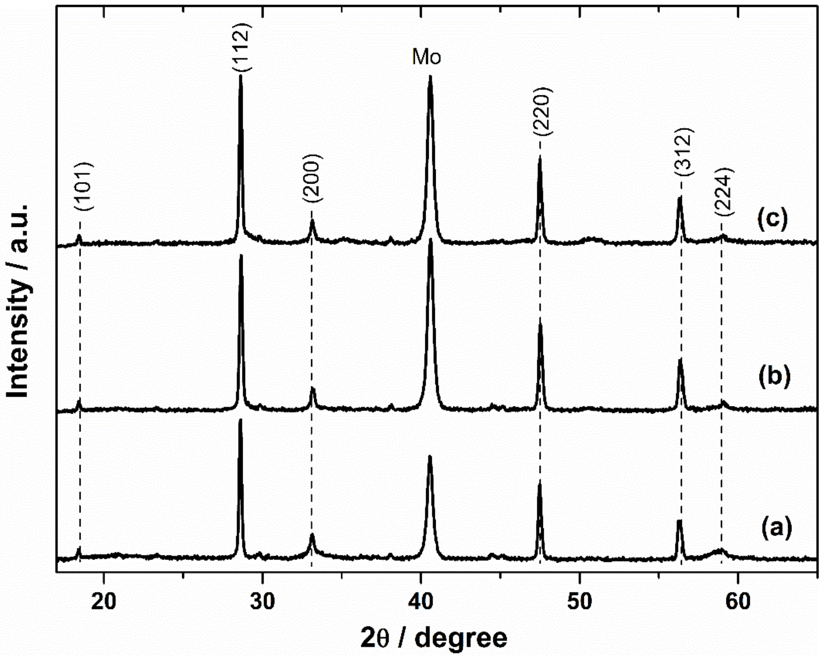

Figure 3. X-ray diffraction patterns of films sulfurized at 580 °C for 10 min that were obtained from (a) CTZ(0), (b) CTZ(20), and (c) CTZ(40).

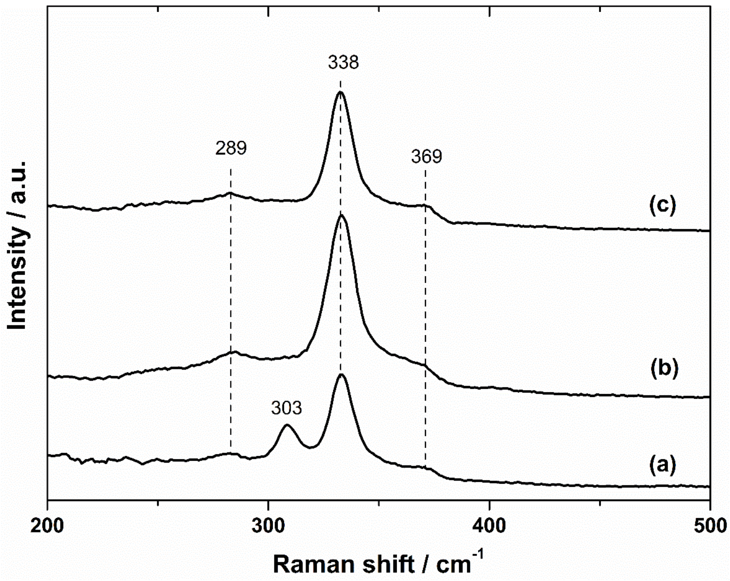

Figure 4. Raman spectra of films at sulfurized 580 ˚C for 10 min that were obtained from (a) CTZ(0), (b) CTZ(20), and (c) CTZ(40).

As determined by EDX analyses, chemical compositions of these sulfurized films were almost the same, with or without the 350-°C preheating. When compared to the stoichiometric composition (*i.e.*, Cu/Zn/Sn/S = 0.25/0.125/0.125/0.5), all of the films were Cu-poor (Cu content = *ca.* 0.23), leading to the formation of Cu vacancies that work as shallow acceptors [26,27]. With regard to Zn and Sn compostions, the CZTS films were Zn-rich relative to Sn (Zn/Sn = *ca.* 1.2) when compared to the stoichiometric ratio (Zn/Sn = 1). Since such Cu-poor and Zn-rich compositions have been shown empirically to have superior photovoltaic performance [26,28], this metallic composition of the films is approximately the composition, though the precise optimum condition has not yet been clarified. In addition, sulfur compositions of all of the films are close to the stoichiometric composition (S content = *ca.* 0.50), implying samller amounts of detrimental donor levels formed by S vacancies. It should be noted that there appear to be other compounds included in the CZTS film derived from CTZ(0) because of the presence of the Cu_2SnS_3 secondary phase despite having almost the same chemical composition as that of the single-phase CZTS films obtained from CTZ(20) and

CTZ(40). Based on the fact that no reflection or peak due to other such impurity phases was observed in the XRD pattern and Raman spectrum of the CZTS film, these contaminants are likely to be present as less-crystalline/amorphous forms in the film.

Fig. 5 shows surface and cross-sectional SEM images of CZTS films obtained from CTZ(0), CTZ(20), and CTZ(40). The surface SEM image of the CZTS film obtained by sulfurization of the CTZ(0) metallic precursor at 580 °C for 10 min indicates that the film consists of angular-shaped solids with particle sizes ranging from several hundreds of micrometers to a few micrometers, as shown in Fig. 5a. Micrometer-sized voids are also frequently observed between these solids. As expected from the surface morphology, the corresponding cross-sectional view shows the formation of many crevices in the CZTS film (Fig. 5d). Based on the fact that a part of the CZTS film thus-obtained was usually peeled-off, formation of these voids and crevices resulted in insufficient adhesion of the CZTS film to the Mo/glass substrate. Even though pure CZTS phase was obtained by sulfurization of the CTZ(0) precursor at 585 °C for 12 min, thus-obtained CZTS film had similar structural and morphological failures. On the other hand, there is no appreciably large void on the surface of the CZTS film obtained from the CTZ(20) metallic precursor: round-shaped particles were densely deposited to form a relatively smooth surface morphology, as shown in Fig. 5c. From its cross-sectional view, the CZTS film showed good adhesion to the Mo/glass substrate without any crevices (Fig. 5d). On the other hand, further extension of preheating to 40 min (*i.e.*, use of the CTZ(40) precursor) resulted in the formation of a CZTS film with less-packed morphology. It should be noted that angular- and round-shaped particles were mixed in the film. As shown in Fig. 5f, the morphological inhomogeneity was also observed in its cross-section, *i.e.*, there are two different particles: round-shape particles with relatively large sizes and angular-shaped particles with sizes of around a few hundred nanometers. In addition to the inhomogeneity, there are several voids, especially at the boundary between the CZTS film and the Mo layer. Hence, it would be an optimum duration of preheating to achieve a homogeneous and densely-packed CZTS film.

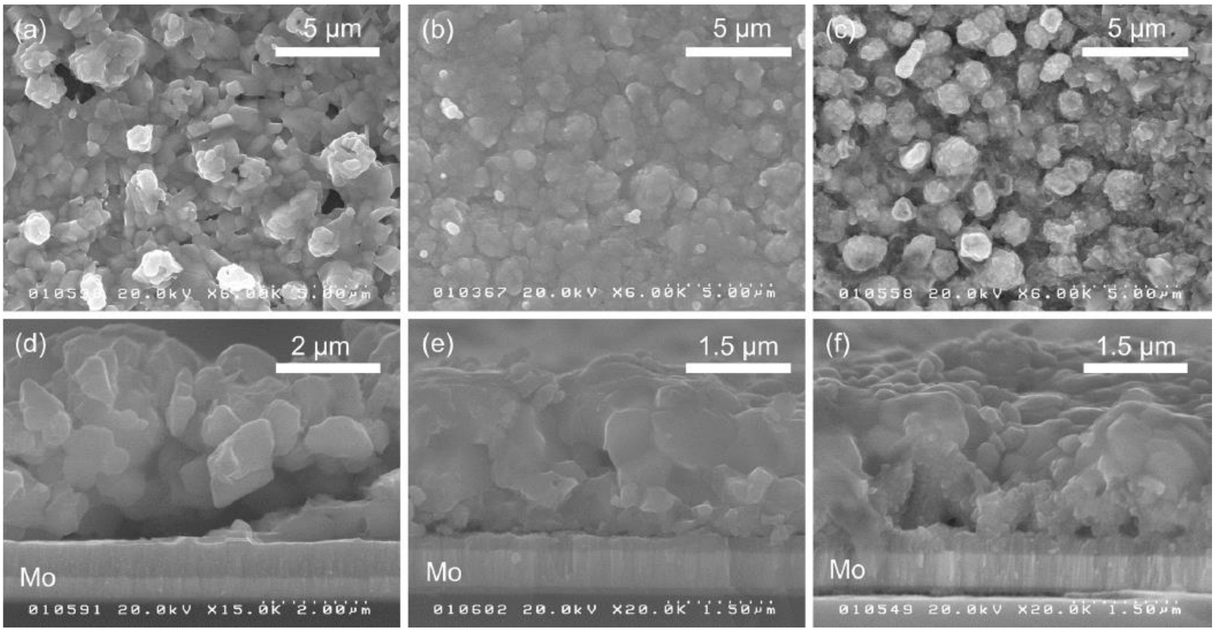

Figure 5. Top-view and cross-sectional SEM images of sulfurized CZTS films obtained from (a,d) CTZ(0), (b,e) CTZ(20), and (c,f) CTZ(40).

As shown in Figs. 5d-5f, cross-sectional SEM images clearly indicate darkening of the upper parts of the Mo layer due to the formation of molybdenum disulfide (MoS_2) during sulfurization. A thick MoS_2 layer (*ca.* 500 nm in thickness) was observed in the sample prepared from CTZ(0) (Fig. 5d). The thickness of the layer in the sample obtained from CTZ(40) was moderate (Fig. 5f), and the MoS_2 layer with the smallest thickness was formed in the sample derived from CTZ(20) (Fig. 5e). Since the thickness of the MoS_2 layer tended to increase with increase in amounts of voids and crevices formed in the CZTS layer, the reaction of the Mo layer and sulfur vapor should be enhanced by peeling-off of the upper metallic and/or CZTS layer during sulfurization. Formation of the MoS_2 interfacial layer at the CZTS/Mo interface is known to be critical in facilitating quasi-ohmic electrical contact[9] but not would be detrimental when it forms with an appreciable thickness. Thus, the CZTS film derived from CTZ(20), having the least-thick MoS_2 layer, is favorable for photovoltaic application.

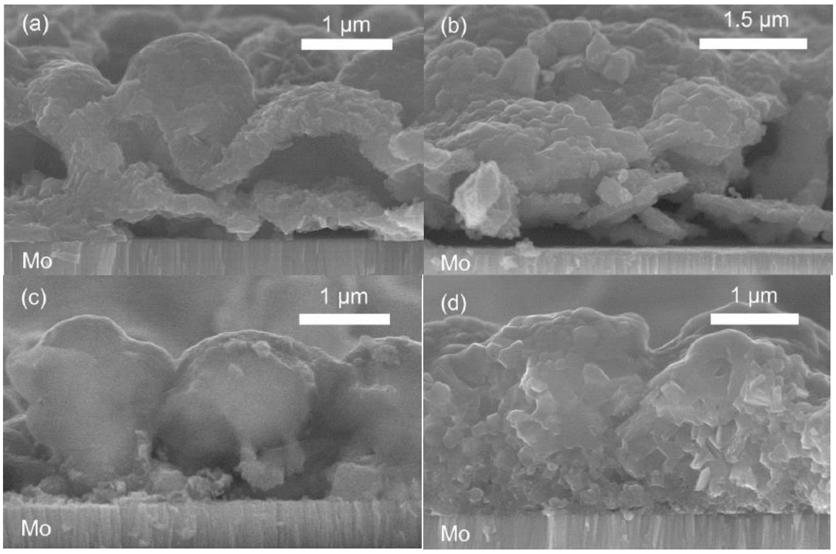

Figure 6. Cross-sectional SEM images of (a, b) CTZ(0) and (c, d) CTZ(20) films after sulfurization for (a, c) 1 min and (b, d) 2 min.

For further evaluation of effects of preheating on properties of thus-obtained CZTS films, morphologies and phase compositions of CTZ(0) and CTZ(20) films after sulfurization for short periods (1 and 2 min) were compared. Typical results on cross-sectional SEM images and Raman spectra of these films are shown in Figs. 6 and 7, respectively. The 1-min sulfurized film obtained from the CTZ(0) metallic precursor shows formation of a layered compound along with appreciable crevices, as can be seen in Fig. 6a. The corresponding Raman spectrum presented in Fig. 7a shows an intense peak centered at 473 cm^{-1}, assignable to copper sulfide (Cu_xS) [29,30], together with the 338 cm^{-1} peak derived from CZTS. Since the Cu_xS compound usually forms a plate-like shape, the observed layered morphology should reflect the formation of the compound. Although the 2-min sulfurized film obtained from CTZ(0) shows an increase in the peak intensity of CZTS, *i.e.*, facilitation of CZTS formation (Fig. 7b), the peak of Cu_xS still appeared, suggesting difficulty in complete diffusion of metallic components due to their inhomogeneous distributions. This should result in the formation of the ternary by-product (Cu_2SnS_3) after prolonged sulfurization (see Fig. 4a). Another point worth noting for the 2-min sulfurized film is that large crevices were still present in the film (Fig. 6d). This results in poor adhesion of the CZTS film to the Mo/glass substrate, as also shown in Fig. 5d. With regard to the 1-min sulfurized film obtained from the CTZ(20) metallic precursor, micrometer-sized lumps were formed without appearance of a layered structure, as shown in Fig. 6c. Although the corresponding Raman spectrum showed an appreciable peak of the Cu_xS compound (Fig. 7c), its peak intensity was significantly small compared to the 1-min sulfurized film obtained from CTZ(0). Moreover, complete disappearance of the Cu_xS compound to form a single-phase CZTS film was achieved after 2-min sulfurization, as shown in Fig. 7d. The cross-section indicates much better adhesion to the bottom Mo layer than that of the 2-min sulfurized film derived from CTZ(0) (see above), while the film was still composed of small particles of *ca.* 100 nm in size (Fig. 6d).

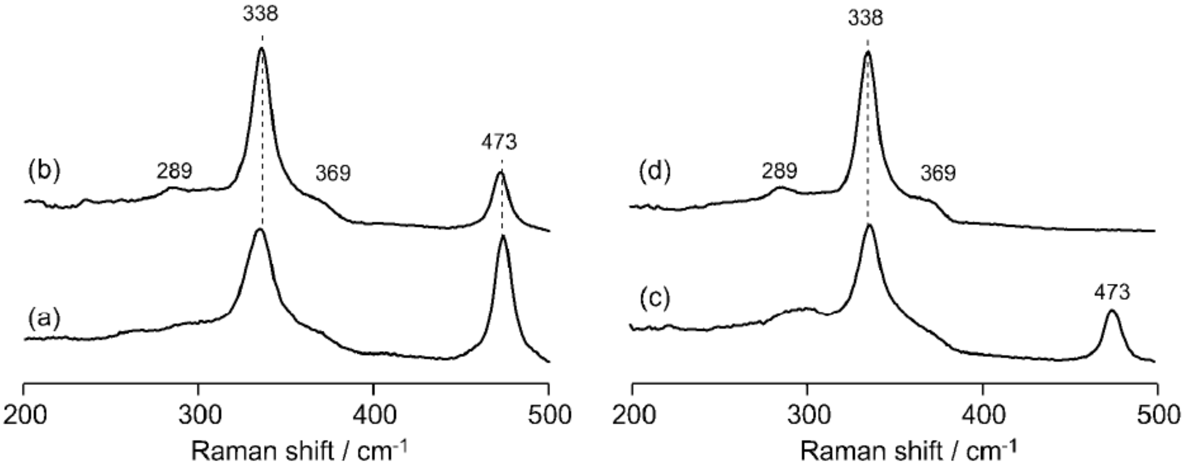

Figure 7. Raman spectra of (a,b) CTZ(0) and (c,d) CTZ(20) films after sulfurization for (a,c) 1 min and (b,d) 2 min.

Since the metallic stack used in this study was deposited in the order of Cu, Sn and Zn, the Cu layer was on the bottom of the as-deposited metallic stack. As mentioned above, sulfurization of the metallic stack without preheating induced significant formation of the Cu_xS compound. Based on these facts, preferable reaction between Cu and sulfur vapor was likely to be induced by out-diffusion of the bottom Cu component to the surface; this would lead to inhomogeneous distribution of the Cu component to form the Cu_2SnS_3 secondary phase and formation of many voids and crevices in the resulting CZTS film. When the 350-°C preheated precursor was employed, however, formation of the Cu_xS compound was significantly suppressed. The difference is attributed to the formation of Cu_6Sn_5, Cu_3Sn and Cu_5Zn_8 alloys, which would suppress the preferential reaction between metallic Cu and sulfur vapor. Instead, relatively reactive or unstable sulfurized compounds were probably formed from Cu_6Sn_5, Cu_3Sn and Cu_5Zn_8 alloys; conversion of them into the CZTS phase occurred promptly. Significant differences in structures of CZTS films obtained from the metallic precursors without and with preheating treatment shown in Fig. 5 are, therefore, attributed to the differences in the growth mechanism of the CZTS phase between them. In addition, there is no experimental evidence to explain the morphological inhomogeneity observed on the CZTS film derived from the metallic precursor with preheating for longer (40 min) duration (see Figs. 5c and 5f). As mentioned above, overgrowth of Cu_6Sn_5 and Cu_5Zn_8 alloys during the 350-°C preheating accompanied with the formation of appreciable voids, is likely to induce reduction of the rate of grain growth of the CZTS phase, leading to remaining appreciable small grains in the final CZTS film.

Solar cells with a device structure of glass/Mo/CZTS/CdS/Al:ZnO were prepared by depositing CdS and Al:ZnO layers on CZTS films prepared from CTZ(0), CTZ(20), and CTZ(40). *J-V* characteristics of these cells under simulated AM1.5 irradiation are shown in Fig. 8. It clear that the *J-V* curve of the cell based on the CZTS film derived from CTZ(0) shows quite poor electrical rectification: it gave conversion efficiency (η) of only 0.43%, as shown in Fig. 8a. As discussed above, appreciable crevices and voids in the CZTS film should induce significant cell leakage. The presence of the Cu_2SnS_3 secondary phase (as well as other unidentified impurities) in the CZTS film would also act as a shunt pass. Owing to these structural failures, the CZTS film was not useful for photovoltaic application. On the other hand, solar cells based on CZTS films derived from CTZ(20) and CTZ(40) exhibited an appreciable performance (Figs. 8b and 8c). The CZTS-based cell derived from CTZ(20) exhibited better performance, with η of 5.6%, short circuit current density (J_{SC}) of 19.8 mA cm^{-2}, open circuit potential (V_{OC}) of 0.64 V and fill factor (FF) of 0.45, than that of the cells obtained from the CTZ(40) metallic precursor (η = 2.6%, J_{SC} = 17.5 mA cm^{-2}, V_{OC} = 0.50 V, and FF = 0.30). As can be seen in Fig. 8c, the J-V curve of the CZTS-based cell derived from CTZ(40) shows relatively poor electrical rectification: it had a low shunt resistance (R_{sh} = 0.04 kΩ cm^{-2}) and a high series resistance (R_s = 15 Ω cm^{-2}). The less-packed nature of the CZTS film (Fig. 5c) led to the generation of an appreciable shut pass: the low R_{sh} significantly reduced V_{OC}. Moreover, the presence of appreciable amounts of voids at the interface of CZTS and Mo/glass and relatively thick MoS_2 layer (Fig. 5f) should cause such inferior qualities of ohmic contact: the resulting high R_s led to a drop in the FF value as well as a decrease in J_{SC}. On the other hand, the CZTS solar cell obtained from the CTZ(20) metallic precursor shows good rectification, as can be seen in Fig. 8b. Significant improvement of V_{OC} compared to that of the CZTS-based cell derived from CTZ(40) film is due to the high degree of compactness of the CZTS film, which leads to suppression of shunting, *i.e.*, it has relatively high R_{sh} (0.15 kΩ cm^{-2}). Large values of FF and J_{SC} are attributed to the good adherence between the CZTS film as well as relatively thin MoS_2 layer, resulting in the efficient majority carrier (hole) transport, thus leading to relatively low R_s (7.6 Ω cm^{-2}).

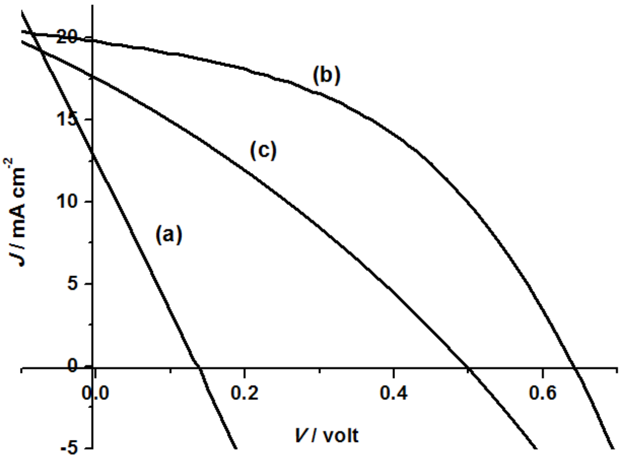

Figure 8. Light J-V data of CZTS-based solar cells derived from (a) CTZ(0)**,** (b) CTZ(20), and (c) CTZ(40).

Fig. 9 shows the external quantum efficiency (EQE) spectrum of the best cell (*i.e.*, the cell derived from CTZ(20)) in wavelength ranging from 300 nm to 1000 nm. The EQE spectrum increases gradually from the onset at *ca.* 350 nm to *ca.* 450 nm, steeply rises to *ca.* 520 nm, and then declines gradually to the onset wavelength of *ca.* 900 nm, corresponding to the band gap energy of CZTS (1.5 eV).[1,3] The reduction of EQE response in the short wavelength region is due to absorption losses in the window (Al:ZnO) and buffer (CdS) layers. On the other hand, the gradual weakening of the EQE response in the long wavelength region indicates loss of deeply absorbed photons due to poor minority carrier diffusion length and/or insufficient penetration of depletion width into the absorber [16,31]. Such a failure would be caused by high majority carrier concentration of the CZTS film, *i.e.*, defect density in the CZTS film is still too high to achieve an optimum. Thus, further investigation should be carried out to improve the device performance by efficient production of a well-defined CZTS film with a small amount of defects and majority carrier density.

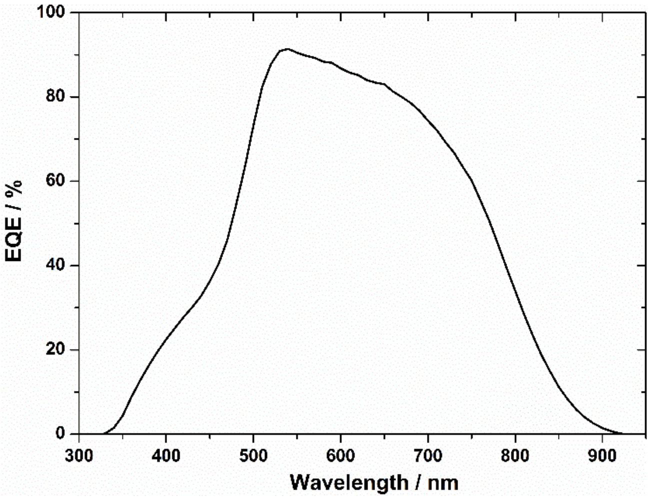

Figure 9. An EQE spectrum of the CZTS-based solar cells derived from CTZ(20).

3.1.4. Conclusion

In this study, we showed importance of preheating of the electrodeposited metallic stack composed of Cu, Sn, and Zn layers to obtain a CZTS film with a good compactness, homogeneity and adhesion to the bottom Mo layer. The solar cell with a glass/Mo/CZTS/CdS/Al:ZnO structure derived from the CZTS film was shown to have efficient device performance with conversion efficiency of more than 5%. Although the efficiency achieved is significant among the CZTS-based cells reported in the literature, there is still room for further improvement in device performance. A limiting factor of the best cell is insufficient utilization of photons of relatively long wavelength, as a result of a highly doped state of the CZTS film. We believe that this failure can be improved by further optimization of preheating conditions as well as precise control of metallic compositions. Since the various parameters can be changed in the preheating process and since the electrodeposition can simply control amounts of deposited metals by changing deposition durations and/or potentials, further investigations along these lines are now in progress.

References

[1] H. Katagiri, K. Saitoh, T. Washio, H. Shinohara, T. Kurumadani, S. Miyajima, Sol. Energy Mater. Sol. Cells, 65 (2001) 141-148.

[2] K. Ito, T. Nakazawa, Jpn. J. Appl. Phys. 1, 27 (1988) 2094-2097.

[3] S. Chen, A. Walsh, J.-H. Yang, X. Gong, L. Sun, P.-X. Yang, J.-H. Chu, S.-H. Wei, Phys. Rev. B, 83 (2011) 125201.

[4] W. Shockley, H. J. Queisser, J. Appl. Phys., 32 (1961) 510-519.

[5] L. M. Peter, Philosophical Trans. Ser. A, Math., Phys. Eng. Sci., 369 (2011) 1840-1856.

[6] C. Wadia, A. P. Alivisatos, D. M. Kammen, Environ. Sci. Technol., 43 (2009) 2072-2077.

[7] B. Shin, O. Gunawan, Y. Zhu, N. A. Bojarczuk, S. J. Chey, S. Guha, Prog. Photovolt.: Res. Appl., DOI: 10.1002/pip.1174.

[8] H. Katagiri, K. Jimbo, S. Yamada, T. Kamimura, W. S. Maw, T. Fukano, T. Ito, T. Motohiro, Appl. Phys. Express, 1 (2008) 041201.

[9] S. E. Habas, H. A. S. Platt, M. F. A. M. van Hest, D. S. Ginley, Chem. Rev., 110 (2010) 6571-6594.

[10] Y. B. K. Kumar, G. S. Babu, P. U. Bhaskar, V. S. Raja, 93 (2009) 1230-1237.

[11] Y. Miyamoto, K. Tanaka, M. Oonuki, N. Moritake, H. Uchiki, Jpn. J. Appl. Phys., 47 (2008) 596-597.

[12] Z. Zhou, Y. Wang, D. Xu, Y. Zhang, Sol. Energy Mater. Sol. Cells, 94 (2010) 2042-2045.

[13] T. K. Todorov, K. B. Reuter, D. B. Mitzi, Adv. Mater., 22 (2010) E156-E159.

[14] T. K. Todorov, J. Tang, S. Bag, O. Gunawan, T. Gokmen, Y. Zhu, D. B. Mitzi, Advanced Energy Materials, DOI: 10.1002/aenm.201200348.

[15] A. Ennaoui, M. Lux-Steiner, A. Weber, D. Abou-Ras, I. Kotschau, H.W. Schock, R. Schurr, A. Holzing, S. Jost, R. Hock, T. Voss, J. Schulze, A. Kirbs, Thin Solid Films, 517 (2009) 2511-2514.

[16] J. J. Scragg, D. M. Berg, P. J. Dale, J. Electroanal. Chem., 646 (2010) 52-59.

[17] S. Ahmed, K. B. Reuter, O. Gunawan, L. Guo, L. T. Romankiw, H. Deligianni, Adv. Energy Mater., 2 (2012) 253-259.

[18] S. M. Lee, S. Ikeda, T. Yagi, T. Harada, A. Ennaoui and M. Matsumura, Phys. Chem. Chem. Phys., 13 (2011) 6662-6669.

[19] S. M. Lee, S. Ikeda, Y. Otsuka, T. Harada, M. Matsumura, Electrochim. Acta, 79 (2012) 189-196.

[20] E. Guaus, J. Torrent-Burgués, J. Electroanal. Chem., 575 (2005) 301-309.

[21] J. von Appen, R. Dronskowski, K. Hack, J. Alloy. Comp., 379 (2004) 110-116.

[22] D. B. Mitzi, O. Gunawan, T. K. Todorov, K. Wang, S. Guha, Sol. Energy Mater. Sol. Cells, 95 (2011) 1421-1436.

[23] P. A. Fernandes, P. M. P. Salomé, A. F. da Cunha, Thin Solid Films, 517 (2009) 2519-2523.

[24] P. A. Fernandes, P. M. P. Salomé, A. F. da Cunha, phys. stat. sol. c, , 7 (2010) 901-904.

[25] P. A. Fernandes, P. M. P. Salomé, A. F. da Cunha, J. Phys. D: Appl. Phys., 43 (2010) 215403.

[26] S. Chen, X. Gong, A. Walsh, S. H. Wei, Appl. Phys. Lett., 96 (2010) 021902.

[27] A. Walsh, S. Y. Chen, S. H. Wei, X. G. Gong, Adv. Energy Mater., 2 (2012) 400-409.

[28] H. Katagiri, K. Jimbo, W. S. Maw, K. Oishi, M. Yamazaki, H. Araki, A. Takeuchi, Thin Solid Films, 517 (2009) 2455-2460.

[29] H. Yoo, J. Kim, L. Zhang, Curr. Appl. Phys., 12 (2012) 1052-1057.

[30] H. Yoo, J. Kim, Sol. Energy Mater. Sol. Cells, 95 (2011) 239-244.

[31] I. Repins, C. Beall, N. Vora, C. DeHart, D. Kuciauskas, P. Dippo, B. To, J. Mann, W. C. Hsu, A. Goodrich, R. Noufi, Sol. Energy Mater. Sol. Cells, 101 (2012) 154-159.

3.2. Fabrication of $CuSbS_2$ Thin Films from Electrodeposited Metallic Stack and Its Photovoltaic Applications

3.2.1. Introduction

Recently, alternative ternary copper sulfides based on Cu-Sb-S and Cu-Bi-S materials such as $CuSbS_2$ and $CuBiS_2$ are expected to be promising absorber materials for sustainable and scalable photovoltaics because of their optimal E_gs (1.52eV for $CuSbS_2$ and 1.65eV $CuBiS_2$) as well as containing less-toxic and abundant elements when compared to CdTe and CIGS [1,2]. Recent theoretical studies also predicted that these materials have strong optical absorption with absorption coefficients of more than 10^4 cm^{-1} [3], which is almost comparable to the above chalcopyrite and kesterite materials. Hence, various fabrication methods, such as thermal evaporation [4,5], and non-vacuum methods such as chemical bath deposition (CBD) [6,7], spray pyrolysis [8], and electrodeposition [9,10] have been reported for fabrication of these I-IV-VI chalcogenide thin films. However, only a study reported application of these thin films to complete device: the device based on the $CuSbS_2$ only gave quite low photovoltaic performance (open-circuitvoltage (V_{OC}) of 345 mV and a short circuit current (J_{SC}) of 0.2 mA/cm^2), due probably to less-crystalline nature of the used $CuSbS_2$ film [7].

Electrochemical approach is one of the desirable methods for fabrication of the I-IV-VI chalcogenide films because of its several advantages, including low equipment cost, negligible waste of chemicals with utilization efficiencies close to 100%, possible formation of a compact film required for solar cell application, scalability, and manufacturability of a large-area polycrystalline film. Previous work in our group has shown that a similar fashion can be used to fabricate $CuInS_2$ and Cu_2ZnSnS_4 thin films [11-13]. These facts and results motivated us to investigate the production of these I-IV-VI chalcogenide films through the electrochemical route for the use of efficient absorbers for solar cells. In this study, therefore, we attempted to fabricate one of the promising I-IV-VI chalcogenide thin-film absorber of $CuSbS_2$. Structural and morphological properties related to solar cell performance related to solar cell performances are discussed in detail.

3.2.2. Experimental

Metallic Cu and Sb layers were electrochemically deposited under potentiostatic control using a Hokuto Denko HSV-100 potentiostat-galvanostat. Three-electrode setup composed of a Mo-coated glass working electrode, a platinum sheet counter electrode, and an Ag/AgCl reference electrode was used for the deposition. The deposition of Cu was performed at potential of -0.4 V (vs. Ag/AgCl) in an electrolyte containing 15 mM $CuSO_4$ and 15 mM citric acid. Then the Sb layer was deposited at potential of -0.3 V vs. Ag/AgCl from an electrolyte containing 15 mM $K_2(Sb_2(C_4H_2O_6)_2$and 50 mM tartaric acid, with a pH adjusted to 1.3 by addition of H_2SO_4. During the depositions, temperature of the electrolytes was kept at 25°C by using a water bath. The amount of each deposited metal was fixed by controlling the electric charge during deposition using a Hokuto Denko HF-201A couloumb/amperehour meter: electric charges for depositions of Cu and Sb were maintained at 0.74 C/cm^2 and 1.1 C/cm^2, respectively, *i.e.*,the atomic ratios of Cu/Sb was fixed to be unity.

The stacked metal precursor was then sulfurized at 450 °C for 30 min under H_2S (5% in Ar) flow to form $CuSbS_2$ (CAS(A)). We also performed sulfurization of the precursor using a different heating profile, i.e., the stacked metal precursor was heated at 510 °C for 60 min under argon (Ar) and then subsequently sulfurized at 450 °C for 30 min under flow of 5% H_2S; thus-obtained $CuSbS_2$ film was labeled CAS(B). Morphologies of the films were examined by scanning electron microscopy (SEM) using a Hitachi S-5000 FEG scanning electron microscope. Crystal structures of the films were measured by X-ray diffraction (XRD) using a Rigaku Mini Flex X-ray diffractometer (CuKα, Ni filter).

For evaluation of solar cell properties of $CuSbS_2$ films, they were processed to form an glass/Mo/$CuSbS_2$/CdS/Al:ZnO structure. After immersion of the $CuSbS_2$ films in an aqueous KCN solution (10%) for 2 min to clean their surfaces, a CdS buffer layer was deposited by chemical bath deposition (CBD). Then an Al:ZnO transparent conductive oxide was deposited on the top of the CdS layer by radio frequency (RF) magnetron sputtering. Current density-voltage (*J*-*V*) characteristics of thus-obtained devices under simulated AM1.5 irradiation (100 mW cm^{-2}) through the Al:ZnO window layer and those under dark (without photoirradiation) were measured with a Bunkoh–Keiki CEP–015 photovoltaic measurement system.

3.2.3. Result and discussion

Fig. 1 shows SEM images of the electrodeposited Cu layer and the Cu/Sb stacked layer. It is apparent that the Cu-layer was dense and consisted of round-shaped grains with sizes less than 1 μm (Fig. 1a). Upon electrodeposition of Sb layer on the top of the Cu-layer (see Fig. 1b), the Sb layer homogenously covered the underlying Cu surface, as can be seen from the appearance of angular-shaped grains on the whole surface of the film. The Sb deposition resulted in a change of the color of the film from a metallic-orange (Cu-like color) into a metallic-grey (Sb-like color). Corresponding cross-sectional image (see Fig. 1c) clearly showed almost complete coverage of a rough Sb layer on the top of homogeneous Cu-layer with the thicknesses of each layer were *ca.*0.3 μm and 0.85 μm, respectively.

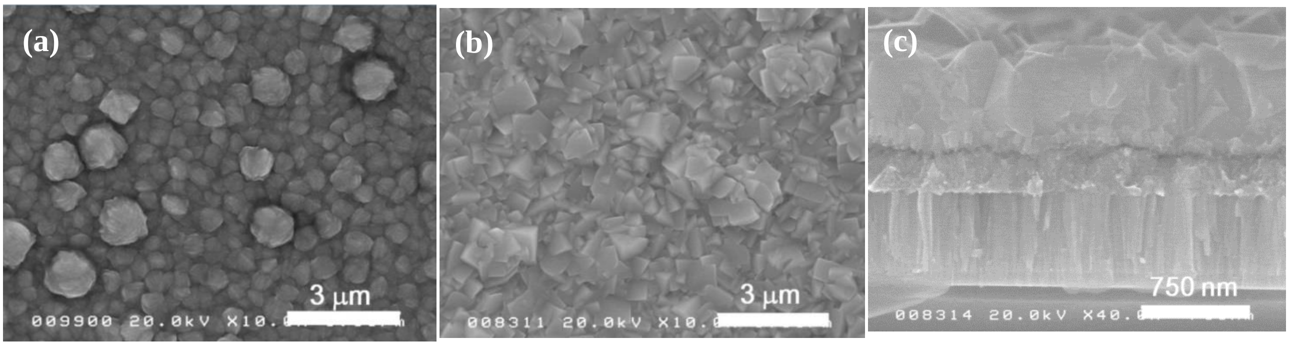

Figure 1. SEM images of electrodeposited (a) Cu layer, (b, c) Cu/Sb stacked layer.

The XRD pattern of the metallic stack after sulfurization at 450 °C for 30 min under H_2S flow (i.e., the CAS(A) film) indicated conversion of the film into the $CuSbS_2$ compound (JCPDS 44-1417), as shown in Fig. 2a. However, there were appreciable reflections assignable to Sb_2S_3 (JCPDS 42-1393) and an unidentified peak at 2θ of 44.5°. Extension of sulfurization duration and increase in sulfurization temperature were not effective to eliminate these impurities: since such changes in the sulfurization profile often induced peeling-off of the film from the Mo/glass substrate, we could not yet perform systematical investigations of sulfurization parameters by using these simple sulfurization profiles. In order to reduce the formation of impurity phases and peeling-off, we added a preheating treatment at 510 °C for 30 min under Ar just before the sulfurization. Fig. 2b shows the XRD pattern of thus-obtained film (CAS(B)). Except for the unidentified peak at 2*θ* of 44.5°, all the reflections of the CAS(B) film were assigned to $CuSbS_2$, i.e., formation of the Sb_2S_3 phase could be avoided by applying such a preheating treatment.

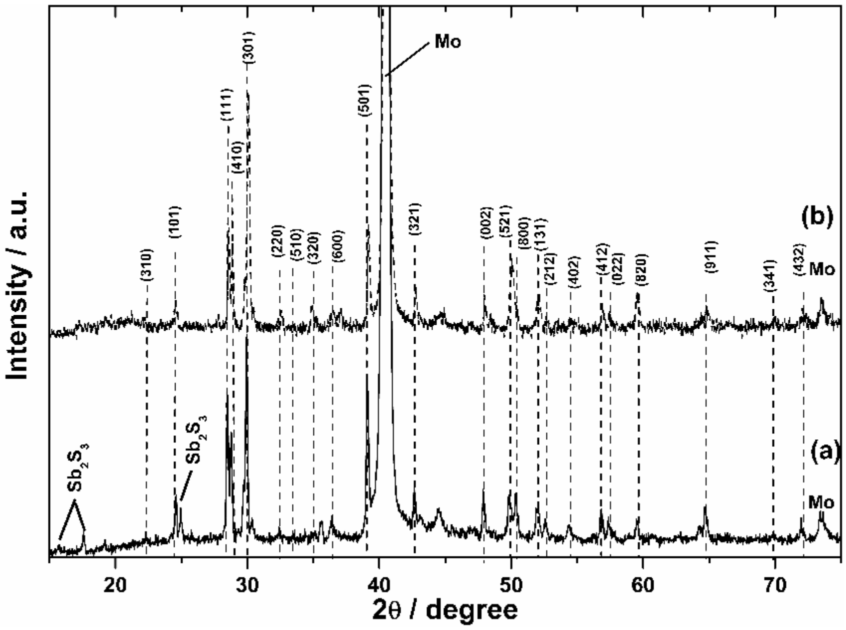

Figure 2. XRD patterns of (a) CAS(A) and (b) CAS(B).

Fig. 3 shows SEM images of CAS(A) and CAS(B). While the top-view SEM image of CAS(A) shows formation of densely packed micron-sized grains, the film also contained appreciable pinholes between these grains, as shown in Fig. 3a. Moreover, corresponding cross-section clearly shows presences of significant voids at the interface between the CAS(A) film and the Mo/glass substrate (Fig. 3b). When compared to the CAS(A) film, the $CuSbS_2$(B) film had a dense morphology and relatively big and homogenous grains sizes compared to those of the CuSbS$_2$(A) film: there is no pinhole on the entire surface of the CuSbS$_2$(B) film (Fig. 3c). As shown in Fig. 3d, moreover, the cross-sectional image of the CuSbS$_2$(B) film shows relatively good adhesion to the Mo substrate and almost no appreciable void which was observed in the CAS(A) film.

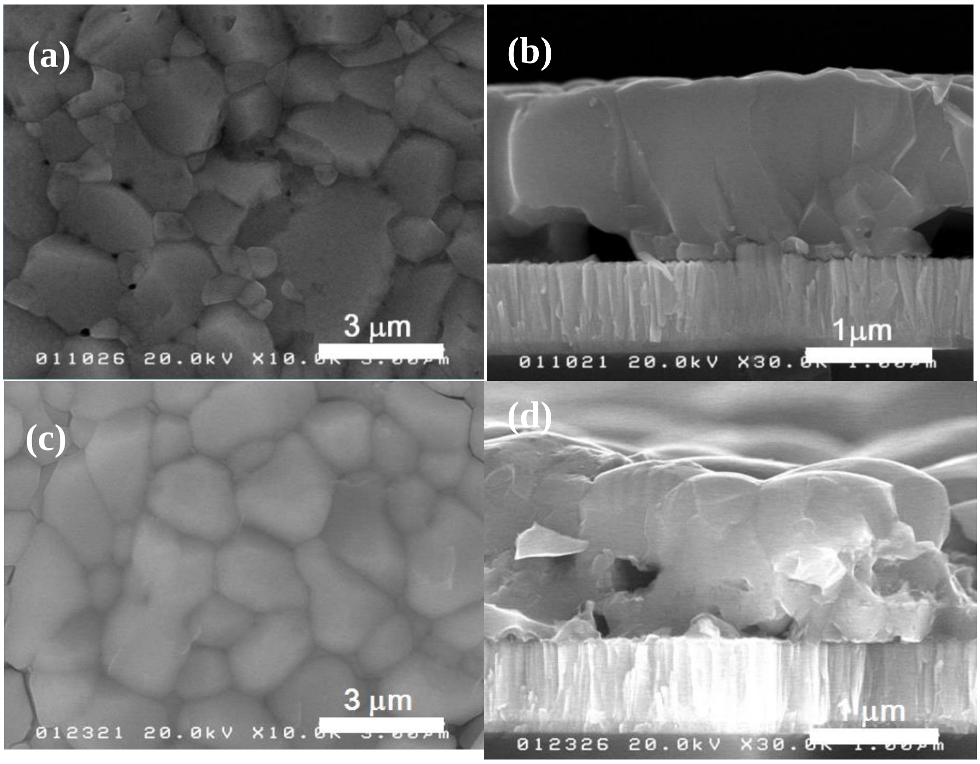

Figure 3. Top view (a, c) and (b, d) cross-sectional SEM images of (a, b) CAS(A) and (c, d) CAS(B).

In order to examine the effect of the pretreating at 510 °C in Ar, structural changes of the Cu/Sb metallic stack were evaluated by the XRD analyses. Fig.4 showsthe results. The XRD pattern of the Cu/Sb stacked film before the 510-°C pretreating consisted of a mixture of metallic Sb (JCPDS 35-0732), Cu (JCDPS 04-0836) and the Cu$_2$Sb compound (JCPDS 87-1176), as shown in Fig. 4a. Presence of the Cu$_2$Sb compound in as-deposited film indicates an appreciable interdiffusion between Cu and Sb during the electrochemical coverage with Sb at room temperature. In fact, the phase diagram of this binary compound implies preferable formation of the Cu_2Sb phase at temperatures below 526 °C when the atomic ratio of Cu to Sb is less than 2 [14]. Upon heating the stacked layer at 510 °C in Ar, the Cu_2Sb reflections become more intense and well-resolved, indicating significant intermixing of the metals and the formation of crystalline Cu_2Sb although minor trace from an unmixed Sb was still detected (Fig. 4b).

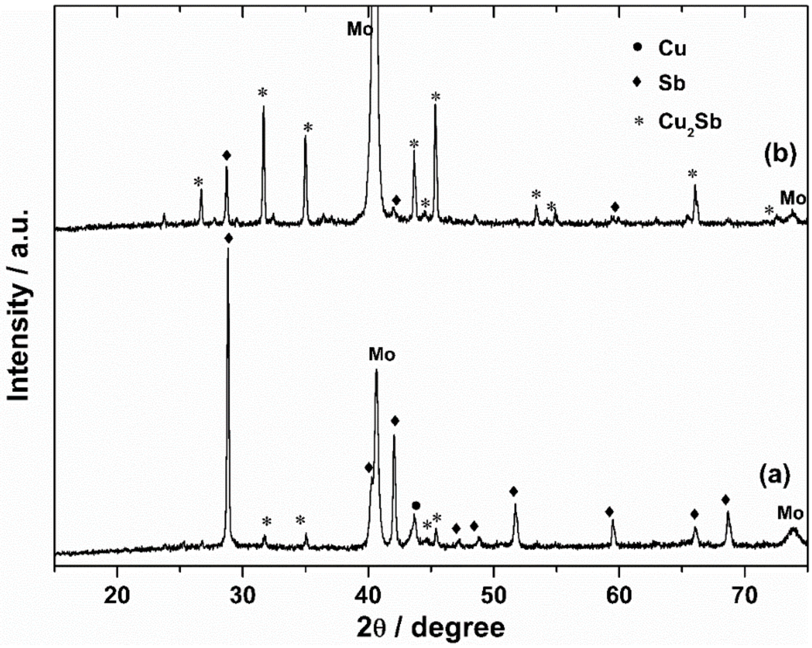

Figure 4. XRD patterns of (a) electrodeposited Cu/Sb stacked layer and (b) that heated at 510 °C in Ar.

As has been discussed previously regarding sulfurization of Cu/In and Cu/Sn/Zn metallic stacks for fabrication of $CuInS_2$ and Cu_2ZnSnS_4 thin-films [11,13], formation of significant voids between these chalcogenide thin-films and the Mo/glass substrate was due to preferable reaction between Cu and sulfur vapor to produce a Cu_xS compound. The reaction would induce out-diffusion of the bottom Cu component to the surface, leading to leaving an empty space at the bottom part of the film. Moreover, the preferable Cu_xS formation might also induce inhomogeneous distribution of the Cu component, resulting ininsufficient grain growth of the $CuSbS_2$ phase, formation of the Sb_2S_3 secondary phase, and productions of appreciable pinholes between these grains. When the 510-°C preheating in Ar was added to the Cu/Sb precursor, however, formation of the Cu_xS compound could be suppressed by the formation of Cu_2Sb alloy, which would suppress the preferential reaction between metallic Cu and sulfur vapor. Instead, relatively reactive or unstable sulfurized compounds were probably formed from the Cu_2S alloy; conversion of them into the $CuSbS_2$ phase occurred promptly.

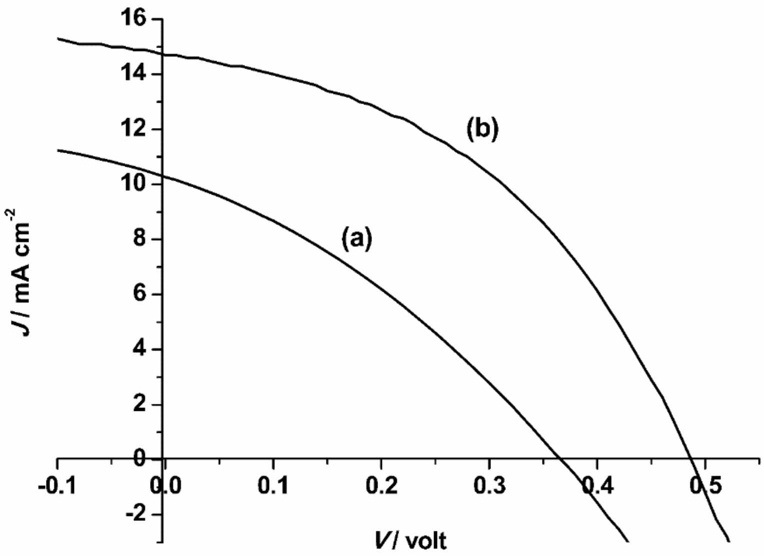

Figure 5. *J*-*V* curves of glass/Mo/$CuSbS_2$/CdS/Al:ZnO devices derived from (a) CAS(A) and (b) CAS(B).

The $CuSbS_2$ films were transferred into devices with a structure of glass/Mo/$CuSbS_2$/CdS/Al:ZnO. Fig.5 shows *J*-*V* curves of the devices. It is evident from the curve that all the devices exhibited solar cell performances. Best conversion efficiencies of 1.24% (J_{SC}: 10.27 mA/cm^2,V_{OC}: 0.37 V, FF:0.33) and 3.13% (J_{SC}: 14.73 mA/cm^2, V_{OC}: 0.49 V, FF: 0.44) were achieved from the devices using CAS(A) and CAS(B) films, respectively. It is apparent that all the solar cell properties of the CAS(B)-based device were superior compared to those of the CAS(A)-based device. Differences in these solar cell properties could be related to above-discussed structural and morphological properties of the CAS(B) film. For example, due to the improvement of adhesion to the Mo/glass substrate, the CAS(B)-based device should decrease interfacial resistance between the $CuSbS_2$ film and the Mo/glass substrate. Extinction of pinholes in the CAS(B) film would suppress the cell leakage. Moreover, disappearance of the Sb_2S_3 secondary phase in the CAS(B) film might reduce carrier recombination probability.

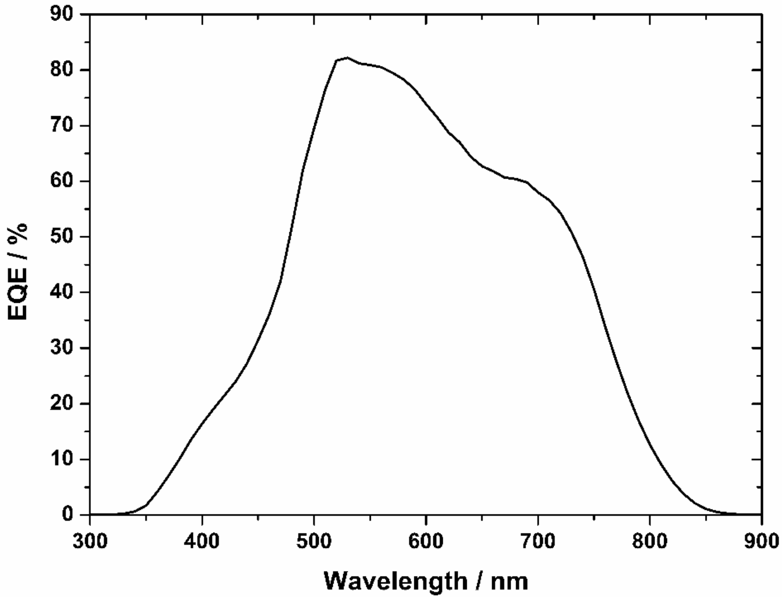

Figure 6. EQE spectra of the device and derived from CAS(B).

Fig. 6 shows the EQE spectrum of the best device (i.e., the CAS(B)-based device). There are several features and problems of the present device. First, a significant loss of the EQE at wavelength shorter than ca. 550 nm was observed due to the photoabsorption by TCO (Al:ZnO, Eg = 3.3 eV[15])and n-type buffer (CdS, Eg = 2.4 eV[16]) layers in the present device, Second,there is also a non-linear decrease of the EQE at wavelengths longer than ca. 550 nm, i.e., the EQE gradually decreases in the wavelengths between ca. 550 nm and ca. 650 nm, becomes flat at wavelengths up to ca. 750 nm, and then again decreases steeply to the onset wavelengths of ca. 850 nm, as corresponded to the band gap energy of $CuSbS_2$ (ca. 1.5 eV).As has been reported in the literature, the flattening of the EQE at ca. 650-750 nm was caused by the optical characteristic of the $CuSbS_2$ [3]. On the other hand, the overall gradual decrease of the EQE in this region was likely to be due to the insufficient minority carrier diffusion length of the present $CuSbS_2$, as has been frequently observed in the CZTS-based solar cell. In order to improve the conversion efficiency, therefore, further optimization of properties/qualities of the $CuSbS_2$ film should be required. Since the maximum EQE value of the present cell only reached 0.8 (at 530nm), moreover, improvements of junction properties (i.e., optimizations of materials and methods for deposition of n-type layer) were also required.

3.2.4. Conclusion

In the present study, we examined the fabrication of $CuSbS_2$-based solar cell from an electrodeposited Cu/Sb stacked layers followed by sulfurization under at 450 ^oC in H_2S gas for 30 min. We found that the preheating under Ar to the stacked layer prior to the sulfurization was beneficial to obtain the $CuSbS_2$ film with a dense structure and a good adherence to the Mo substrate. A promising maximum conversion efficiency of 3.13% has been achieved with the solar cell device using this approach. This result is promising considering the use of new material for thin film solar cell. In order to improve the photovoltaic performance, various optimizations, such as sulfurization conditions, precise control of Cu/Sb atomic ratio, thickness of the $CuSbS_2$ film, choices of optimum buffer layers, can be estimated. Hence, studies along with these lines are now in progress.

References

[1] J. T. R. Dufton, A. Walsh, P. M. Panchmatia, L. M. Peter, D. Colombara, M. Saiful Islam, Phys. Chem. Chem. Phys., 14 (2012) 7229.

[2] D. J. Temple, A. B. Kehoe, J. P. Allen, G. W. Watson, D. O. Scanlon, J. Phys. Chem. C,

116 (2012) 7334.

[3] L. Yu , R. S. Kokenyesi , D. A. Keszler, A. Zunger, Adv. Energy Mater., 3 (2013) 43.

[4] C. Garza, S. Shaji, A. Arato, E. P. Tijerina, G. A. Castillo, T. K. Das Roy and B. Krishnan, Sol. Energy Mater. Sol. Cells, 95 (2011) 2001.

[5] A. Rabhi, M. Kanzari and B. Rezig, Mater. Lett., 62 (2008) 3576.

[6] Y. Rodriguez-Lazcano, M. T. S. Nair and P. K. Nair, J. Cryst. Growth, 223 (2001) 399.

[7] Y. Rodriguez-Lazcano, M. T. S. Nair and P. K. Nair, J. Electrochem. Soc., 152 (2005) G635.

[8] S. Manolache, A. Duta, L. Isac, M. Nanu, A. Goossens and J. Schoonman, Thin Solid Films, 515 (2007) 5957.

[9] D. Colombara, L. M. Peter, K. D. Rogers, J. D. Painter and S. Roncallo, Thin Solid Films, 519 (2011) 7438.

[10] D. Colombara, L. M. Peter, K. D. Rogers and K. Hutchings, J. Solid State Chem., 186 (2012) 36.

[11] S. M. Lee, S. Ikeda, T. Yagi, T. Harada, A. Ennaoui and M. Matsumura, Phys. Chem. Chem. Phys., 13 (2011) 6662.

[12] S. M. Lee, S. Ikeda, Y. Otsuka, T. Harada, M. Matsumura, Electrochim. Acta, 79 (2012) 189.

[13] Yixin Lin,1,2 Shigeru Ikeda,1,* Wilman Septina,1 Takashi Harada,1 and Michio Matsumura1 SOLMAT

[14] X. Liu, C. Wang, I. Ohnuma, R. Kainuma and K. Ishida, *J. Phase Equilib.*, 21 (2000) 432.

[15] A. I. Oliva, O. Solis-Canto, R. Castro-Rodriguez and P. Quintana, Thin Solid Films, 391 (2001) 28.

[16] J. J. Scragg, D. M. Berg and P. J. Dale, J. Electroanal. Chem., 646 (2010) 52.

Chapter 4

Electrochemical Deposition of Cu_2O Thin Films for Photovoltaic Applications

4.1. Potentiostatic Electrodeposition of Cu_2O for Cu_2O/Al:ZnO Solar Cell

4.1.1. Introduction

Cuprous oxide (Cu_2O) is a p-type metal oxide semiconductor with a band gap of approximately 1.9 - 2.1 eV, i.e., it absorbs visible light of wavelengths up to 650 nm. Cu_2O is an abundant and economically available material with low toxicity. Moreover, this material is known to have sufficient mobility and a relatively large minority carrier diffusion length. Due to these specific features, fabrication of solar cells based on a Cu_2O photoabsorber has been studied for a long time [1-13].

Because of the difficulty in obtaining n-type Cu_2O, Cu_2O-based solar cells have usually been composed of a heterojunction between Cu_2O and an n-type oxide. Of the wide variety of possible combinations for heterojunctions, renewed interest has recently been shown by several researchers in Cu_2O/ZnO and Al-doped ZnO (Al:ZnO) heterojunctions because of the favourable alignment of band edges: except for these combinations, there have been few reports on Cu_2O-based solar cells with an appreciable photovoltaic property [5-13]. The best conversion efficiency of 4.1% has been reported for a cell based on a Cu_2O/ZnO heterojunction [8], whereas the theoretical limit of the energy conversion efficiency of a Cu_2O-based solar cell is estimated to be ca. 20% [4].

As has been reported in the literature, Cu_2O films can be obtained by various techniques including sputtering [5], thermal [6-9] and anodic oxidation of metallic Cu sheets [3], photochemical deposition [10], and electrodeposition [11-17]. Among these fabrication methodologies, electrodeposition is a promising technology because of its advantages of low equipment cost, negligible waste of chemicals with utilization efficiencies close to 100%, and scalability and manufacturability of large-area polycrystalline films. Hence, many studies have focused on fabrication of Cu_2O/ZnO or Cu_2O/Al:ZnO heterojunctions by using the electrodeposition technique, though the efficiencies of these solar cells remain below 1.3% [12].

For the purpose of achieving optimum solar cell properties, we investigated fabrication of solar cells based on a Cu_2O/Al:ZnO heterojunction, which were prepared by using a potentiostatic electrodeposition process for growing a Cu_2O layer on an FTO glass substrate and subsequent deposition of an Al:ZnO layer by sputtering. Effects of applied potentials for the Cu_2O deposition on structural properties of the Cu_2O films and properties of the solar cells made of these films are discussed in detail.

4.1.2. Experimental

Electrodeposition of Cu_2O was carried out in a three-electrode setup consisting of a reference Ag/AgCl electrode, a copper sheet counter electrode, and an FTO-coated glass substrate (Asahi Glass Co. Ltd., sheet resistance of 10.8 Ω/square) as a working electrode. Before the electrodeposition, the FTO surface was precleaned by ultrasonication in ultrapure water, ethanol and acetone followed by exposure to oxygen (O_2) plasma (40 W, 7.5×10^{-5} Pa) for 15 min. The electrolyte used was composed of 0.2 M $CuSO_4$ and 3 M lactic acid with pH adjusted to 12.5 by addition of NaOH. The precleaned FTO-coated glass substrate was immersed in the electrolyte solution and electrodeposition was performed at fixed potentials ranging from -0.50 V to -0.65 V vs Ag/AgCl using a Hokuto Denko HSV-100 potentiostat-galvanostat at 60 ^{o}C. The amount of deposition was estimated by the electric charge using a Hokuto Denko HF-203D bipolar couloumb/amperehour meter. On the top of the Cu_2O film, an Al:ZnO film with a thickness of 200 nm was sputtered under RF power of 350W at room temperature for 5 min. The solar cell thus fabricated had a structure of glass/FTO/Cu_2O/Al:ZnO.

An Al layer was deposited at a corner of the AZO layer to make a good contact to a Cu lead wire. The solar cell properties were measured with a Bunkoh-Keiki CEP-015 photovoltaic measurement system under simulated AM 1.5 irradiation (100 mW cm^{-2}) through the Al:ZnO electrode.

The morphologies of the films were examined using a Hitachi S-5000 FEG field-emission scanning electron microscope (FE-SEM). Crystal structures and phase compositions of the films were measured by X-ray diffraction (XRD) analysis using a Rigaku MiniFlex X-ray diffractometer (Cu Kα, Ni filter). Oxidation states of copper components in the Cu_2O films were examined by X-ray photoelectron (XP) spectroscopy using a Shimadzu AXIS ULTRA X-ray photoelectron spectrometer. Photoelectrochemical measurements on the Cu_2O films were carried out using a three-electrode cell containing 0.5 M Na_2SO_4 electrolyte (pH = 6.7). A Pt wire and an Ag/AgCl electrode in saturated KCl served as the counter electrode and the reference electrode, respectively, and a Hokuto Denko HB-151 potentio-galvanostat was employed to obtain voltammograms. Photocurrents were measured under O_2 using the lock-in technique. Sample electrodes were illuminated with a monochromatized light chopped at a frequency of 10 Hz. The number of incident photons was determined with an OPHIR Orion Laser power meter equipped with a photodiode. Absorption spectra of the films were measured with a Hitachi U-4100 UV/vis/NIR spectrometer.

4.1.3. Results and Discussion

A Pourbaix diagram for the aqueous copper system suggests that deposition of Cu_2O occurs at pH larger than 4 in a limited potential window of about 0.3 V. In order to obtain suitable potentials for selective growth of a Cu_2O film, linear sweep voltammetry (LSV) was performed in the electrolyte consisting of 0.2 M $CuSO_4$ and 3 M lactic acid with pH adjusted to 12.5. The potential sweep started at 0 V vs. Ag/AgCl and was performed in the cathodic direction with a scan rate of 10 mV s^{-1}. It should be noted that addition of lactic acid, which works as a complexing agent for Cu^{2+}, is essential to prevent $Cu(OH)_2$ precipitation in the present basic electrolyte solution. Figure 1 shows a typical LSV curve obtained with the FTO-coated glass substrate immersed in the electrolyte solution at 60 °C. It is clearly shown in the figure that there are two different regions in the cathodic current curve: a gradual increase in the cathodic current at applied potentials ranging from -0.4 V to -0.65 V vs. Ag/AgCl and a remarkable rise in the cathodic current at potentials more negative than -0.65 V (vs Ag/AgCl). As has been reported in the literature [15-16], the former is attributed to the formation of Cu_2O and the latter indicates further reduction to form Cu metal. Since sufficient cathodic currents for selective Cu_2O deposition seem to appear at applied potentials ranging from -0.50 V to -0.65 V vs. Ag/AgCl, we fabricated Cu_2O films at different applied potentials in this region.

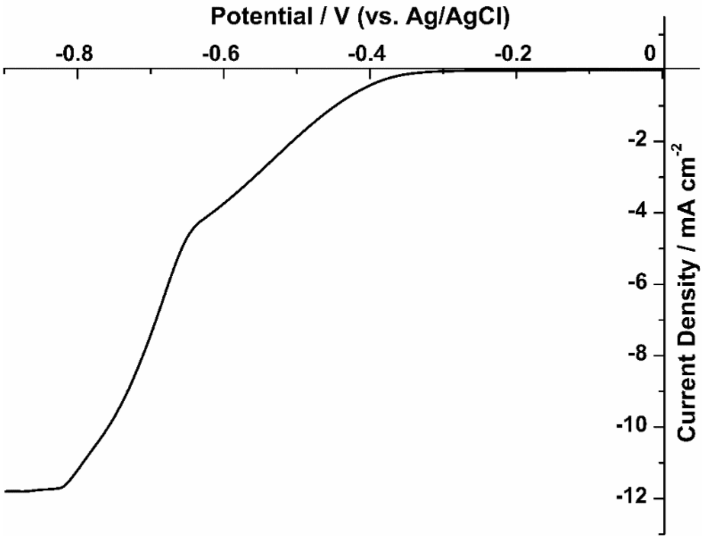

Figure 1. Linear sweep voltammogram for Cu_2O and Cu depositions in an alkaline electrolyte bath (pH 12.5) containing 0.2 M $CuSO_4$ and 3 M lactic acid at 60 °C.

Figure 2 shows representative FE-SEM images of thus-obtained Cu_2O films under different applied potentials. The cathodic charge was fixed at 1.4 C cm^{-2} for the deposition of these films. The thicknesses of the Cu_2O films were about 2.0μm, 2.0μm, 1.6μm, and 1.5μm for deposition at -0.50 V, -0.55 V, -0.60 V and -0.65 V vs. Ag/AgCl, respectively. The decrease in the thickness with the increase of negative potential is mostly due to increased compactness of the films. The top-view FE-SEM images indicate that all of the films consist of agglomerates of angular-shaped crystallites. Significant differences observed between these films are their grain sizes, i.e., Cu_2O grains in the film became smaller when deposited at more negative potentials: the grain sizes were estimated to be about 4, 2 , 1 and 0.8 μm for films deposited at potentials of -0.50 V, -0.55 V, -0.60 V and -0.65 V vs. Ag/AgCl, respectively. This is attributed to the fact that frequencies of nucleation of Cu_2O crystallites during the Cu_2O deposition tends to be higher when the applied potentials become more negative. Although a Cu_2O film having large grains is promising for photovoltaic applications because of the possible reduction of recombination probability at the grain boundaries, the Cu_2O film deposited at a potential of -0.50 V (vs. Ag/AgCl) contained voids between these large grains (Fig. 2a), which caused leakage current. As shown in Fig. 2c, the Cu_2O film deposited at a potential of -0.60 V (vs. Ag/AgCl) became more compact than the films deposited at a more positive deposition potential. Corresponding cross-sectional views of these films also indicate that the Cu_2O film deposited at a potential of -0.60 V has the flattest surface of all of the films prepared, whereas the same columnar shape was observed regardless of the deposition potential. Another point worth noting is that lumps of ca. 5 μm in diameter appeared on the surface of the Cu_2O film when deposited at -0.65 V (vs. Ag/AgCl), as shown in Fig. 2d. Although the formation mechanism of these lumps is not clear at present,

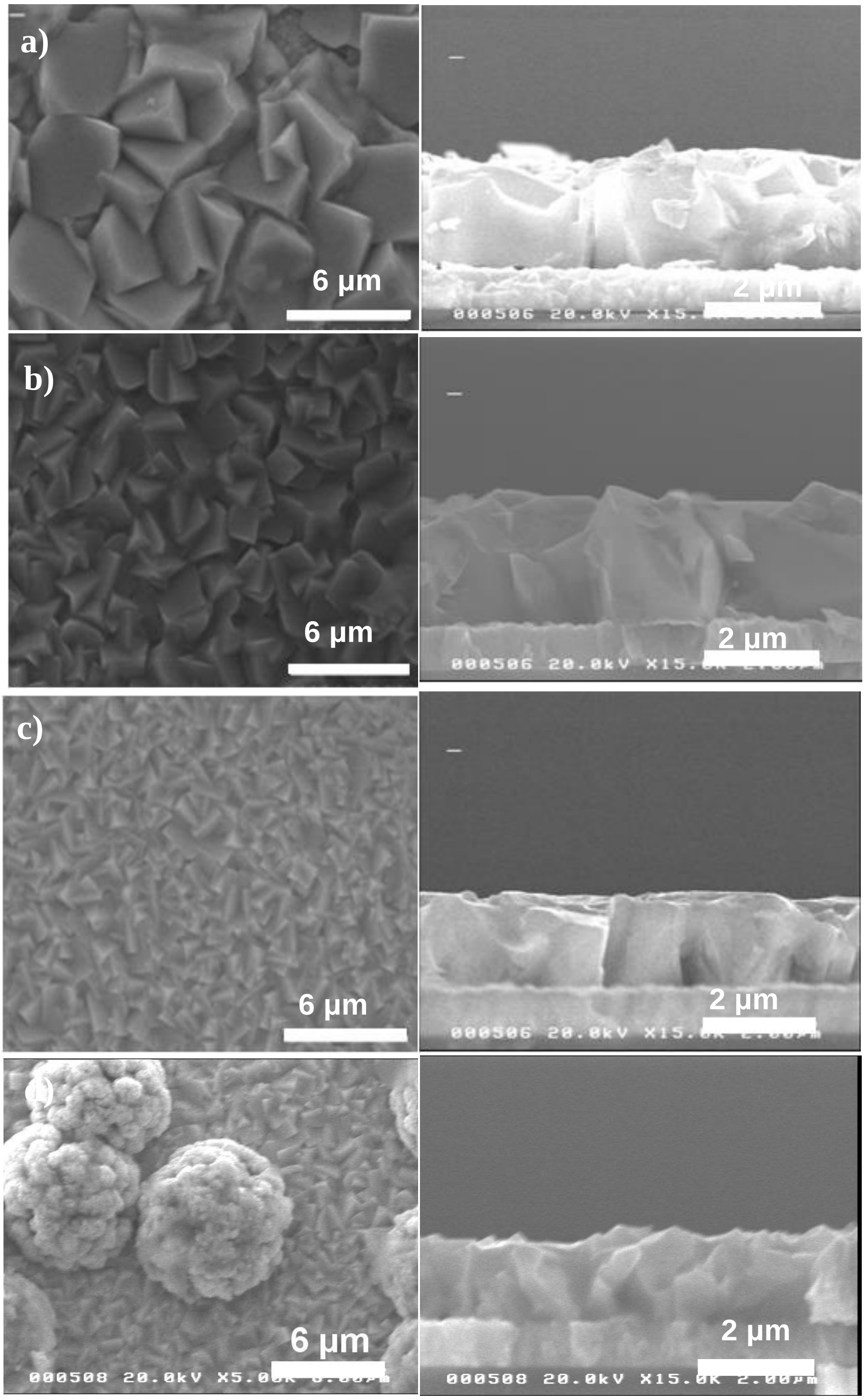

Figure 2. Top view and cross-sectional FE-SEM images of the electrodeposited Cu_2O films at different applied potentials: (a) -0.5 V, (b) -0.55 V, (c) -0.6 V, and (d) -0.65 V vs. Ag/AgCl.

they would interfere with properties of the heterojunction formed at the top part of the Cu_2O surface.

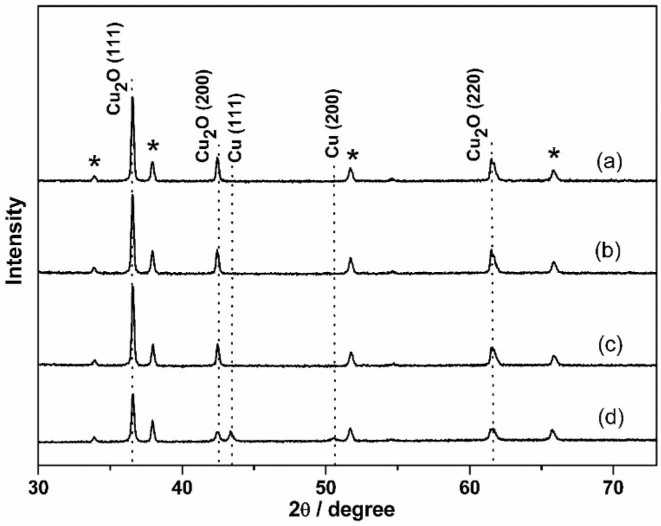

Figure 3. XRD patterns of electrodeposited films under different applied potentials: (a) -0.5 V, (b) -0.55 V, (c) -0.6 V, and (d) -0.65 V vs. Ag/AgCl. Asterisks denote diffraction peaks derived from the FTO substrate.

Figure 3 shows XRD patterns of Cu_2O films deposited at various applied potentials. XRD patterns of films obtained at applied potentials of - 0.50 V, - 0.55 V, and - 0.60 V vs. Ag/AgCl showed typical diffraction peaks assigned to Cu_2O (according to JCPDS 5-667) in addition to peaks due to the FTO substrate (Figs. 3a-3c). The relatively high intensity of the (111) peaks compared to that of (200) peaks indicates preference in the growth of these Cu_2O films towards the (111) direction [17]. In the film deposited at applied potential of -0.65 V vs. Ag/AgCl, appreciable peaks assignable to Cu metal appeared, accompanied by a significant decrease in intensities of Cu_2O peaks, implying less crystallinity of the film than that of films obtained at more positive potentials. The appearance of the Cu peaks suggests that the lumps observed on the surface of the Cu_2O film deposited at this potential are made of metallic Cu.

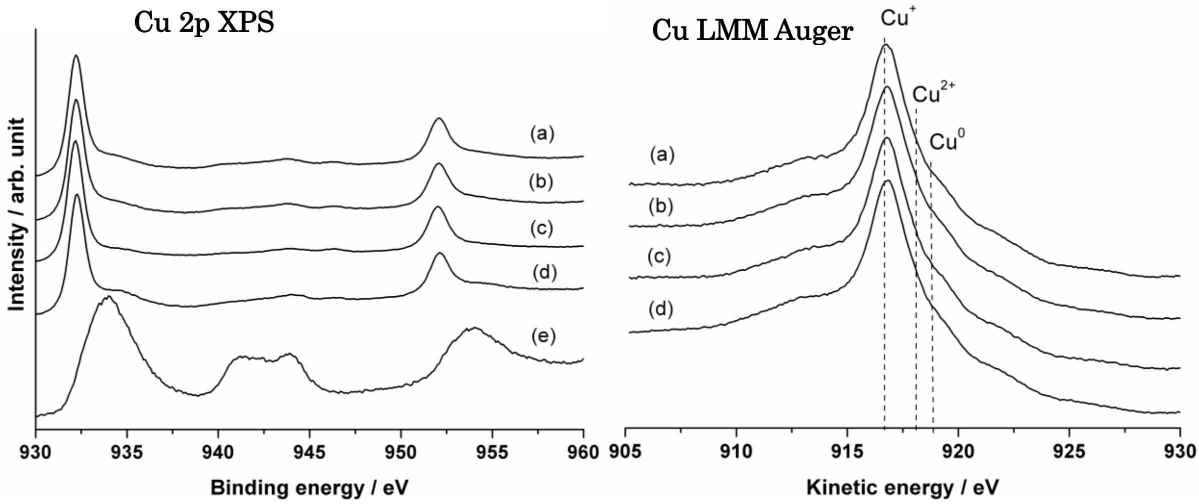

Figure 4. Cu 2p XP and Cu LMM Auger spectra of Cu_2O films prepared at (a) -0.5 V, (b) 0.55 V, (c) -0.6 V, and (d) -0.65 V vs. Ag/AgCl. (e) is a reference XP spectrum of CuO powder. The binding and kinetic energies were referenced to the C 1s level at 284.8 eV.

XP spectroscopic analyses were carried out for further evaluation of film qualities. Figure 4 shows Cu 2p XP and Cu LMM Auger spectra of Cu_2O films obtained at various applied potentials. A Cu 2p XP spectrum of the CuO powder is also shown as a reference (Fig. 4e). The binding energy positions of Cu^0 and Cu^+ on Cu 2p XP spectra are overlapped with only 0.2 eV difference, but they are distinguishable from Cu^{2+} by both their different peak binding energies and the absence/presence of a satellite structure at ca. 940-945 eV in binding energy, as shown in Fig. 4, and Cu LMM Auger spectra provide contents of Cu^0 and Cu^+ in these films [18-19]. It is interesting that weak peaks due to Cu^{2+} are observed in the Cu 2p XP spectra of all the films despite no CuO X-ray diffraction peaks being observed in the XRD patterns (Fig.

3). Moreover, weak peaks due to Cu^0 were also observed in Cu LMM Auger spectra of all the Cu_2O films. These results indicate incorporation of appreciable amounts of Cu^{2+} and Cu^0 impurities during the electrodeposition process. It should also be noted that the Cu_2O film deposited at -0.65 V did not show an intense Cu^0 peak in the Cu LMM Auger spectrum although it contained metallic Cu as evidenced by the XRD pattern (Fig. 3d). Since the film showed relatively intense peaks assigned to Cu^{2+} components in Cu 2p XP spectra in comparison with Cu_2O films prepared at more positive potentials, the surface of the lumps made of metallic Cu may be covered with a CuO/Cu_2O layers.

Photoelectrochemical measurements of the electrodeposited films were performed in 0.5 M Na_2SO_4 electrolyte, which was bubbled with O_2 as an electron acceptor. In this condition, all the Cu_2O electrodes deposited at potentials of -0.50 V to –0.65 V vs. Ag/AgCl showed appreciable photocurrents at potentials more negative than -0.2 V vs. Ag/AgCl. We measured the external quantum efficiency (EQE) spectra of these Cu_2O electrodes at -0.4 V vs. Ag/AgCl, at which a band bending of about 0.2 eV is expected. The EQE spectra show an onset at about 650 nm and a steep rise at about 520 nm, as shown in Figure 5. Since Cu_2O has a direct allowed transitions at wavelengths shorter than 520 nm and a direct forbidden transition at wavelengths shorter than 650 nm [20, 21], the observed spectral responses would reflect the photoabsorption properties of the compound.

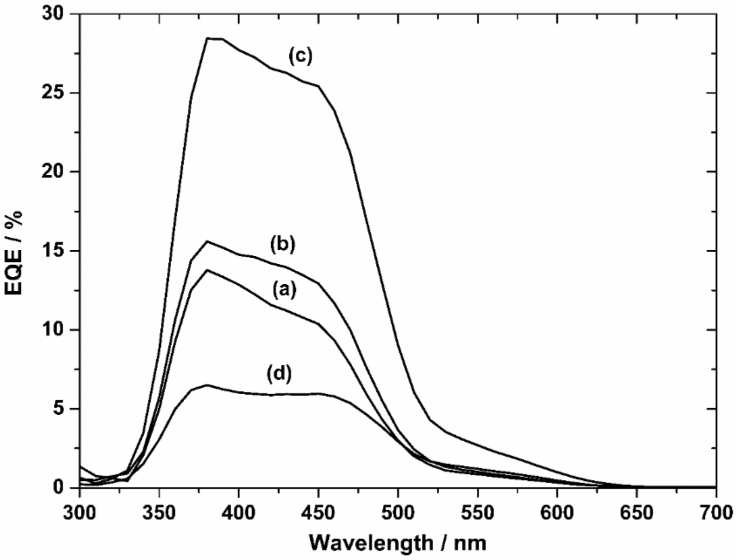

Figure 5. External quantum efficiency (EQE) spectra of Cu_2O films prepared at (a) -0.5 V, (b) -0.55 V, (c) -0.6 V, and (d) -0.65 V vs. Ag/AgCl. These spectra were obtained at the applied potential of -0.4 V vs. Ag/AgCl in 0.5 M Na_2SO_4 under O_2 bubbling.

As shown in Fig. 5c, the highest EQE was obtained from the film deposited at an applied potential of -0.6 V vs. Ag/AgCl, with 28% EQE at a wavelength of 375 nm (Fig. 5c). As shown in the above XPS results, the Cu_2O films deposited at applied potentials of -0.50 V and -0.55 V vs. Ag/AgCl contain relatively larger amounts of Cu^{2+} impurities than the film deposited at a potential -0.60 V vs. Ag/AgCl, as seen from the slightly higher Cu^{2+} peak intensities. Hence, the lower EQEs of the films deposited at -0.50 V and -0.55 V vs. Ag/AgCl are probably due to the inclusion of Cu^{2+} impurities in the films at higher concentrations. In the case of the Cu_2O film deposited at applied potential of -0.65 V vs. Ag/AgCl, the inclusion of metallic Cu components may result in the low EQE (Fig. 5d).

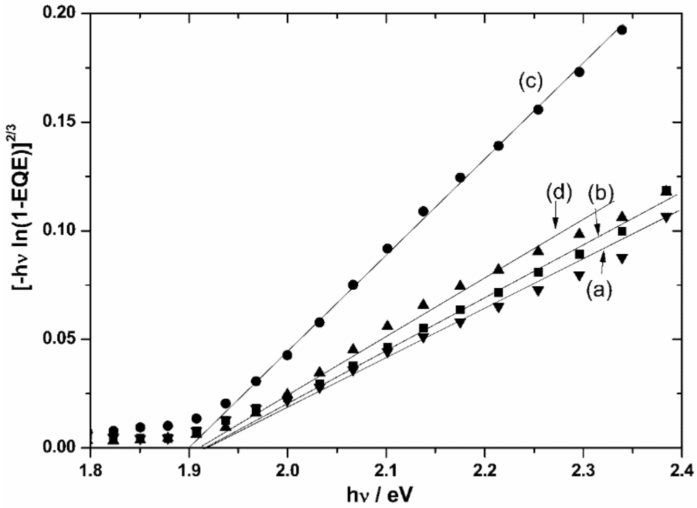

Figure 6. Plots of [-hν ln (1-EQE)]$^{2/3}$ vs. hν (eV) for Cu_2O films prepared at (a) -0.5 V, (b) -0.55 V, (c) -0.6 V, and (d) -0.65 V vs. Ag/AgCl. Intercept lines denote E_g values.

The band gap (E_g) of the Cu_2O films can be determined from analysis of the absorption spectra and also from the EQE spectra of the films near the onset regions. According to Gartner's treatment [22], EQE can be described by the following equation:

$$\mathrm{EQE} = 1 - \frac{\exp(-\alpha W)}{1+\alpha L_n}, \tag{4.1.1}$$

where α is the absorption coefficient of the material, W is the width of the space charge region, and L_n is the minority carrier diffusion length. It is reasonable to assume small L_n (αL_n<<1) for the Cu_2O films deposited by electrochemistry. Hence, the equation is converted to eq. (4.1.2).

$$\mathrm{EQE} = 1 - \exp(-\alpha W). \tag{4.1.2}$$

The absorption coefficient of a material as a function of photon energy is given by

$$\alpha = \frac{A(\mathrm{h}\nu\text{-}E_g)^n}{\mathrm{h}\nu}, \tag{4.1.3}$$

where A is a constant, hν is the photon energy, and n is a constant depending on the probability of transition; the values are 1/2, 3/2, 2 and 3 for direct allowed, direct forbidden, indirect allowed and indirect forbidden transition gaps, respectively. Since the transition of Cu_2O near the onset is direct forbidden (see above), n of 1.5 is applied. By substituting equation (4.1.3) into equation (4.1.2), EQE can be related to E_g by the following equation:

$$[-h\nu \ln (1-\mathrm{EQE})]^{2/3} = h\nu - E_g. \qquad (4.1.4)$$

Figure 6 shows plots of $[-h\nu \ln (1-\mathrm{EQE})]^{2/3}$ against hν for the Cu_2O films. From the intercepts of the photon energy (hν) axis, E_g of these films was determined be about 1.9±0.02 eV.

To complete the heterojunction solar cells, Al:ZnO films with a thickness of about 200 nm were sputtered on the Cu_2O films. Figure 7 shows the current density-voltage (J-V) curves for the glass/FTO/Cu_2O/ Al:ZnO devices under simulated AM 1.5 irradiation (100 mW cm^{-2}). The devices were irradiated through the AZO films because more photons can be absorbed by the Cu_2O layer near the Cu_2O/ Al:ZnO junction, which produced larger photocurrents. The glass/FTO/Cu_2O/ Al:ZnO device based on the Cu_2O film deposited at -0.50 V vs. Ag/AgCl shows no rectification behavior: it gave almost a linear J-V plot with a steep slope (Fig. 7a). The existence of voids between the relatively large Cu_2O grains in the film (see Fig. 2a) caused direct contact between the back and front electrodes, leading to the observed significant leakage. Note that in the case of the photoelectrochemical measurements as shown in Fig. 5, the leakage becomes less significant because the transport of chemicals (O_2 in the case of our experiments) through narrow voids is a slow process. The other glass/FTO/Cu_2O/ Al:ZnO devices based on Cu_2O films deposited at potentials more negative than - 0.50 V vs. Ag/AgCl showed solar cell properties.

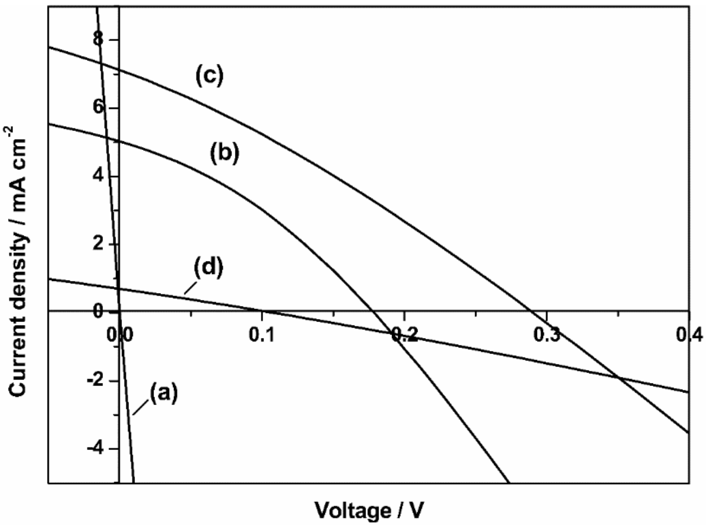

Figure 7. *J*-*V* characteristics of glass/FTO/Cu_2O/ Al:ZnO cells made from Cu_2O films electrodeposited at (a) -0.5 V, (b) -0.55 V, (c) -0.6 V, and (d) -0.65 V vs. Ag/AgCl.

The highest energy conversion efficiency of 0.603% was obtained with the Cu_2O film deposited at a potential of -0.60 V vs. Ag/AgCl, as shown in Fig. 7c: J_{SC} was 7.12 mA cm^{-2}, V_{OC} was 0.29 V, and fill factor (*FF*) was 0.292. Relatively good compactness of the film and small inclusion of Cu^{2+} in the film, as discussed above, are responsible for the good properties. From the *J*-*V* plot of the best solar cell in this study (see Fig. 7c), shunt resistance (R_{sh}) and series resistance (R_s) of the cell were determined to be 514 Ω and 210.6 Ω, respectively [23]. The low R_{sh} in our cell resulted in low V_{OC} and *FF*. Even though the Cu_2O in this device has better compactness and flatness than those obtained at different potentials (see Fig. 2), the results imply the presence of pinholes in this film. Mechanical damage that occurred during sputtering of the upper Al:ZnO film might also cause defects contributing to the leakage current. The high R_s of our device, which was probably due to the small grain size of Cu_2O crystallites, also resulted in decrease in *FF*.

The device based on the Cu_2O film deposited at a more negative potential of -0.65 V vs. Ag/AgCl was largely resistive and showed leakage current, resulting in very low solar cell performance (Fig. 7d). The large resistivity and the leakage of the device are attributed to the less crystalline nature of the film and the formation of lumps of metallic Cu on the Cu_2O film (Fig. 3d).

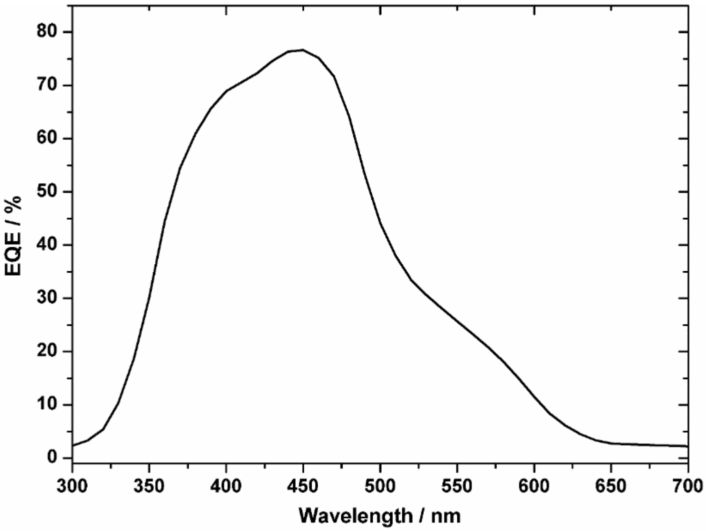

Figure 8. An EQE spectrum of the glass/FTO/Cu_2O/ Al:ZnO cell made from a Cu_2O film deposited at -0.6 V vs. Ag/AgCl.

To further study the properties of our best device made of the Cu_2O film deposited at -0.60 V (vs. Ag/AgCl), its EQE spectrum was measured. The onset of EQE is about 650 nm, which is consistent with the band gap of 1.9 eV. The EQE reaches a maximum value (ca. 75%) at 450 nm, as shown in Fig. 8. An appreciable shoulder observed at wavelength between 520 nm and 650 nm was due to the direct forbidden transition nature of Cu_2O (see above). The higher EQE and the stronger shoulder were observed in this measurement than those obtained in the photoelectrocemical measurement using the Cu_2O film deposited under the same conditions (see Fig. 5c). This is due to the difference in the band bending: magnitudes of band bending of about 0.2 eV and 1.0 eV are expected for the photoelectrochemical (based on the photocurrent onset) and photovoltaic measurements (assuming an ideal case for Cu_2O/ZnO junction [24]), respectively. The difference in the band bending leads to the different *W* for the two measurements.

It is useful to determine *W* at the short circuit condition to analyze the fundamental features of the device made of the electrochemically deposited Cu_2O films. The *W* value can be correlated to EQE by taking logarithms of eq. (4.1.2),

$$-\ln(1-\mathrm{EQE}) = \alpha W. \qquad (4.1.5)$$

Using this equation, W can be experimentally estimated from the slope of the –ln(1-EQE) versus α plots, where α values are determined from the absorption spectrum of the Cu_2O film (see the inset of Fig. 9). The slope of Fig. 9 gives the *W* value of 0.28 μm. This in turn gives the acceptor concentration of 1.07×10^{16} cm^{-3}, assuming the band bending of 1 eV and dielectric constant of 7.6 [25]. The *W* value of our device suggests that the observed low V_{oc} of about 0.29 V is not due to the insufficient thickness of the Cu_2O film but due to the current leakage through the film

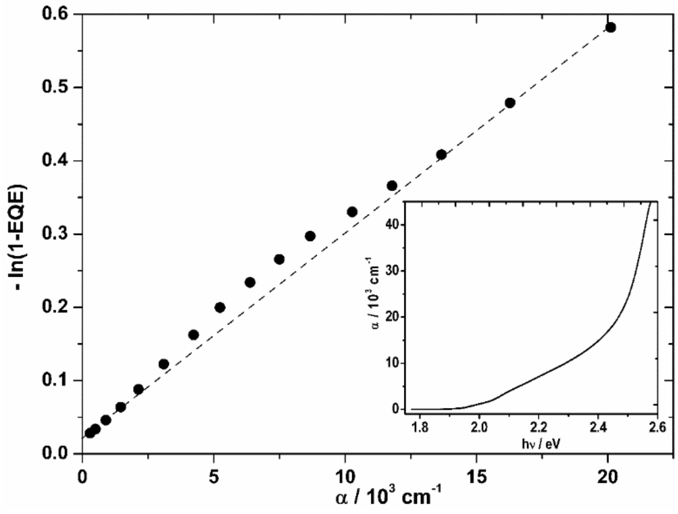

Figure 9. Plot of -ln(1-EQE) vs. α of the Cu_2O film electrodeposited at -0.6 V vs. Ag/AgCl. Inset shows plot of α vs. hν of the film obtained from its photoabsorption property and film thickness (1.6 μm).

To further confirm the above conclusion, we prepared devices with different Cu_2O thicknesses of 0.8, 1.6, 2.3, and 3.2 μm. The films were deposited on FTO substrates at -0.6 V vs. Ag/AgCl by changing the deposition time: the charges passed during the deposition were 0.7, 1.4, 2.0, and 2.8 C cm^{-2}. The device with a 1.6 μm-thick Cu_2O film showed the highest efficiency. The device with a 0.8 μm-thick film showed considerable leakage current, and the devices with 2.3 μm-thick and 3.2 μm-thick films showed lower FF and lower J_{sc} due to large R_s. The devices with the Cu_2O films of 2.3 and 3.2 μm showed nearly the same V_{oc}. Concerning the space charge region developed in the Cu_2O layer, W of 0.28 μm was estimated under the short-circuit condition, as discussed above. This W is smaller than the thicknesses and the optical absorption depth (α^{-1}) of the Cu_2O film: α^{-1} is 0.46 μm at a wavelength of 500 nm.

From the facts and insights described above, the solar cell properties of the present device will be improved by various modifications, e.g., increase in W by decreasing the acceptor concentration, increase in Cu_2O grain sizes while maintaining film thickness homogeneity to reduce the internal resistivity of the Cu_2O film, and insertion of a thin buffer layer before the deposition of Al:ZnO to suppress cell leakage. Since the quality of the electrodeposited Cu_2O film is highly dependent on the deposition parameters such as deposition potential, temperature and electrolyte composition, increase in the efficiency of the devices is expectable by optimizing these parameters and controlling the conditions precisely.

4.1.4. Conclusion

A Cu_2O/AZO heterojunction was fabricated by electrodeposition of a Cu_2O film on an FTO glass substrate in a potentiostatic regime followed by sputtering of an AZO film. The heterojunction obtained from the Cu_2O film deposited at -0.6V (vs Ag/AgCl) showed good electrical rectification and the best solar cell performance with 0.60% conversion efficiency. We found that the morphologies and phase purities of the Cu_2O films are highly dependent on the electrodeposition potential; thus strongly affect the photovoltaic properties. Although the Cu_2O/AZO heterojunction is a highly promising combination for a scalable production of solar cells, achievement of high conversion efficiency is still a bottleneck. The present device film possesses a high series resistance and a low shunt resistance derived from various faults of the Cu_2O film and the interface between the Cu_2O and AZO films..

References

[1] G. P. Pollack, D. Trivich, J. Appl. Phys., 46 (1975) 163-172.

[2] L. C. Olsen, F. W. Addis, W. Miller, Sol. Cell., 7 (1982) 247-279.

[3] E. Fortin, D. Masson, Solid State Electron., 25 (1982) 281-283.

[4] R. J. Iwanowski, D. Trivich, Phys. Status Solidi A 95 (1986) 735-741.

[5] K. Akimoto, S. Ishizuka, M. Yanagita, Y. Nawa, G. K. Paul, T. Sakurai, Solar Energy 80 (2006) 715-722.

[6] J. Herion, E. A. Niekisch, G. Scharl, Sol. Energy Mater., 4 (1980) 101-112.

[7] T. Minami, H. Tanaka, T. Shimakawa, T. Miyata, and H. Sato, Jpn. J. Appl. Phys., Part 2 43A, L917, (2004).

[8] Y. Nishi, T. Miyata, T. Minami, Thin Solid Films, 528 (2013) 72-76.

[9] T. Minami, T. Miyata, K. Ihara,Y. Minamino, S. Tsukada, Thin Solid Films 494 (2006) 47-52.

[10] M. Izaki, K. Mizuno, T. Shinagawa, M. Inaba, A. Tasaka, J. Electrochem. Soc., 153 (2006) C668-C672.

[11] J. Katayama, K. Ito, M. Matsuoka, J. Tamaki, J. Appl. Electrochem. 34 (2004) 687.

[12] M. Izaki, T. Shinagawa, K. Mizuno, Y. Ida, M. Inaba, A. Tasaka, J. Phys.D: Appl. Phys. 40 (2007) 3326.

[13] S. S. Jeong, A. Mittiga, E. Salza, A. Masci, S. Passerini, Electrochim. Acta, 53 (2008) 2226-2231.

[14] T. D. Golden, M.G. Shumsky, Y. Zhou, R.A. VanderWerf, R.A. Van Leeuwen, and J. A. Switzer, Chem. Mater., 8 (1996) 2499-2504.

[15] Y. Zhuo and J.A. Switzer, Scripta Mater., 38 (1998) 1731-1738.

[16] T. Mahalingam, J. S. P. Chitra, J. P. Chu, S. Velumani, P. J. Sebastian, Sol. Energy Mater. Sol. Cell., 88 (2005) 209-216.

[17] L. C. Wang, N. R. de Tacconi, C. R. Chenthamarakshan, K. Rajeshwar, and M. Tao, Thin Solid Films, 515 (2007) 3090-3095.

[18] P. E. Larson, J. Electron. Spectrosc. Relat. Phenom. 4 (1974) 213-218.

[19] N. S. Mclntyre, M. G. Cook, Analy. Chem. 47 (1975) 2206-2213.

[20] H. Amekura, N. Umeda, Y. Takeda, and N. Kishimoto, Appl. Phys. Lett., 89 (2006) 223120.

[21] P. E. de Jongh, D. Vanmaekelberg, J. J. Kelly, Chem. Mater., 11 (1999) 3512-3517.

[22] W. W. Gartner, Physical Review, 116 (1959) 84.

[23] K.-I. Ishibashi, Y. Kimura, M. Niwano, J. Appl. Phys. 103 (2008) 094507.

[24] S. Ishizuka, K. Suzuki, Y. Okamoto, M. Yanagita, T. Sakurai, K. Akimoto, N. Fujiwara, H. Kobayashi, K. Matsubara, S. Niki, Phys. Stat. Sol. C, 4 (2004) 1067-1070.

[25] E. C. Heltemes, Phys. Rev. 141 (1966) 203.

4.2. An Inorganic/Organic Hybrid Solar Cell Consisting of Cu_2O and a Fullerene Derivative

4.2.1. Introduction

It is expected that the production cost of solar cells can be reduced if thin-film solar cells are fabricated without using sophisticated processes. Organic solar cells are attracting attention because of their potential low-cost production due to ease in producing large-area and flexible devices by wet processes such as printing [1,2]. A typical organic solar cell is made of an electron-donating conducting polymer, such as polythiophene, and a derivative of fullerene (C_{60}) that is a good electron acceptor. Photoactive layers of those solar cells are produced by spin-coating from a solution containing these materials. The photoactive layers are mostly designed to have a bulk-heterojunction architecture that consists of interpenetrating networks of the electron donor and the electron acceptor [3-5]. Irradiation of these organic solar cells results in the formation of a spatially localized electron-hole pairs, i.e. Frenkel-type excitons, which have a relatively large binding energy in th eorder of 0.5 eV. Hence, the separation of carriers from Frenkel-type excitons at a donor/acceptor interface is essential for organic solar cells, which means that a large interfacial area and good contact between the electron donor and acceptor are important [6,7]. This sometimes makes reproducible fabrication of high-quality layers difficult.

In the case of inorganic semiconductors, free charge carriers are generated upon irradiation. Inorganic semiconductors are advantageous over organic materials in chemical stability and mobility of charge carriers. Some inorganic semiconductors can be produced by low-cost processes such as close-space sublimation, sol-gel deposition, and electrodeposition [8-10].These semiconductors include p-type materials such as CdTe and Cu_2O as well as n-type materials such as CdSe, TiO_2 and ZnO. Using Cu_2O, fairly high efficiency is expected, although its band gap (1.9 –2.1eV) is larger than the optimal energy gapfor solar cells (1.4 eV). Another advantage of Cu_2O is that it is made of nontoxic and abundant elements. In addition, Cu_2O films can be deposited electrochemically from an aqueous solution containing Cu^{2+} ions. Highest efficiency of 4.12% has been reported for a solar cell with a junction of p-Cu_2O and n-ZnO [11].However, in that study, the ZnO layer was deposited on the Cu_2O layer by using a vacuum technique. Non-vacuum deposition techniques such as electrodeposition and photochemical deposition have been investigated for fabrication of a p/n junction [12,13].However, formation of a p/n junction with high quality by these methods is difficult. Although ZnO has been used as an n-type semiconductor for thefabrication of a p/n junction with Cu_2O [14-16], inherent defects (oxygen vacancies/zinc interstitial)often pose problems. It is therefore, important to develop a method for fabricating a good p/n junction with Cu_2O using an n-type semiconductor that can be deposited by a non-vacuum process.

To achieve the above goal, we have studied the formation of a p/n junction with Cu_2O using [6,6]-phenyl-C_{61}-butyric acid methyl ester (PCBM), which is a derivative of fullerene (C60). The advantages of using the organic material lie in its good electronic accepting properties and simple film formation using a spin-coating method, which is an economical and scalable method compared to vacuum evaporation techniques [17,18].Similar to our approach, Oku et al. proposed fullerene (C_{60}) as an n-type material for the formation of a p/n junction with Cu_2O [19].They tried to make the C_{60} layer by different methods including spin coating. However, the highest efficiency they achieved was less than 0.005%. This low efficiency is probably due to the difficulty in making uniform films of C_{60} that is insoluble in solvents. Recently, Hung et al.[20] made a good Cu_2O/PCBM junction on a Cu_2O layer made of hollow nanoparticles. In these devices, the fullerene compounds (C_{60} and PCBM) are supposed to form a p/n junction with Cu_2O, and electrons photogenerated in the Cu_2O layer are expected to be transferred to the fullerene layer, which is a good electron conductor.

Herein we report a solar cell with a Cu_2O/PCBM junction formed on an electrochemically deposited Cu_2O layer. The use of PCBM is expected to be suitable for making a homogeneous layer on the Cu_2O layer, which usually has a rough surface. Optimization of the electrochemical deposition of Cu_2O layers is also expected to contribute to an increase in efficiency [21]. The solar cell properties were studied by changing the conditions of electrochemical deposition of the Cu_2O layer and post-annealing.

4.2.2. Experimental

Solar cells with a structure as shown in Fig. 1 were fabricated on indium-tin-oxide (ITO) glass substrates (resistivity of 15Ω/sq, Asahi Glass Co.). The substrates were cleaned by immersing in boiling de-ionized waterand sonicating in acetone for 30 min each and then exposed to oxygen (O_2) plasma(40 W, 7.5×10^{-5} Pa) for15 min. ACu_2O layer was electrodeposited on an ITO-coated glass substrate with a three-electrode system using Ag/AgCl as a reference electrode, a copper sheet as a counter electrode, and the ITO-coated glass substrate as a working electrode. The electrolyte consisted of 0.2 M $CuSO_4$ and 3M lactic acid. The pH of the solution was adjusted to 12.5 by addition of NaOH. The temperature of the electrodeposition bathwas kept at about 55-60°C. The thickness of the Cu_2O film was controlled in a range from 500 to 900 nm by changing the time of electrodeposition. After depositing a Cu_2O layer,annealing was carried out at 120°C for 30 min in low vacuum (about 10 Pa) to remove moisture from the films. Details of the electrodeposition of Cu_2O layers were reported elsewhere [21]. On the Cu_2O layer, a PCBM(Aldrich, 95.5% purity)layer was spin-casted from a 10 mg/mL solution in chloroform at 850 rpm for 30 s, which are in the range of standard conditions for coating aPCBM layer of organic solar cells and other electronic devices [22, 23].

By depositing an Al electrode on the stacked Cu_2O/PCBM layers, a solar cell having an active area of 0.02 cm^2 was fabricated. Then the device was post-annealed in air at 90°C for 15 min to improve the quality of interfaces included in the devices.

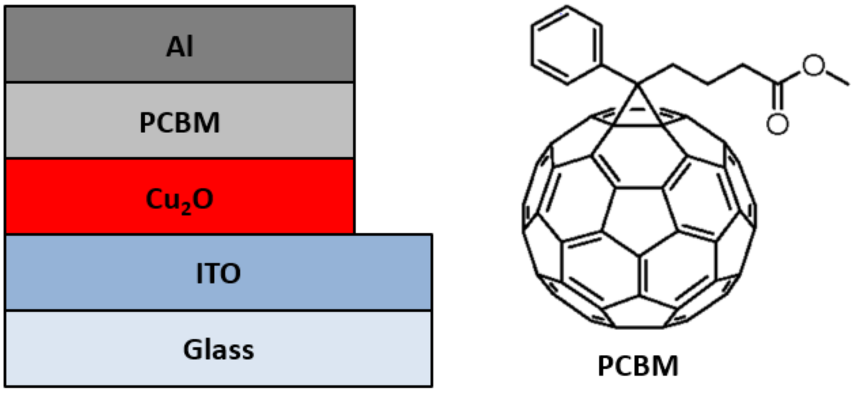

Figure. 1. A schematic of a solar cell fabricated in this study and a molecular structure of PCBM.

Current–voltage (*J*-*V*) characteristics of the solar cells were measured at room temperature in air with a photovoltaic measurement system (Bunko keiki CEP-015) under a simulated AM 1.5G (100mW/cm^2)condition. Crystal structure and phase composition of the p-type Cu_2O films were determined by X-ray diffraction (XRD) analysis using an X-ray diffractometer (RigakuMiniFlex)with a theta /2 theta configuration usingNi-filtered CuKα radiation (λ = 0.15418 nm, 30 kV, 15 mA). Ultraviolet/visible (UV-vis) absorption spectra were obtained witha spectrometer (Hitachi U-4100). Scanning electron micrography (SEM) was conducted using a field-emission type scanning electron microscope (Hitachi S-5000 FEG) with an acceleration voltage of 2 kV. The average thicknesses of the films were determined from the cross sectional views of the SEM images.

4.2.3. Results and discussion

Cu_2O films were electrochemically grown on patterned ITO glass substrates from an electrolyte consisting of 0.2 M $CuSO_4$ and 3M lactic acid at an optimized voltage of -0.6V[23]. After processing at this potential for3 min, 5 min and 6 min, layers with thicknesses of about 500 nm, 700 nm and 900 nm, respectively, were deposited. The films were heated at 120°C for 30 min under low vacuum (about 10 Pa) to remove moisture from the films. This heating process did not affect the XRD pattern or the UV-vis spectra of the films. XRD patterns of the films thus obtained showed narrow peak widths as can be seen in Fig. 2, indicating that the Cu_2O grains are made of well-developed crystals. The grains were more oriented in the (111) direction for all the films, and this tendency became weaker as the Cu_2O layer became thicker.

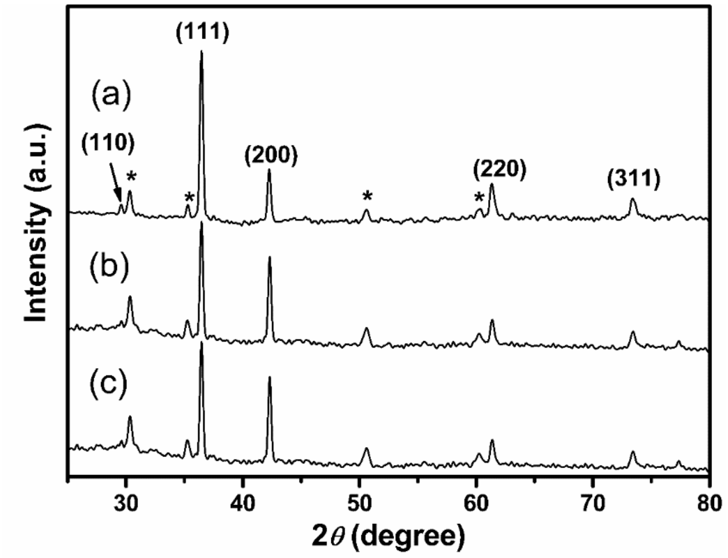

Figure. 2. XRD patterns of Cu_2O layers with various thicknesses: (a) 500 nm, (b) 700 nm, and (c) 900 nm. Asterisks denote diffraction peaks from the ITO substrate.

In this study, we used Cu_2O layers deposited at a potential of -0.6 V vsAg/AgCl because those Cu_2O films showed the optimal properties as a p-type semiconductor for solar cells [21].

On the top of the Cu_2O film, a PCBM layer was deposited by spin-casting chloroform solution containing PCBM at a concentration of 10 mg/mL. Cross-sectionalSEM images of typical samples with and without a PCBM layer areshown in Fig.3. The SEM images show that the Cu_2O layers deposited at -0.6 V consist of closely-packed grains with a size of about 500 nm. However, the surface of the Cu_2O layers was rather rough due to the morphology of the grains. When the chloroform solution containing the PCBM layer was spin-casted on the Cu_2O layer, a film of PCBM with a thickness of about 100 nm was deposited. The surface of the stacked films became flatter than the surface of the Cu_2O layer. In addition, there were no voids at the Cu_2O/PCBM interface, as can be seen in Fig. 3b. We consider these are the advantages of making ap/n junction on a Cu_2O layer by spin-coating a PCBM layer.

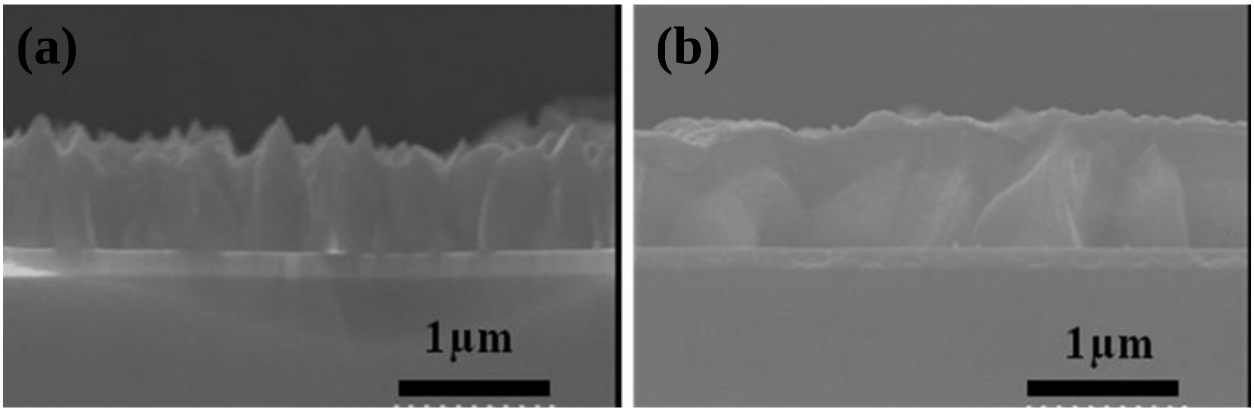

Figure. 3. Cross-sectional SEM images of (a) a Cu_2O film with a thickness of about 900 nm and (b) a stack of Cu_2O/PCBM films after post-annealing at 90 °C. The PCBM layer on the Cu_2O film is about 100 nm thick.

Figure 4 shows UV-vis spectra of a Cu_2O film, a PCBM film, and a stack of Cu_2O/PCBM film. The Cu_2O and stacked films show strong photoabsorption over the wavelengths up to 630 nm (1.96eV), which corresponds to the band gap of Cu_2O. In addition to this strong photoabsorption, weak photoabsorption cotinues to about 700 nm, which may be due to the inclusion of a small amount of CuO in the electrochemically deposited Cu_2O films. The inclusion can occur because the potential range for the formation of Cu_2O is as narrow as 0.15 V in the phase diagram [24].

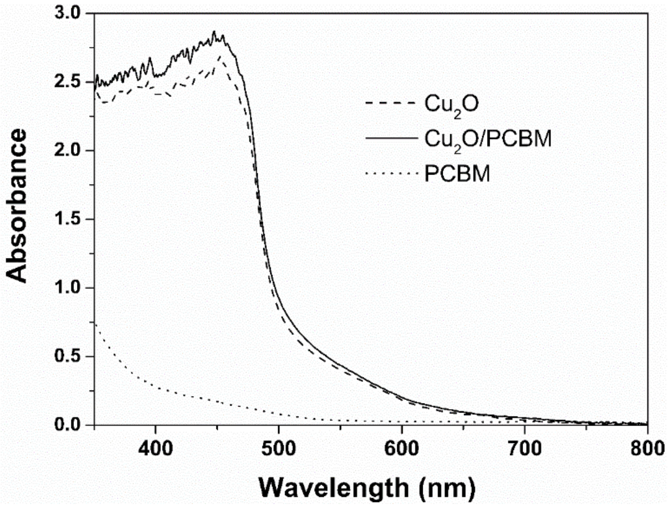

Figure. 4. UV-vis spectra of a PCBM film (broken line) and a stack of Cu_2O/PCBM films (solid line). The Cu_2O film was about 700 nm thick and the PCBM film was about 100 nm thick. The absorption is saturated at wavelengths shorter than 470 nm due to inhomogeneousness of the Cu_2O film.

By depositing a PCBM layer and an Al layer sequentially in this order on the Cu_2O layer, solar cell devices with a structure of glass/ITO/Cu_2O/PCBM/Al were prepared. The devices were post-annealed at 90°C for 15 min in air, which means that the device was annealed after loading the Al electrode. This annealing was effective to increase the photocurrent density by about 50%. Very similar increase in photocurrent was observed when the Al electrode was deposited on the Cu_2O/PCBM stacked layers that had been annealed under the same conditions. Hence, we assume that the improvement is due to the increased contact area at the Cu_2O/PCBM interface, although we were unable to observe morphological changes in SEM images by the annealing. Solar cell devices were prepared by changing the thickness of the Cu_2O layer, keeping all other conditions the same. Figure 5 showscurrent density-voltage (J-V) characteristics of deviceshaving Cu_2O films with thicknesses of about 500, 700, and 900 nm. Performances of the solar cells, i.e. short-circuit photocurrent density (J_{SC}), open-circuit voltage (V_{OC}), fill factor (FF), and efficiency, are summarized in Table 1. Of the three kinds of devices, the device having a 700nm-thick Cu_2O layer exhibited the highest efficiency of 0.095% mostly because of the highest J_{sc} of 1.50 mA/cm^2. On the other hand, devices using Cu_2O layers with thicknesses of500 nm and 900 nm showed lower efficiencies of 0.045% and 0.055%with J_{SC} of 0.67 and 0.80mA/cm^2, respectively. The lowered current density for the device with a 900 nm-thick Cu_2O layer is attributed to the increased internal filtering effect, which lowers the photoabsorption by Cu_2O near the Cu_2O/PCBM interface. On the other hand, the low current density for the device with a 500 nm-thick Cu_2O layer is attributed to the poor quality of Cu_2O in a shallow region near the substrate. Incidentally, for devices with a Cu_2O/Al:ZnO junction, the solar cell properties improved by increasing the thickness of the Cu_2O layer to the level of about 1,600 nm, although the photoactive region was estimated to be about 280 nm thick from the junction[21]. The Cu_2O layer of this type of device was photoirradiated through the Al:ZnO layer;it was photoirradiated from the far side from the substrate.

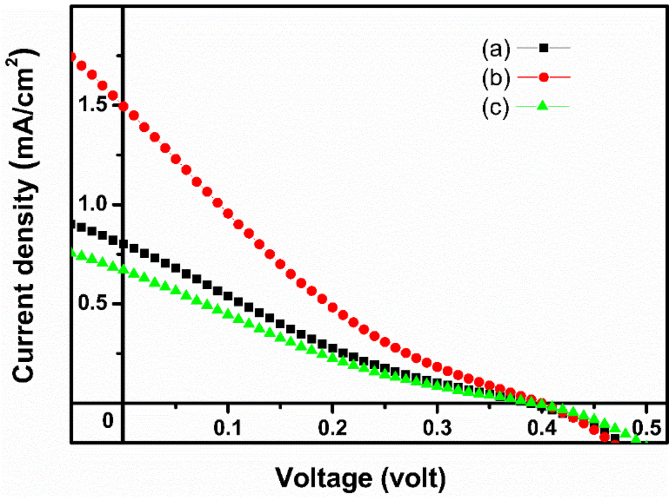

Figure. 5. Current density-voltage characteristics of the devices having a Cu_2O/PCBM junction. Thicknesses of the Cu_2O layer were (a) 500 nm, (b) 700 nm, and (c) 900 nm.

Table 1. Performances of 3 kinds of solar cells with a structure of glass/ITO/Cu_2O/PCBM/Al under AM 1.5G (100 mW/cm^2) irradiation. Thicknesses of the Cu_2O layer are (a) 500 nm, (b)700 nm, and (c) 900 nm.

Cu_2O thickness	J_{SC} / mA cm^{-2}	V_{OC} / V	*FF*	Efficiency / %
(a) 500 nm	0.67	0.40	0.17	0.045
(b) 700 nm	1.50	0.40	0.16	0.095
(c) 900 nm	0.80	0.39	0.17	0.055

All of these devices showed *FF* of about 0.16. This low *FF* together with low J_{sc} of the devices suggests buildup of charges in the Cu_2O layer due to inefficient charge carrier extraction. On the other hand, the present Cu_2O/PCBM heterojunction cell showed higher V_{oc}than that of our previous Cu_2O/ Al:ZnO junction cell [21]. This suggests that PCBM can be deposited without causing damage to the Cu_2O film.

Figure 6 shows the external quantum efficiency (EQE) spectrum of the solar cell with a 700nm-thick Cu_2O layer, which showed the highest solar cell efficiency. The low EQE values at wavelengths shorter than 500 nm indicate that the filter effect due to the internal photoabsorption by the Cu_2O film is responsible for the low photocurrent densities of our samples; see the absorption spectrum shown in Fig. 4. In addition, the poor quality of Cu_2O in the region near the substrate impedesthe photocurrent generation by the carriers photogenerated in this region. This also lowers EQE at short wavelengths. The relatively high EQE values around 600 nm, at which the absorbance of the Cu_2O film was about 0.18 as seen in Fig. 2, is partly attributed to the increased optical length due to reflection of light at the PCBM/Al interface. Small photocurrents are generated at wavelengths longer than 650 nm. Sinceintrinsic Cu_2O does not photoabsorb in this wavelength region, the photocurrents should be related tothe unique photoabsorption of the Cu_2O film deposited by electrochemistry. The origin of thephotoabsorption is not clear yet, but it might be related to the CuO component included in the Cu_2O film as discussed above.

From the overlap of the EQE spectrum shown in Fig. 6 and the AM1.5G spectrum (100 mW/cm^2) [25], a photocurrent density of 2.5 mA/cm^2 is estimated. The observed J_{SC} values are lower than this value as shown in Table 1, indicating that the electron-hole recombination is enhanced under strong irradiation.

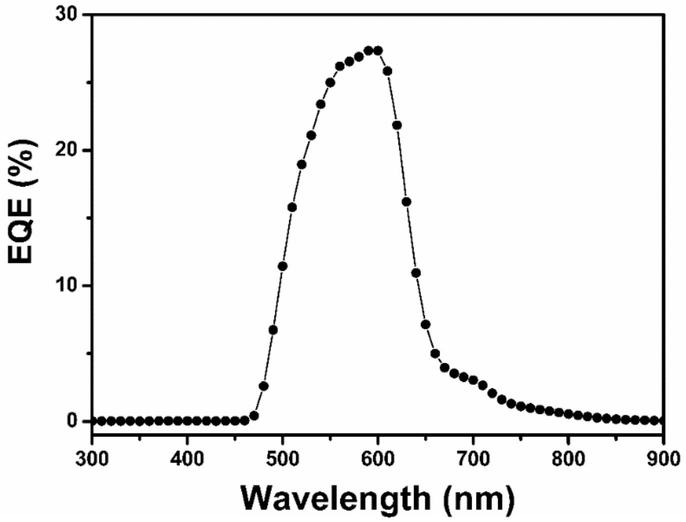

Figure. 6. A spectrum of external quantum efficiency of an ITO/Cu_2O(700 nm)/PCBM/Al solar cell.

The results obtained in the present study suggest that the Cu_2O/PCBM junction is effective for making solar cells. The results also suggest that increase in the mobility and lifetime of electrons in the Cu_2O films is important for increasing solar cell efficiency. It may be possible to increase the photocurrent and the efficiency by introducing an interpenetrated structure at the Cu_2O/PCBM interface, which is sometimes used in organic solar cells [26, 27]. The structure can be prepared by roughening the Cu_2O/PCBM interface using a Cu_2O film consisting of more protruded Cu_2O grains. Although the fundamental properties of the solar cells need to be improved for practical applications, the results are promising concerning the use of the Cu_2O/PCBM junction in solar cells.

4.2.4. Conclusion

We fabricated an inorganic/organic hybrid solar cell with a Cu_2O/PCBM junction using wet processes, i.e. electrochemical deposition and spin coating. The highest efficiency of the solar cell was only 0.095%. We expect that efficiency will be increased by improving the mobility and lifetime of electrons in the Cu_2O film and/or introducing an interpenetrated Cu_2O/PCBM interfacial structure into the device.

References

[1]G. Li, V. Shrotriya, J. Huang, Y. Yao, T. Moriarty, K. Emery, and Y. Yang, Nat. Mater.4 (2005) 864.

[2]H. Hoppe, M. Niggemann, C. Winder, J. Kraut, R. Hiesgen, A. Hinsch, D. Meissner, and N. S. Sariciftci, Adv.Funct. Mater.14 (2004) 1005.

[3]F. Yang, M. Shtein, and S. R. Forrest, Nat. Mater.4(2005)37.

[4]Z. Zhou, X. Chen,and S. Holdcroff,J. Am. Chem. Soc.130(2008)11711.

[5]A. J. Moule and K. Meerholz, Adv. Mater.20(2008)240.

[6]Y. Kim, S. Cook, S.M. Tuladhar, S. A. Choulis, J. Nelson, J. R. Durrant, D. C. Bradley, M. Giles, I. McCulloch, C. S. Ha, and M. Ree, Nat. Mater.5(2006)197.

[7]D. C. Coffey, O. G. Reid, D. B. Rodovsky, G. P. Bartholomew, and D. S. Ginger, Nano Lett.7(2007)738.

[8]W.U. Huynh, J. J. Dittmer, and A.P. Alivisatos,Science 295(2002)2425.

[9]C. Y. Kuo, W. C. Tang, C. Gau, T. F. Guo, and D. Z.Jeng,Appl. Phys. Lett.93 (2008)033307.

[10]W. J. E. Beek, M. M. Wienk, and R. A. J. Janssen,Adv. Mater.16(2004)1009.

[11] Y. Nishi, T. Miyata, T. Minami, Thin Solid Films, 528 (2013) 72-76.

[12]M. Izaki, T. Shinagawa, K. Mizuno, Y. Ida, M. Inaba, and A. Tasaka, J. Phys. D: Appl. Phys.40(2007)3326.

[13]M. Izaki, K. Mizuno, T. Shinagawa, M. Inaba, and A. Tasaka,J. Electrochem. Soc.153

(2006) C668.

[14]A. Mittiga, E. Salza, F. Sarto, M. Tucci, R. Vasanthi, Appl. Phys. Lett.88 (2006) 163502.

[15]T. Minami, T. Miyata, K. Ihara,Y. Minamino, S. Tsukada, Thin Solid Films 494 (2006) 47.

[16]J. Katayama, K. Ito, M. Matsuoka, J. Tamaki,J. Appl. Electrochem.34(2004) 687.

[17]G. Yu, and A. J. Heeger, J. Appl. Phys.78 (1995)4510.

[18]F. Padinger, R. S. Rittberger, and N. S. Sariciftci,Adv. Funct. Mater.13(2003)85.

[19]T. Oku, R. Motoyoshi, K. Fujimoto, T. Akiyama, B. Jeyadevan, J. Cuya,J. Phys. Chem. Solids72(2011)1206.

[20]L.-I. Hung, C.-K. Tsung, W. Huang, and P. Yang, Adv. Mater.22 (2010)1910.

[21]W. Septina, S. Ikeda, M. A.Khan,T. Hirai, T. Harada, M. Matsumura, and L. M. Peter,Electrochim. Acta56(2011)4882.

[22] A. Tada, Y. Geng, Q. Wei, K. Hashimoto, and K. Tajima, Nature Mater.10 (2011) 450.

[23] T. Morita, V. Singh, S. Oku, S. Nagamatsu, W. Takashima, S. Hayase, and K. Kaneto, Jpn. J. Appl. Phys. 49 (2010) 041601.

[24]M. Izaki, M. Nagai, K. Maeda, M. F. B. Mohamad, K. Motomura, J. Sasano, T. Shinagawa, and S. Watase,J. Electrochem. Soc.158 (2011) D578.

[25]ASTM Standard, G-173-03, "Standard Tables for Reference Solar Spectral Irradiance",ASTM International, 1992.

[26]T. Hori, H. Moritou, N. Fukuoka, J. Sakamoto, A. Fujii and M. Ozaki, Materials 3 (2010) 4915.

[27]T. Osasa, S. Yamamoto, and M. Matsumura, Adv. Funct. Mater. 17 (2007) 2937.

General Conclusion

This thesis deals with electrochemical synthesis of p-type semiconductor thin films of CZTSe, CZTS, $CuSbS_2$ and Cu_2O for photovoltaic applications. In general, we demonstrated the successful fabrication of those mentioned semiconductors and their applications in solar cells. The summaries throughout this work are described as follow.

In chapter 2, single–step electrodeposition synthesis of a CZTSe film on a Mo–coated glass substrate from an acidic electrolyte containing Cu(II), Zn(II), Sn(IV), and Se(IV) species was investigated. The desired CZTSe film as main phase was obtained at some selected applied potential ranges through reaction among binary selenides, Cu_2Se, ZnSe and $SnSe_2$, which were continuously formed in the present electrolyte. Sulfurization of the as-deposited film at several temperatures under H_2S gas flow resulted in the formation of mixed compounds of CZTSSe. Although we found appropriate electrodeposition conditions to obtain CZTSSe thin films in the previous research, significant compositional deviations from the optimal composition for photovoltaic application could not be avoided, resulted in difficulty to obtain photovoltaic properties of these thin films. Therefore, a sequential electrodeposition of Cu-Zn-Sn-Se and Cu-Sn-Se layers was applied for fabrication of a CZTSe thin film. Annealing of the bilayer film under argon (Ar) flow induced significant losses of Sn and Se components due probably to evaporation of the SnSe compound. Suppression of these losses could be realized by introduction of Se vapor during the annealing: as a result, a CZTSe thin film with an ideal Cu-poor/Zn-rich composition for solar cell application was obtained. The solar cell with a device with the structure of glass/Mo/CZTSe/CdS/ZnO/Al:ZnO derived from thus-obtained CZTSe film exhibited a conversion efficiency of 1.1%.

In chapter 3, we showed the importance of preheating of the electrodeposited metallic stack composed of Cu, Sn, and Zn layers, and Cu and Sb layers to obtain CZTS and $CuSbS_2$ films with a good compactness, homogeneity and adhesion to the bottom Mo layer. The solar cells with glass/Mo/CZTS or $CuSbS_2$/CdS/Al:ZnO structures derived from the preheated metallic precursors showed the best conversion efficiency of 5.6% and 3.1%, respectively, as opposed of 0.43% and 1.24% from the cells using the CZTS and $CuSbS_2$ without the preheating. In addition, to our knowledge, this is also the first report of the $CuSbS_2$-based solar cell having appreciable solar cell properties.

In chapter 4, electrodeposition synthesis of Cu_2O thin films on glass substrates coated with FTO was studied. The solar cells with a glass/FTO/Cu_2O/Al:ZnO structure were fabricated by sputtering an Al:ZnO film onto the electrodeposited Cu_2O film. The highest efficiency of 0.603% was obtained with a Cu_2O film deposited at -0.6 V (vs. Ag/AgCl). This was attributed to better compactness and purity of the Cu_2O film than those of the Cu_2O films deposited at other potentials. In addition, we fabricated inorganic/organic hybrid solar cells consisting of a p-type Cu_2O layer and a spin-coated fullerene derivative (PCBM) layer. The optimized solar cell showed short circuit current density of 1.5 mA/cm^2, open circuit voltage of 0.4 V, and overall power conversion efficiency of 0.095%. Improvement in mobility and life time of electrons in the Cu_2O layer and/or introducing an interpenetrated Cu_2O/PCBM interfacial structure into the device are considered to be the key to increase efficiency further.

In summary, our results demonstrated the feasibility of electrochemical method to synthesis various semiconductor thin films for photovoltaic applications. We showed various electrodeposition approaches to synthesize the semiconductors: the direct electrodeposition from electrolyte containing all the required elements as demonstrated for the fabrication of Cu_2O and CZTSe, and the electrodeposition of stacked metallic layers as demonstrated for the fabrication of CZTS and $CuSbS_2$. For the fabrication of CZTS(e) and $CuSbS_2$, the approach using electrodeposition of metallic layers precursors allowed more effective control over the compounds' composition compared to the direct electrodeposition, thus, it was easier to fabricate the compounds with composition suitable for photovoltaic applications. In most of the cases, heat treatments at relatively high temperatures were necessary to obtain high crystalline films, except for the fabrication of Cu_2O since the resulted film has sufficient crystallinity even without annealing. Important factors of the materials that determine the solar cell properties are purity, structural compactness, adhesivity to the substrate, and interface quality in the junction. Cu_2O was the simplest to produce, but high purity of the film was a challenge due to high probability of the presence of mixture of Cu^+ and Cu^{2+} components in the electrodeposited films. Hence, it will be the limiting factor as well as the challenge to obtain an appreciable efficiency from the electrodeposited Cu_2O-based solar cell. Moreover, the Cu_2O/Al:ZnO junction had a lower open circuit voltage compared to the Cu_2O/PCBM junction, which suggested that this type of junction is not the ideal one due to the damage by the sputtered Al:ZnO to the Cu_2O film. Optimization of the interface quality by inserting the buffer layer or softer deposition of Al:ZnO can be considered for future research. For the CZTSe, CZTS, and $CuSbS_2$-based solar cells, electrodeposition parameters (eg. applied potential and composition of the electrolyte) and heat treatment condition affect structural and electrical properties of the fabricated materials. Hence, control of these parameters are necessary to obtain the desirable film properties for photovoltaic applications. Promising devices efficiencies obtained using these compounds, eventhough various faults were observed, suggested that much improved solar cell properties can be expected with further optimization of the electrodeposition parameters and heat treatment condition (heating profile, pressure of the S/Se gases). We also expect that the electrodeposition technique can be applied to synthesis other emerging semiconductors thin films for photovoltaic applications, such as $CuBiS_2$, Cu_2SnS_3, SnS, etc.

List of publications

Peer-reviewed publications included in the present thesis:

1. *"Potentiostatic electrodeposition of cuprous oxide thin films for photovoltaic applications"*
   Wilman Septina, Shigeru Ikeda, M. Alam Khan, Takeshi Hirai, Takashi Harada, Michio Matsumura, Laurence M. Peter
   Electrochimica Acta, 56 (2011) 4882-4888.

2. *"An inorganic/organic hybrid solar cell consisting of Cu_2O and a fullerene derivative"*
   M. Alam Khan, Wilman Septina, Shigeru Ikeda, Michio Matsumura
   Thin Solid Films, 526 (2012) 191-194.

3. *"Single-step electrodeposition of a microcrystalline $Cu_2ZnSnSe_4$ thin film with a kesterite structure"*
   Wilman Septina, Shigeru Ikeda, Akio Kyoraiseki, Takashi Harada, Michio Matsumura
   Electrochimica Acta, 88 (2013) 436-442.

4. "*Fabrication of $Cu_2ZnSnSe_4$ thin films from an electrodeposited Cu–Zn–Sn–Se/Cu–Sn–Se bilayer"*
   Wilman Septina, Shigeru Ikeda, Takashi Harada, Michio Matsumura
   physica status solidi (c), in press (2013). DOI: 10.1002/pssc.201200800

5. "*Mechanistic aspect of preheating effects of electrodeposited metallic precursors on structural and photovoltaic properties of Cu_2ZnSnS_4 thin films"*
   Yixin Lin, Shigeru Ikeda, Wilman Septina, Takashi Harada, Michio Matsumura
   Solar Energy Materials and Solar Cells, in review (2012).

6. "*Thin film solar cell based on $CuSbS_2$ absorber fabricated from an electrochemically deposited metal stack"*
   Wilman Septina, Shigeru Ikeda, Yuta Iga, Takayuki Nakamura, Takashi Harada, Michio Matsumura
   Thin Solid Films, submitted for publication (2013).

Peer-reviewed publications not included in the present thesis:

1. *"Synthesis of nanoporous TiO_2 and its potential applicability for dye-sensitized solar cell using antocyanine black rice"*
   Brian Yuliarto, Wilman Septina, Kasyful Fuadi, Fahiem Fanani, Lia Muliani, Nugraha
   Advances in Materials Science and Engineering, 2010 (2010).

2. "*Homogeneous electrochemical deposition of In on a Cu-covered Mo substrate for fabrication of efficient solar cells with a $CuInS_2$ photoabsorber"*
   Sun Min Lee, Shigeru Ikeda, Yasunari Otsuka, Wilman Septina, Takashi Harada, Michio Matsumura
   Electrochimica Acta, 79 (2012) 189-196.

3. "*Fabrication of $CuInS_2$ and $Cu(In,Ga)S_2$ thin films by a facile spray pyrolysis and their photovoltaic and photoelectrochemical properties"*
   Shigeru Ikeda, Midori Nonogaki, Wilman Septina, Gunawan Gunawan, Takashi Harada, Michio Matsumura
   Catalysis Science & Technology, in press (2013). DOI: 10.1039/C3CY00020F

Acknowledgements

The works in this thesis have been carried out at Research Center for Solar Energy Chemistry, Osaka University. I gratefully acknowledge Ministry of Education, Culture, Sports, Science, and Technology (MEXT) Japan for providing me the scholarship during my study. Certainly, the completion of this thesis could not be achieved without help and encouragement of many people to whom I am very grateful for.

First and foremost, I would like to thank my supervisors Prof. Michio Matsumura and Prof. Shigeru Ikeda for their constant guidance and motivation throughout my study. They let me involve in various research projects and gave me experiences to join numerous international conferences, which were extremely helpful in broaden my knowledge and also networking. I also thank Dr. Takashi Harada, who is always ready to help whenever I have technical difficulties, and all the members of Matsumura laboratory from 2008 to 2013 for being a very nice and helpful company.

I also not forget to thank the persons in University of Bath for their hospitality in which I spent three months of short time research. Prof. Laurie Peter gave me immense motivation and inspiration based on his excellent knowledge in electrochemistry. I also would like to thank Diego for his kindness to share his knowledge in his research and teached me a lot of electrochemistry techniques.

I thank my parents Deddy Rachman and Lindiawati for their motivation, and everything that they do for their son which is uncountable and indispensable. Words could not express my big thanks to them. My thanks also go to my younger sister and younger brother, Fitria Rachmawati and Luthfan Maftuh for being my motivation.

Finally, I thank my wife Meika Aidil Fitri and my son Hiro Aufaa Faheem for accompanying me in Japan, for their support, for their patience, and always ready to ease my tension and cherishing my day.

Certainly, there are so many important people which always give me encouragement for my study whom I could not thank one by one here. I thank them very much for being part of my life and their contributions so that this thesis can be completed.

Wilman Septina

September 2013